A Neutral Beam Based Beam Profile Diagnostic Solution for Integration on the CERN-LHC



Sam Attias
Rees Davison
Gerald Gan
Jiaruo Yan

supervised by
Professor F. Hofmann
Professor J. C. Tan

University of Oxford

Department of Engineering Science

Third-year Project Report

Trinity 2016

Acknowledgements

The authors of this project would like to express their gratitude for the supervision and support received by Professor F. Hofmann and Professor J. C. Tan of the University of Oxford throughout its duration. In addition, we would like to convey our thanks for the input and feedback received from CERN as well as their generosity for accommodating us during our visit. We thank R. Steinhagen and R. Veness of CERN for all their assistance.

Abstract

Particle accelerators are the most important instruments for physicists studying the fundamental nature of our universe. Observing high energy collisions give physicists a glimpse at the early moments of our universe. At present, the largest particle collider is the Large Hadron Collider (LHC) based at CERN on the Franco-Swiss border. The particle collider took over 10 years to build and the collaboration of thousands of scientists from around the world. CERN is currently working towards further increasing the luminosity and beam energy of the LHC towards its target of 14TeV. The LHC-HL project has been setup to facilitate this upgrade. Reaching this goal raises significant engineering challenges. One such challenge is collimation, the process of reducing beam divergence due to electrostatic repulsion of hadrons. Design for a collimator has been initiated. This report proposes a novel and yet unexplored application of neutral beams in the role of beam diagnostics for collimator calibration and aims to highlight the advantages and technical challenges of such a solution.

Contents

1 Introduction **1**

1.0.1 Specification . . . 2
1.0.2 Existing Diagnostic Tools . . . 2
1.0.3 Initial Proposal . . . 4

2 Neutral Beam Interaction **5**

2.0.1 Aim . . . 5
2.1 Upper energy limit . . . 5
2.2 Ionization . . . 7
2.2.1 Ionisation Cross Section, σ . . . 7
2.2.2 Particle Flux . . . 10
2.2.2.1 Coherently Pulsed Neutral Beam (CPNB) . . . 12
2.2.3 Neutral beam thickness . . . 13
2.2.4 Neutral beam density . . . 13
2.3 Feasibility . . . 13
2.3.1 Neutral beam ionisation . . . 13
2.3.2 Proton beam signal . . . 15
2.4 Beam shape . . . 16
2.5 Fluorescence . . . 17
2.5.1 Proton Beam Fluorescence . . . 20
2.5.2 Final Proposal . . . 22
2.6 Overall Device Design . . . 23
2.6.1 Location . . . 23
2.6.2 Integration with Collimator . . . 24
2.6.2.1 Neutral beam generator . . . 26
2.6.2.2 Detectors . . . 27
2.6.3 Technical Specification Summary . . . 27

3 Neutral Beam Generation **28**
3.1 Generation Methods 28
3.1.1 Negative Ion Neutralisation 28
3.1.2 Positive Ion Neutralisation 29
3.1.3 Accelerated Neutral Atom Beam (ANAB) 29
3.1.4 Quantum Gas Jet 30
3.2 Negative Hydrogen Ion Source: Penning Ion Gauge 31
3.2.1 General Mechanism 31
3.2.2 Practical Concerns 32
3.2.2.1 Electron Co-extraction 33
3.2.2.2 Caesium-induced Breakdowns 33
3.2.3 Design Choices 34
3.2.3.1 Penning Ion Gauge vs Other Sources 34
3.2.3.2 Geometry and Magnetic Field 34
3.2.3.3 Further Development and Concerns 35
3.3 Ion Beam Lensing 35
3.3.1 Electrostatic Lens Basics 35
3.3.2 The Einzel Lens 36
3.3.3 Focusing Lens Design Considerations 36
3.3.3.1 Einzel Lens Mode 37
3.3.3.2 Centre Lens Electrode Potential 37
3.4 Beam Deflection and Scanning 38
3.4.1 Parallel Plate Condenser 38
3.4.2 Angle of Incidence on Hadron Beam 39
3.4.3 Effect on Focusing 40
3.4.3.1 Simulation of Ion Lensing and Deflection 41
3.4.4 Practical Concerns 41
3.5 Ion Beam Neutralisation 43
3.5.1 Maximising Cross Section of the Reaction 43
3.5.2 Maximising Irradiation Time 44
3.5.2.1 Mirror Design Considerations 45
3.5.3 Maximising Photon Flux 46
3.5.4 Neutralisation Variation While Scanning 46
3.5.4.1 Beam Geometry 46
3.5.4.2 Laser Interference 47
3.5.5 Other Practical Considerations 50

3.5.5.1 Incomplete Neutralisation of the Beam 50
3.5.5.2 Laser Induced Damage of Components 50
3.5.5.3 Magnetic Field of the Environment 50
3.5.6 Neutralisation Chamber Design Process 51
3.5.6.1 Mirror Choice 51
3.5.6.2 Laser Source Specification 52
3.5.6.3 Laser Source Arrangement 52
3.5.6.4 Neutralisation Chamber Model 53
3.6 Overall Architecture 55

4 Hollow Electron Beam Imaging 56
4.1 Neutral Particle Detector 56
4.1.1 Semiconductor Detector for Atomic Hydrogen 56
4.1.2 Neutral Particle Imager (NPI) 58
4.1.2.1 Surface Interaction 59
4.1.3 Micro-Channel Plate (MCP) Neutral Detector 63
4.1.4 MCP Operation and Assembly 63
4.1.5 Delay-line layer 65
4.1.6 Mechanical Design 66
4.1.7 Calibration 67
4.1.7.1 MCP Characteristics 67
4.2 Reconstruction of the 2D Beam Profile 69
4.2.1 Challenges 69
4.2.2 Explored methods of reconstruction 69
4.2.2.1 Radon Transform and Inverse Radon Transform 70
4.2.2.2 Binary Image Reconstruction 71
4.2.2.3 Other Reconstruction Methods 72
4.2.3 Hollow Electron Beam Profile Model 73
4.2.4 Produce 1D Projections 74
4.2.5 Back Projection and Improvements 75
4.2.6 Determination of Parameters 77
4.2.7 Practical Issues in Reconstruction 78
4.2.7.1 Obtaining 1D Projection Data from Detector 78
4.2.7.2 Noises 78
4.3 Extensions to a more general beam profile 79

4.3.1 Elliptical Beam Profile Reconstruction From Two Orthogonal Projections . . . 79
4.3.2 Reconstruction of True Beam Profile From Few Projections . . . 80

5 Imaging the Proton Beam 81
5.1 Lens Modelling Techniques . . . 81
5.1.1 The Thin Lens Equation . . . 81
5.1.2 Matrix modelling . . . 82
5.1.3 Aberrations . . . 83
5.1.4 Depth of field . . . 84
5.2 Computer Modelling . . . 84
5.2.1 Using the thin lens equation to model the blur circle . . . 84
5.2.2 Accounting for Lens Thickness . . . 86
5.2.3 Test Data . . . 86
5.2.4 Aperture . . . 88
5.2.5 Sensor Noise . . . 88
5.2.6 Final Model . . . 89
5.3 Choice of Lens . . . 90
5.3.1 Single Lens . . . 90
5.3.2 Bi-Telecentric Lenses . . . 91
5.3.3 Standard Fixed Focal Length Lenses . . . 91
5.3.4 Zoom Lenses . . . 92
5.3.5 Final Choice . . . 92
5.3.6 Motorised Control . . . 93
5.4 Choice of Camera . . . 94
5.4.1 Sensor . . . 94
5.4.1.1 CCD . . . 94
5.4.1.2 CMOS . . . 94
5.4.2 Image Intensifier . . . 95
5.4.3 Final Camera Choice . . . 96
5.5 Proton Beam Reconstruction . . . 96
5.5.1 Integration of Data . . . 97
5.5.2 Smoothing the Data . . . 97
5.5.3 Rectangular Window . . . 98
5.5.4 Hamming Window . . . 99
5.5.5 Noise Removal . . . 100

5.5.6 The Final Approach 101
5.5.6.1 Final Reconstruction 102
5.5.6.2 Further Testing 103
5.6 SOLIDWORKS Models 106

6 Conclusion **107**
6.1 Further Developments 109
6.1.1 Obtaining High Energy Cross Section Data 109
6.1.2 Calibrating Neutral Atom Gun 109
6.1.3 Optimising Reconstruction 109
6.1.4 Improving CCD Noise Rejection 110
6.1.5 Miscellaneous 110

Bibliography **111**

List of Figures

1.1 Reference diagrams given in project specification. 2

2.1 Basic diagnostic configuration for single axis profile 6
2.2 Approximate upper energy limit for neutral beam interaction (equation 2.1) into singly charged ions 7
2.3 Measurement of σ for impact of electron, positron, proton and antiproton for Helium[10]. 8
2.4 Empirical plot of Ionisation Cross Section from equations 2.3 and 2.4 on a log-log axis 9
2.5 p-beam and e-shell profile from equation 2.6 10
2.6 Monte-Carlo simulation of interaction of neutral beam ◇ with protons –, electrons – for neutral beam radius of 1σ 11
2.7 Ratio of intercepted particles by 1σ neutral beam from Monte-Carlo simulation 12
2.8 Plot showing the proportion of neutral beam that is ionised (by protons in red and by electrons in blue) for beam radius $r = 1\sigma$ and $E = 100$eV 15
2.9 Scheme of a gas curtain BIF monitor as evaluated in this chapter. 16
2.10 MATLAB simulation of $45°$ gas curtain interception of beams. 17
2.11 Beam profile data yielded from various gasses [6] 18
2.12 Configuration of a BIF monitor [17] 19
2.13 Normalised proton energy loss to Nitrogen as a function of proton beam energy given by Bethe equation [16]. 21
2.14 Experimental data conducted on a proton beam with properties: $\sigma = 676\mu$, $I = 140$ mA, 2×10^{13} protons, beam energy $= 450$ GeV, and nitrogen pressure 5×10^{-7} Torr with a Gaussian curve fitted to vertical profile [21]. . 21
2.15 Representation of overall beam diagnostic configuration in one axis as described in section 2.5.2. 22
2.16 Photograph of the candidate location RB-46 from Figure 2.17 and CAD representation of implementation [1] 23

2.17 Candidate positions for the electron lenses are RB-44 and RB-46 at Point 4 [1] . . . 24
2.18 CAD model of electron lens with intended diagnostic observation region highlighted in blue where $l \approx 1010$mm and $d \approx 480$mm. . . . 24
2.19 CAD representation of diagnostic configuration with constituent elements defined in Table 2.3. . . . 25
2.20 MATLAB B-field simulation around collimator solenoid with superimposed CAD outline of collimator. . . . 26

3.1 A 2-D representation of the Penning Ion Gauge . . . 31
3.2 2-D representation of an Einzel Lens focusing a beam[32] . . . 36
3.3 Graph of Einzel lens focusing strength against voltage ratio[32] . . . 36
3.4 Deflection of ion beam with matched parallel plate condensers . . . 40
3.5 Comparison of Focal Lengths of Deflected and Undeflected Ion Beam . . . 42
3.6 Plot showing experimental data of photo-detachment cross-section against photon energy [35] . . . 44
3.7 2-Dimensional abstraction of laser beam path as it reflects in the chamber, relative to the ion beam . . . 45
3.8 Diagram to illustrate variation of intersecting laser intensity, where H represents half design intensity and F full design intensity *(note laser angles are exaggerated to illustrate the concept)* . . . 47
3.9 Variation of intersecting laser intensity as ion beam is scanned . . . 48
3.10 Transverse plane interference patterns for various number of lasers . . . 49
3.11 CAD Model of Neutralisation Chamber . . . 54
3.12 Overall Beam Line Architecture . . . 55

4.1 Semiconductor Detector System[43] . . . 57
4.2 Ionisation Efficiency for Atoms as a Function of Energy [44] . . . 58
4.3 Schematic Views of High Frequency Shutter [44] . . . 59
4.4 Detection by Reflection Surface [44] . . . 60
4.5 Concept of Detection based on Secondary Electron Emission [44] . . . 61
4.6 3D CAD Model for NPI, Modified from the Model in [44] . . . 62
4.7 MCP Schematic Structure, Hamamatsu [47] . . . 63
4.8 MCP CF Flange Assembly [48] . . . 64
4.9 Schematic of the Hexanode [49] . . . 65
4.10 MCP Detection System MCA refers to multi-channel analyser . . . 66
4.11 Calibration Results of the neutral MCP Detector from [50] . . . 67

4.12 Discrete Gaussian Electron Shell Synthesised in MATLAB resolution = 420×560, data type: uint8 70
4.13 Radon Transform from [51] 70
4.14 Synthesised Gaussian Electron Shell Profile from MATLAB, 420×560 . . . 74
4.15 Projections in 2 Orthogonal Directions for Figure 4.14 75
4.16 Back Projection Reconstruction 76
4.17 Fitting to the Ends for an Estimation of Parameters 77
4.18 Obtaining Projections from the Oblique Elliptical Beam Profile 79

5.1 Thin Lens Equation from [59] 81
5.2 Blur Circle diameter formula 84
5.3 Vector approach to Light Mapping 85
5.4 Thick lens Representation 86
5.5 Profile formed using Gaussian formula 87
5.6 Randomly generated data 88
5.7 Perfect Focusing, beam position 1.2 mm 89
5.8 Imperfect Focusing, beam position 1.2 mm 89
5.9 Perfect Focusing, beam position -5.6 mm 90
5.10 Imperfect Focusing, beam position -5.6 mm 90
5.11 Image Intensifier from [71] 95
5.12 Image captured on camera sensor at Beam Position 1.2mm 97
5.13 Integration of Image along z-axis from figure 5.12b 98
5.14 Different rectangular window sizes at Beam Position 1.2mm 99
5.15 Different Hamming window sizes at Beam Position 1.2mm 100
5.16 Integrated slices, threshold value removal, linear interpolation, at Beam Position 1.2mm 101
5.17 $k = 1000\times$Noise Signal at Beam Position 7.6mm 101
5.18 Noise Removed, Hamming Window Filtered, Scale and Delay Corrected . . 102
5.19 Slices compiled at their Beam Position 103
5.20 Proton Beam Reconstruction 104
5.21 Profile reconstructed after going through system 104
5.22 Profile reconstructed with protons centred at $x = 1$ mm, $y = 1$ mm 105
5.23 Profile reconstructed with protons centred at $x = -0.5$ mm, $y = -1$ mm . . 105
5.24 3D camera and lens setup 106
5.25 2D drawing of component parts 106

Chapter 1

Introduction

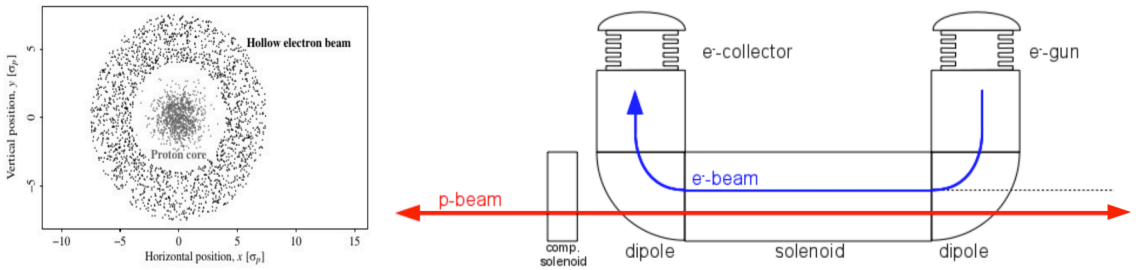
Particle colliders such as the Large Hadron Collider (LHC) on the Franco-Swiss border are incredibly powerful tools for physicists studying the fundamental nature of our universe. The LHC is the largest of such colliders being over 27 km in circumference. The LHC generates two proton beams with energies up to 7 TeV travelling in opposite directions before directing them to converge. The interaction between colliding high-energy beams causes the release of their constituent particles that physicists aim to detect in their study of sub-atomic particle physics.

There are many difficulties in generating such a high intensity beam. One of them being beam divergence. Dense proton beams have a tendency to diverge due to electromagnetic repulsion between individual protons. Divergence in the proton beams is undesirable as it causes exponential decrease in luminosity through particle loss, vacuum degradation and uncontrolled energy loss (damage to equipment).

An electron lens based collimator has been designed to reduce the problem of proton beam divergence [1]. The collimator works on the principle of space-charge compensation i.e. the electrostatic force between protons can be compensated by the electromagnetic force of an opposite charged beam parallel to its axis. Specifically, an electron lens generates a hollow electron beam (e-beam) around the proton beam (p-beam) to compensate divergence force. The optimal profile is shown in figure 1.1a. The electron shell serves the additional purpose of proton beam halo cleaning i.e. removing protons that have diverged far from the net beam path. The electron lens consists of an electron gun (e-gun), an electron collector (e-collector) and a strong solenoid for focusing the electron beam. The configuration is shown in figure 1.1b.

Two collimator's will be installed on the LHC, one for each proton beam in each direction. For the collimators to be effective we must know the relative positions of the p-beam and e-beam such that we can calibrate the e-beam to be coincident with the p-beam (as in

figure 1.1a) for optimal effect. This report will address the design of a diagnostic tool capable of imaging both the e-beam and p-beam to produce a cross sectional profile of both beams to facilitate calibration of the collimator leading to reduced divergence and increased proton beam luminescence.



(a) e-beam & p-beam profile (b) Electron lens configuration

Figure 1.1: Reference diagrams given in project specification.

1.0.1 Specification

Task to develop an efficient *in-situ* beam diagnostic solution for integration with an electron-lens collimator installed on the CERN-LHC. The diagnostic device must measure asymmetry and distribution of both the main hadron beam and the electron shell generated in the collimator to optimise overlap and beam position.
Preferred:

- non-invasive operation during regular LHC operation.
- ideally performed under nominal HL-LHC conditions (e-beam: 10-100 A, p-beam: 0.5 A, UHV conditions, RF beam impedance, LHC beam size: $\sigma = 1$mm r.m.s. (round))
- Simple & Safe Design i.e.no un-safe objects too close to the beam.

1.0.2 Existing Diagnostic Tools

Several different diagnostic tools have already been developed and are in use in the field of beam diagnostics. A number of the most common techniques are evaluated below and considered with respect to the specification.

Wire Scanner/'Flying wire' [2] A single wire usually of Carbon or SiC is swept across the beam path. Incident particles cause secondary electrons to be liberated. A polarisation voltage removes the liberated electrons causing a current to flow into the wire. This current is measured for each wire and together with wire position is used to reconstruct the beam profile along a single axis.

At high beam intensity this method is considered non-destructive. However, studies show that wire temperature in high-intensity beams will exceed 1400 K, considered

the safe limit for the material [3]. Likewise, at low-intensity, for example during beam run-up, the beam deposits much more energy into the wire causing it to be destroyed in a few ms.

In conclusion, a wire scanner cannot be considered an *in-situ* diagnostic tool for high-intensity beams.

Secondary Emission (SEM) Grids [4] Consist of a grid of thin wires each linked to a current-voltage amplifier. This works on the same principle as the wire scanner described above. Evidently, as was the case with the wire scanner any solid material exposed to a high-intensity beam will be destroyed in a matter of ms. Therefore SEM grids are not a viable option.

Residual Gas Ionisation Monitor [5] This technique, considered non-destructive, aims to detect residual ionised products from the collisions between protons and residual gasses present in the vacuum chamber, usually Nitrogen. The ionised products are directed towards a detector using an electric field.

An immediate issue that would arise in the context of using a residual gas monitor with an electron lens is the presence of the electron lens' solenoidal magnetic field which has a maximum magnitude of 7 T. This would affect the trajectory of any ionised particles produced and remove all spatial resolution from the detected signal.

Beam Induced Fluorescence (BIF) Monitor [6] Works on a similar principle to the ionisation monitor however measures the emission of ionisation photons rather than ionised products. For example, N_2 atoms interact with protons to produce N_2^+. These ions decay producing photons in the visible frequency range proportional to the proton beam intensity and partial gas pressure. The photons are detected with a CCD camera. Often additional Nitrogen is injected into the vacuum to enhance the effect. Additional Nitrogen can be injected as a beam (Gas Jet Monitoring) or as a curtain (Gas Curtain Monitoring). These methods are in use at CERN for high-intensity beam monitoring.

BIF monitoring is considered to be minimally invasive. However research has shown that that the fluorescence profile width obtained is always greater than the true profile width [7]. This is due to fluorescence from halo protons distorting the image. Furthermore this raises the question of how to distinguish between the proton beam and electron beam.

Synchrotron Radiation Monitor [8] This is a non-destructive technique that measures the radiation emitted by accelerating charged particles, known as synchrotron radiation. The emission propagates tangential to the beam trajectory opening in a cone shape. A signal can be obtained *via* a CCD camera and calibrated band-pass filtering.

This technique is not-applicable to imaging within the collimator since the collimator is a linear segment of the LHC thus there is no particle acceleration and therefore no synchrotron emission.

From the existing diagnostic techniques considered above, the only viable technique is that of Beam Induced Fluorescence (BIF) Monitoring. This shall be one of the underlying principles behind this reports design proposal.

1.0.3 Initial Proposal

The initial proposed concept and focus of the feasibility study comprises of the following stages:

1. A thin beam of neutral gas atoms (neutral beam) as shown in Figure 2.1 is scanned linearly across the cross-section of the proton beam and electron shell.
2. The neutral gas atoms upon interaction with high velocity electrons or protons will become ionised.
3. Upon ionisation the particles are deflected away from the axis of the neutral beam due to electric and magnetic field influences present within the vacuum chamber (the solenoidal B-field in the electron lens).
4. The gas atoms that are not ionised by a proton or electron continue on a straight trajectory towards a detector placed at the opposite end to the neutral beam source.
5. The detector measures the proportion of the neutral gas atoms that arrive unaffected by the protons and electrons with respect to position of the neutral beam. This profile should represent the inverse of a single axis density profile of the combined proton beam and electron shell.
6. The combined beam profile is separated computationally into two individual profiles: one for the proton beam and one for the electron shell through detection of the distinguishable peaks and known density distribution profiles.
7. The process is repeated along two axes to yield corresponding x and y profiles. The process is repeated at a frequency of 60 Hz to yield an *in-situ* model of the beam for use in calibration of the electron collimator.

Chapter 2

Neutral Beam Interaction

2.0.1 Aim

This section of the report will focus on the interaction of the diagnostic neutral gas beam with the proton beam and electron shell produced by the collimator. The aim of understanding the interaction processes is to assess fundamental feasibility of the proposed solution and to determine the neutral gas beam parameters to optimise detection and eventually beam-profile reconstruction.
To assess the feasibility of this method the following questions must be answered:

1. What is the maximum neutral beam energy for an atom, once ionised, to be deflected away from the detector so as not to interfere with the detection of the unionised neutral beam?

2. At what beam energy will a significant proportion of the neutral atoms become ionised and is this energy below the aforementioned maximum beam energy?

3. Are the detectable profiles of the proton beam and electron shell distinguishable from one another in the total beam profile? If not, is there an alternative way to separate the signals?

2.1 Upper energy limit

To answer the first question the assumption must be made that the neutral particles are ionised within the cross section of the proton beam and electron shell. This assumption shall be justified later in the report when analysing neutral beam ionisation.
For a charged particle inside the vacuum chamber of the collimator, its trajectory may be influenced by the following:

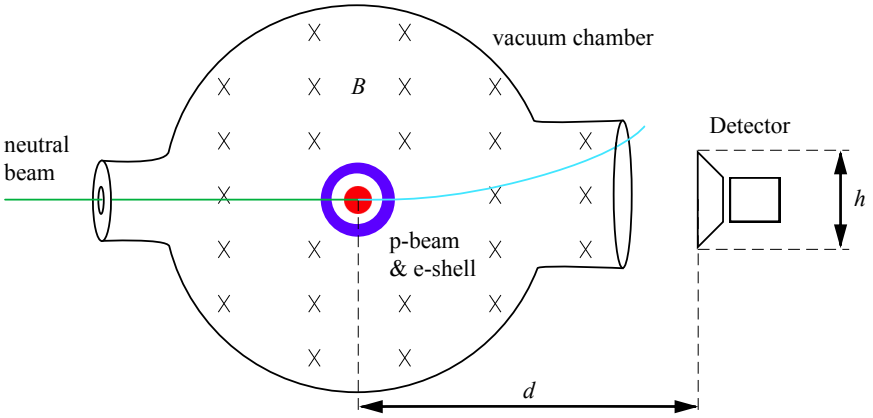


Figure 2.1: Basic diagnostic configuration for single axis profile

The E-field due to the proton beam and electron shell Although the E-field may be large due to high particle density its magnitude will fall off with $1/r^2$. It is therefore permissible to ignore the E-field for ions far from the cross section of the electron and proton beams.

The B-field due to the proton beam and electron shell can be assumed sufficiently weak compared to the applied solenoidal magnetic field described below so as to be ignored.

The B-field due to the solenoid The large solenoid used in the electron collimator produces a B-field of 1-7 T. This B-field will remain relatively uniform across the cross section of the vacuum. In the analysis it shall assumed that the B-field will remain constant between the main beam and the detector.

Through approximate calculation of the above field strengths it can be deduced that the B-field due to the solenoid represents the most significant force on the ionised beam. Through the above assumptions equation 2.1 can be derived. It represents the upper limit on the neutral beam energy in electron volts such that the ionised particles are deflected away from the detector so as to prevent interference signals. The equation is plotted in figure 2.2 with the apparatus dimensions from section 2.6.2.

$$E(\text{eV}) = \frac{q}{2m}\left(\frac{Bd}{\sin(2\arctan(h/2d))}\right)^2 \tag{2.1}$$

Where B is the solenoidal field strength (7 T), q is the charge of the ion, m is its mass and d & h are geometric parameters shown in figure 2.1.

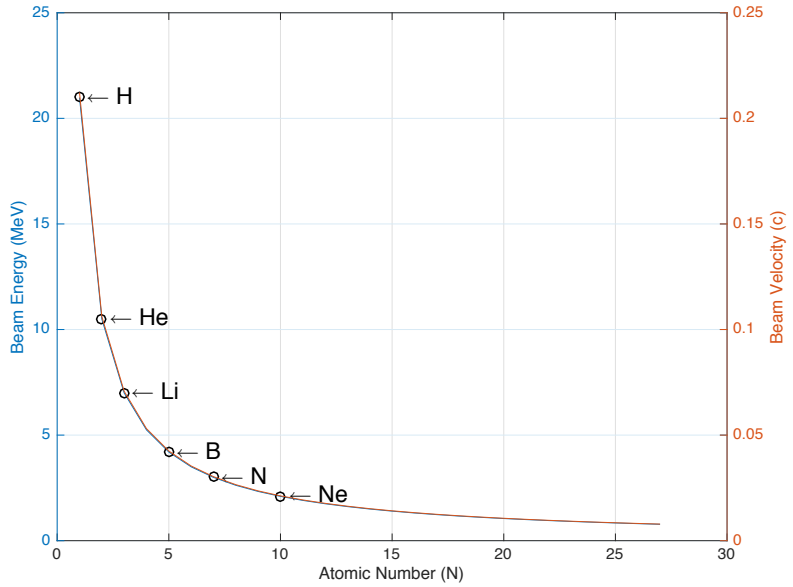


Figure 2.2: Approximate upper energy limit for neutral beam interaction (equation 2.1) into singly charged ions

2.2 Ionization

Now that an upper limit on beam energy has been established, the second question must be considered: What is the effective lower limit on beam energy? To begin answering this question it is necessary to determine the probability of a neutral particle becoming ionised upon interaction with the high speed electrons and protons within the collimator.

2.2.1 Ionisation Cross Section, σ

There are many factors that come into play when determining ionisation rates. Firstly, the ionisation cross section must be considered.

The Ionisation Cross Section is the probability of an atom being ionised in a given volume of space; this can be described by equation 2.2.

$$P_{ion} = \sigma(E_{proj})\rho_{gas}d_{gas} \quad [9] \tag{2.2}$$

Where σ is the ionisation cross section, E_{proj} is the energy of the incident protons or electrons (projectiles), ρ_{gas} is the neutral beam density and d_{gas} is the target thickness.

The value of σ is found experimentally for a given ionisation state of an individual species by a specified incident projectile and its energy. This analysis requires only the first ionisation of a neutral atom by impact of electrons and protons. Figure 2.3 shows this relationship

for Helium but a similar trend is true across other elements. As expected, for low hadron energies (projectiles) there will be insufficient energy for ionisation and so σ will be small. For high projectile energy the projectile will be travelling fast and so the interaction time for ionisation will be small. Thus σ will be small. There must therefore exist a point between the two aforementioned scenarios where σ is maximised and this is indeed the case shown in figure 2.3.

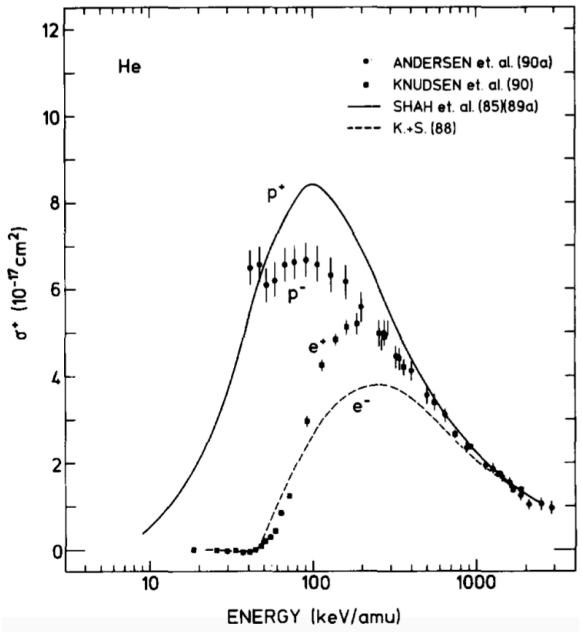


Figure 2.3: Measurement of σ for impact of electron, positron, proton and antiproton for Helium[10].

From figure 2.3 it is immediately clear that for energies beyond 10 MeV the ionisation cross section tends to zero. This is also the case for other single atoms. However, a useful relationship is also realised: the trend for ionisation by electrons and protons converge. Therefore, from this point onwards equal probability of ionisation for protons and electrons shall be assumed for high projectile energy. The maximum design energy of the proton beam is 7 TeV. In this energy range no experimental results exist, it is just known that the ionisation cross section will be small. The question then becomes: how small? To answer this, empirical formula can be fitted to experimental data. Such analysis has been conducted in the 60's by Wolfgang Lotz [11]. The following equations 2.3 and 2.4 approximate the relationship between energy and ionisation cross section.

$$\sigma = \zeta_1 \frac{a \ln(\frac{E}{x_1})}{x_1 \cdot E} \ [\text{cm}^2], \qquad if \qquad x_1 \leq E \leq x_2, \tag{2.3}$$

Specie	Configuration	Ionisation Potential			U_{max}	Effective Number, $\bar{\zeta}$					
						$U \approx 1.25$		$U = U_{max}$		$E \gg x_2$	
		x_1	x_2	$\bar{x}$	$U(x_1)$	exp.	theor.	exp.	theor.	exp.	theor.
Hydrogen I	$1s$	13.6	-	-	4.0	0.49	1	0.90	1	1.0	1
Helium I	$1s^2$	24.6	-	-	4.9	0.70	2	1.75	2	2.0	2
Lithium I	$1s^2 2s$	5.39	56	7.87	3.0	0.65	1	1.04	1	1.7	1.7
Boron I	$2s^2 p$	8.30	12.9	10.6	(6)	(0.6)	1	(2.1)	2.9	(2.9)	2.9
Nitrogen I	$2s^2 p^3$	14.5	20.3	16.2	7	0.58	3	3.3	4.9	4.2	4.9
Neon I	$2s^2 p^6$	21.6	48.5	23.9	8	0.52	6	4.0	7.6	5.3	7.6

Table 2.1: Data Table for Various Elements (Brackets Indicate Predicted Values) [11]

$$\sigma = \sum_{i=1}^{N} \zeta_i \frac{a \ln(\frac{E}{x_1})}{x_i \cdot E} = \bar{\zeta} \frac{a \ln(\frac{E}{\bar{x}})}{\bar{x} \cdot E}, \qquad if \qquad E \geq x_N \tag{2.4}$$

[11] Where x_1 is the ionisation potential for electron in the outermost shell in electron-volts, x_2 is ionisation potential for electron in the next inner (sub)-shell etc., $\bar{x}$ is the weighted mean of x_1 and x_2, etc., E is the electron energy in electron-volts, $a = 4.0 \times 10^{-14}$ and $\zeta \geq 0.5$ is a varying function representing the number of equivalent electrons.

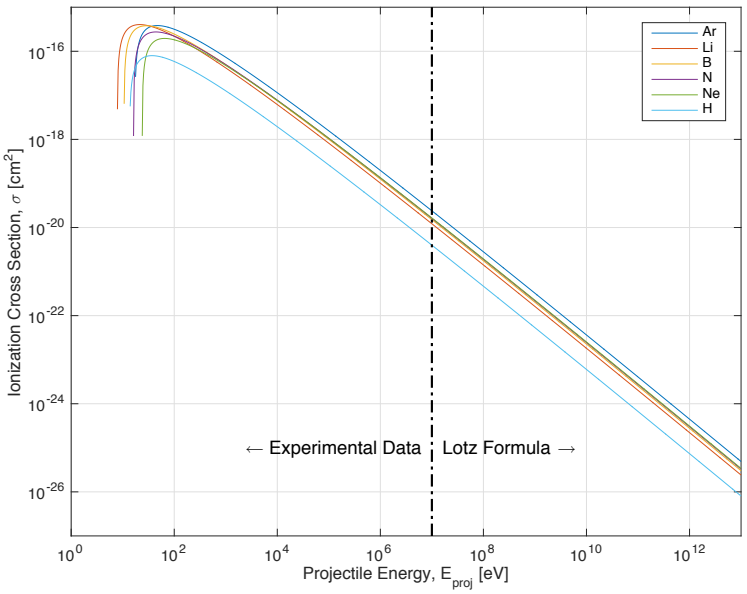


Figure 2.4: Empirical plot of Ionisation Cross Section from equations 2.3 and 2.4 on a log-log axis

The empirical formula describing ionization cross section described by equations 2.3 and 2.4 is plotted in figure 2.4. As expected, the value of σ falls off logarithmically in magnitude. From these results, at an incident proton energy of 7 TeV [12], for atomic Hydrogen, an approximate value of $\sigma_{proton} \approx 6.9 \times 10^{-26}\text{cm}^2$ can be expected and at an incident

electron energy of 25 KeV[13], $\sigma_{electron} \approx 5.2 \times 10^{-18}$cm^2.

2.2.2 Particle Flux

Now that an approximate value for the ionisation cross section has been yielded it becomes necessary to consider the required parameters of the neutral beam to yield accurate profile content. Equation 2.2 in section 2.2.1 represents the probability of ionisation. From this, a statement about the ionisation rate can be written in the form of equation 2.5 where ϕ represents the particle flux per second for the respective beam.

$$R_{ionization} = \rho_{gas} d_{gas} (\phi_{proton} \sigma_{proton} + \phi_{electron} \sigma_{electron}) \tag{2.5}$$

To calculate the flux both the electron and proton distributions through the cross section of the beams must be analysed. Both the electron shell and proton beam can be idealised as Gaussian distributions. It is convenient to describe the profile in polar coordinates as given by equation 2.6 where σ^* represents the standard deviation, I represents the intensity and R represents the electron shell radius.

$$P(r) = (2\pi)^2 \left[\frac{I_p}{\sigma_p^*} e^{-\frac{r^2}{2\sigma_{p*}^2}} + \frac{I_e}{\sigma_e^*} e^{-\frac{(r-R)^2}{2\sigma_{e*}^2}} \right] \tag{2.6}$$

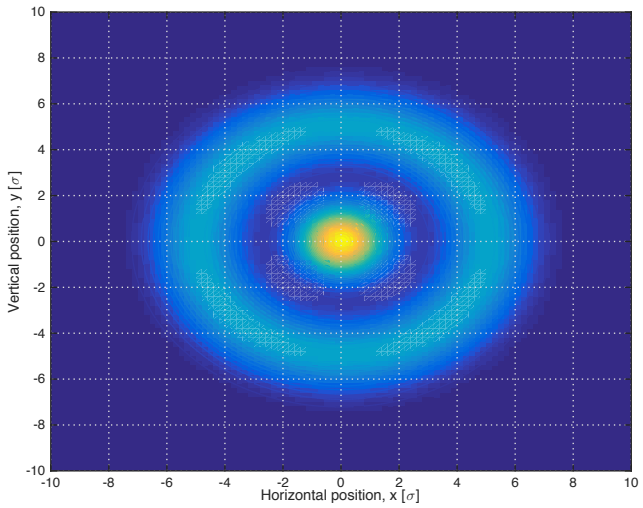


Figure 2.5: p-beam and e-shell profile from equation 2.6

This profile model can be compiled into a computational simulation to calculate the proportion of particles intercepted by the neutral beam when scanning the p-beam and e-shell profile. In the model the following assumptions have been made:

- The neutral beam scanning velocity is slow such that the proton bunches can be considered as continuous.
- The density of the neutral beam is uniform throughout its circular cross section.
- Scanning of the neutral beam can be considered as horizontal to the plane of the p-beam and e-shell.

In addition to these assumption, the model demands the proton and electron fluxes; These can be calculated fairly simply from LHC current parameters *via* $\phi_{total} = I/q$. Taking proton beam current $I_{proton} = 0.58$A [12] and maximum electron collimator current $I_{electron} = 50$A [13] the total proton flux can be calculated: $\phi_{total,proton} = 3.62 \times 10^{18}$ protons/sec and the total electron flux $\phi_{total,electron} = 3.12 \times 10^{20}$ electrons/sec.

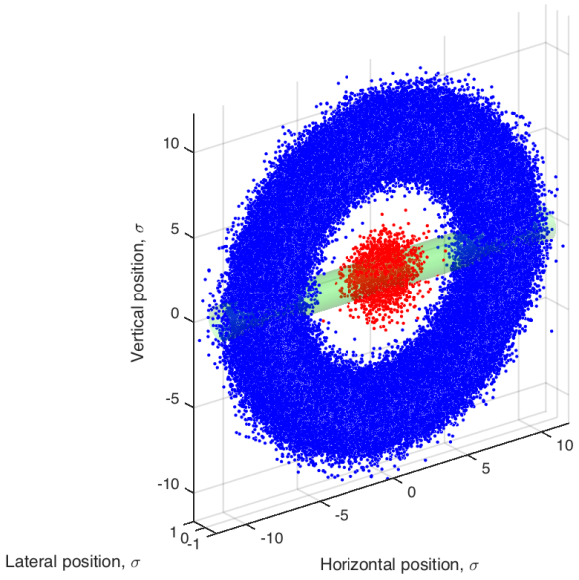
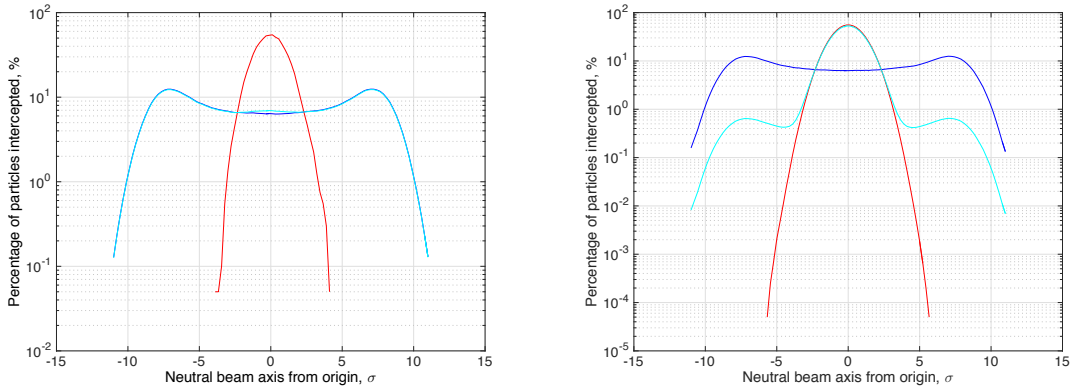


Figure 2.6: Monte-Carlo simulation of interaction of neutral beam ◇ with protons –, electrons – for neutral beam radius of 1σ



(a) Continuous Neutral Beam (b) CPNB

Figure 2.7: Ratio of intercepted particles by 1σ neutral beam from Monte-Carlo simulation

Using equation 2.6 in addition to the aforementioned parameters, and an element analysis of the beam profile as shown in figure 2.6, the relationship between the proportion of intercepted particles and the neutral beam position can be derived. This is shown in figure 2.7a for a neutral beam radius of 1σ. Focusing the analysis on the beam at central position i.e.when neutral beam axis is at zero distance from the origin: from figure 2.7a it is shown that $\sim 55\%$ of protons are intercepted and $\sim 6.3\%$ of electrons are intercepted. From these results, it can be calculated that at the central point, proton flux $\phi_{proton} = 1.99 \times 10^{18}$protons/sec and electron flux $\phi_{electron} = 1.97 \times 10^{19}$electrons/sec.

2.2.2.1 Coherently Pulsed Neutral Beam (CPNB)

From figure 2.7a above it is realised that a relatively small proportion of the intercepted particles are protons. This is because the proton flux is relatively small with the proton beam current $\times 86$ smaller than the electron beam current. This is true only in the case where the proton beam is considered to be continuous.

In reality the proton beam consists of high luminosity bunches spaced at even intervals. A variant of the initial proposal conceptualises a pulsed neutral beam that is synchronised to intercept individual proton bunches. From LHC beam parameters it is noted that for a bunch spacing of 25 ns[12] an approximate pulse frequency of the neutral beam of 40.0 MHz would be required. In reality the CPNB frequency would have to remain a variable to account for different beam proton velocities where the average passing frequency is 31.6 MHz [12].

A corresponding instantaneous proton beam current can be calculated corresponding to an r.m.s. bunch length of 7.55cm and a bunch spacing of 25ns $\times\, c \approx 7.5$m.

$$I_{inst.} = \frac{7.5}{0.0755} I_{proton} = 57.6\text{A} \tag{2.7}$$

This equivalent proton beam current corresponds to an instantaneous particle flux of $\phi_{protontotal,inst.} = I/q = 3.60 \times 10^{20}$protons/sec. Taking the proportion of protons intercepted at neutral beam position of zero distance from the origin to be 55% (the same as for a continuous beam) we get a proton flux of $\phi_{proton,inst.} = 1.98 \times 10^{20}$protons/sec. This is over $\times 100$ greater than the flux achieved by a continuous neutral beam. This result is further considered in section 2.3.1.

2.2.3 Neutral beam thickness

Referring to equation 2.2, d_{gas} represents the target thickness i.e.the distance travelled by a projectile through the neutral beam. Since the neutral beam has a circular cross section, the value of d_{gas} will be a function of radius rather than a constant. Again working on the assumption that the neutral beam is uniform d_{gas} can be derived by integration from simple geometry:

$$d_{gas} = \frac{2r}{\pi} \int_0^{\pi/2} \sin\left(\frac{\pi - 2\theta}{2}\right) d\theta = \frac{2r}{\pi} \tag{2.8}$$

For the case discussed where the neutral beam radius is 1σ we get $d_{gas} = 2\sigma/\pi$.

2.2.4 Neutral beam density

The final parameter in equation 2.2 that must be derived is ρ_{gas}, the neutral beam density in $atoms/m^3$. This parameter is determined by the neutral beam generation process as outlined in chapter 3 and can be calculated from $\rho_{gas} = \phi_{neutral}/vA$ where $\phi_{neutral}$ is the neutral beam flux, v is the neutral beam velocity and A is the neutral beam cross-sectional area (πr^2).

Substituting this along with equation 2.8 into equation 2.2 to give:

$$R_{ionization} = \frac{2\phi_{neutral}}{vr\pi^2}(\phi_{proton}\sigma_{proton} + \phi_{electron}\sigma_{electron}) \tag{2.9}$$

2.3 Feasibility

2.3.1 Neutral beam ionisation

All parameters have now been derived to assess the feasibility of a neutral beam based solution. Taking equation 2.10 and dividing by $\phi_{neutral}$ yields the proportion of the neutral beam that is ionised. Note that this proportion is independent of the neutral beam flux. Assuming neutral beam velocity $v \ll c$, this gives $v = \sqrt{2Eq_e/m}$ where E is the neutral

beam energy in electron-volts, q_e is the charge on an electron and m is the neutral particle mass in kg. Substituting into equation 2.10 results in:

$$\frac{R_{ionisation}}{\phi_{neutral}} = \frac{1}{r\pi^2}\sqrt{\frac{2m}{Eq_e}}(\phi_{proton}\sigma_{proton} + \phi_{electron}\sigma_{electron}) \tag{2.10}$$

From the approximate values derived in section 2.2, the proportion of a neutral atomic hydrogen ($m = 1u$) beam of radius $r = 1\sigma$ (where $\sigma \approx 1 \times 10^{-4}$m) passing through the origin of the p-beam and e-shell can be computed. From section 2.2.1 σ_{proton}(7TeV) $\approx 6.9 \times 10^{-26}$cm^2 & $\sigma_{electron}$(25KeV) $\approx 5.2 \times 10^{-18}$cm^2, from section 2.2.2 $\phi_{proton} = 1.99 \times 10^{18}$protons/sec ($\phi_{proton,inst.} = 1.98 \times 10^{20}$protons/sec for CPNB) and $\phi_{electron} = 1.97 \times 10^{19}$electrons/sec. This gives:

$$\frac{R_{ionisation}}{\phi_{neutral}} \approx \frac{\nu}{\sqrt{E}} \tag{2.11}$$

This is the proportion of the neutral beam that is ionised at zero offset from central axis where ν, the ionisation constant, is given in table 2.2

Table 2.2

Neutral Beam	Ionisation constant, ν		
	Hydrogen	*Nitrogen*	*Argon*
Continuous	42	112	189
CPNB	42	112	189

As expected, the proportion of ionised particles is greater for lower neutral beam energies as the interaction time is maximised. There is also no advantage of a CPNB over a continuous beam. This is expected considering the relative magnitudes of the ionisation cross sections compensated only by a nominal increase in observed proton beam flux. The prospect of a CPNB shall therefore be disregarded.

The minimum ionisation proportion for an atomic Hydrogen neutral beam can be calculated by considering the upper energy limit derived in section 2.1 and plotted in figure 2.2 from which $E_{max} = 1.8$ MeV. This yields a minimum ionization proportion of $\sim 1.41 \times 10^{-5}$ below which interference with the detector will occur. These findings can be further elaborated upon by referring to equation 2.10 and plotting the proportion of the neutral beam that is ionised. This is done by applying equation 2.10 to the product of the proportion calculated in figure 2.7a and the total flux ϕ for the associated electron/proton. This model is shown in Figure 2.8.

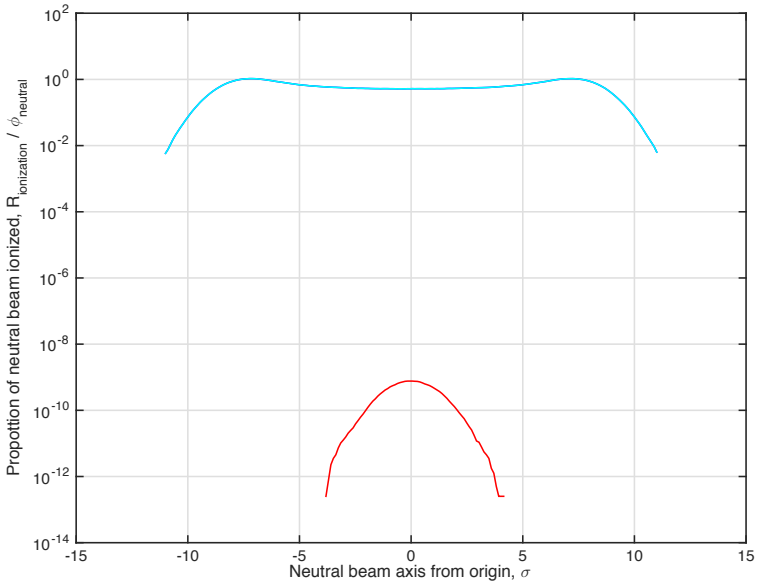


Figure 2.8: Plot showing the proportion of neutral beam that is ionised (by protons in red and by electrons in blue) for beam radius $r = 1\sigma$ and $E = 100$eV

In figure 2.8 the neutral beam energy E has been set such that the neutral beam is fully ionised at its maximum point. Therefore, this value of energy, set as 100 eV represents the minimum neutral beam energy to yield a distinguishable profile during detection. It can therefore be concluded that for a neutral atomic hydrogen beam with radius $r = 1\sigma$ the following condition must be satisfied:

$$100\text{eV} < E < 20\text{MeV} \tag{2.12}$$

With optimal performance towards the lower energy bound. This allows us to set a safe design energy of 500eV for the neutral beam.

2.3.2 Proton beam signal

It is clear from figure 2.8 that the ionising effect on the neutral beam of the proton beam is small. More precisely, the ionising effect is a magnitude of up to $10^{12}\times$ smaller than that of the electron shell. The proton beam signal is so small such that, unless ultra sensitive detection is available, the proton beam ionising effect is indistinguishable from the total profile which is dominated by the electron shell ionising effect.

This effectively means that to distinguish electron shell profile information from the neutral beam little signal analysis is required. However, an alternative method must be conceived through which the proton beam profile can be determined. This will be the focus

of the next chapter which will explore the prospect of Beam Induced Fluorescence (BIF) monitoring.

2.4 Beam shape

The ability to detect fluorescent photons raises the question: why use a thin pencil beam rather than a gas curtain? Gas curtains have already been successfully implemented in synchrotrons albeit exclusively to attain single proton beam profiles [14]. A ribbon beam could be realistically implemented within the required energy range across both beam cross sections as shown in figure 2.9. The problem with a ribbon beam is that it would no longer be possible to detect the neutral gas flux deficit because of the lack of spatial information yielded through a curtain beam. The method would rely entirely on fluorescence to attain the proton and electron beam profiles. Since the proton beam fluorescence will be substantially weaker than that of the electron shell this raises difficulty in detection and profile separation as discussed in chapter 5.

Continuing to use a thin neutral beam will allow for measure of the flux deficit post-interaction to attain a profile of the electron shell. Additionally sensitive, calibrated CCD cameras can be implemented to detect only the fluorescent contribution the proton beam allowing for profile reconstruction.

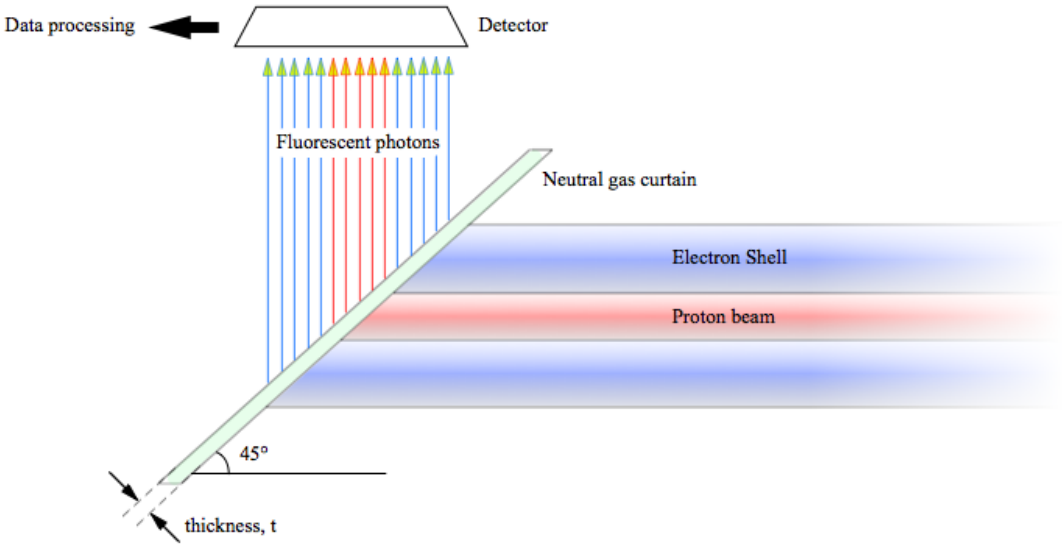


Figure 2.9: Scheme of a gas curtain BIF monitor as evaluated in this chapter.

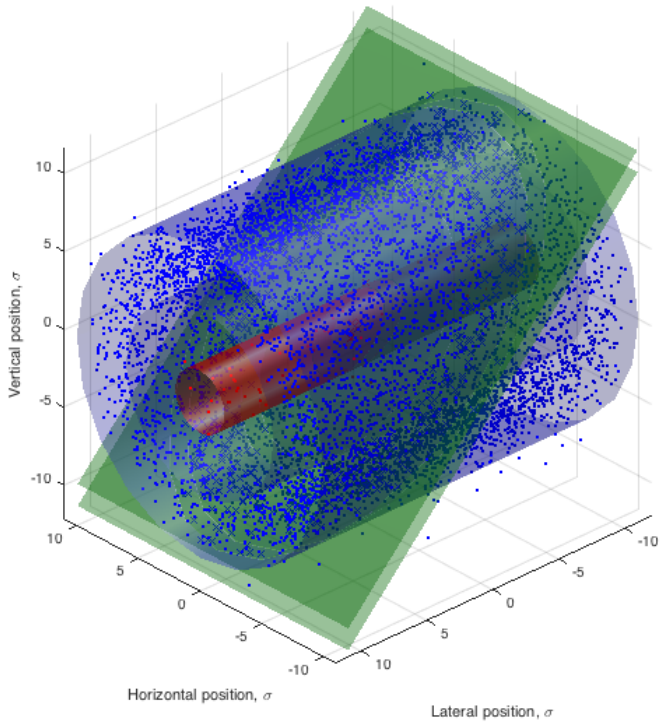


Figure 2.10: MATLAB simulation of 45° gas curtain interception of beams.

2.5 Fluorescence

As covered in Chapter 4 current foil and photomultiplier technology do not allow for signal amplification of up to 10^{12} as required to distinguish the proton signal, shown in figure 2.8. Additionally noise in the signal will cause difficulty in computationally distinguishing both beam profiles from each other.

An alternative method for differentiating the proton and electron beam signals would be to detect fluorescence caused by interaction between neutral atoms and both beams. The following sections will consider the fluorescence emitted during ionisation of the neutral atoms. This fluorescence can be detected using a CCD camera as will be discussed.

In section 2.3 it was found that the proportional ionisation of a neutral beam by the proton beam relative to the surrounding electron shell is small. However, given a neutral beam where the gas density/flux is sufficiently large, it was discovered that ionisation events will occur due to the proton beam.

This section will focus on how we are able to detect individual ionisation events caused by the proton beam opposed to having to detect a flux deficit as done in the previous section. It is known that image intensified CCD cameras are available which can detect indi-

vidual photons. The challenge becomes extracting only the profile of the proton beam and removing any contributions from the electron beam.

Considerable research and development has been conducted around residual gas monitors which measure the ionising effect on trace amounts of gasses, usually Nitrogen, within the vacuum chamber. Through supplementary injection of Nitrogen, signal strengthening and image processing it is possible to attain accurate beam information. Figure 2.11a shows beam profile data from various gasses. It is clear that it is possible to distinguish the position of the beam. Regarding the nature of the gas it is shown that for gasses besides Helium the profile reading will be equal. The use of an atomic Hydrogen beam remains feasible.

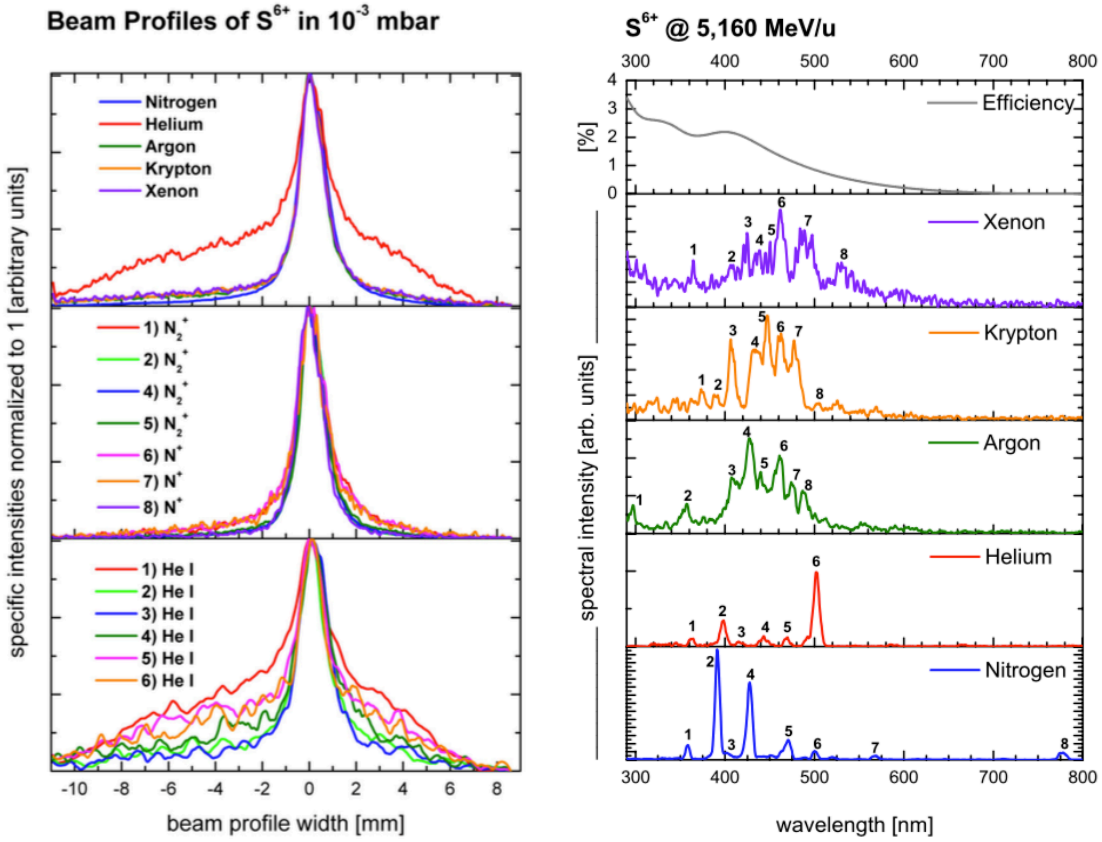


Figure 2.11: Beam profile data yielded from various gasses [6]

This technique is commonly referred to as Beam Induced Fluorescence monitoring (BIF) and was first conceived for low energy beams in Los Alamos in the late seventies. The principle is that collisions between the gas and hadrons causes excitation within the internal energy levels of the gas atoms. Upon returning to the low-energy state, photons are emitted at a particular frequency depending on the internal configuration of the gas atom. Using

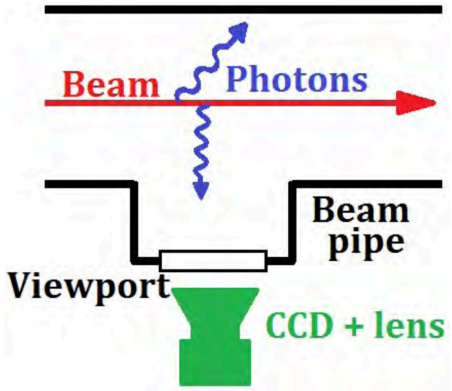


Figure 2.12: Configuration of a BIF monitor [17]

Nitrogen gas, for example, produces a blue fluorescent profile in the visual frequency range, as shown in Figure 2.11b. The reaction lifespan is in the vicinity of 60 ns and causes minimal energy loss of the projectile beam. The main concern is that light production will be too low to detect at energies beyond several MeV despite a study for HERA [15, 16].

To yield an impression of the relative magnitudes of the fluorescent signals the determining parameters must be considered. The parameters affecting the fluorescent signal R_γ are given by the following expression [17]:

$$N_{photon} \propto \frac{dE}{dx}\Delta x \cdot p \cdot \frac{I_{beam}}{q_e} \cdot \frac{\Omega}{4\pi} \cdot \frac{f}{h\nu} \tag{2.13}$$

Where $\frac{dE}{dx}\Delta x$ is the energy loss of the ions with charge q_e in an observable length Δx and pressure p, $f \sim 1\%$ the fraction of the light conversion to $h\nu$ and Ω the solid angle converted by the CCD.

It is noted that the energy loss is also described by the following relationship [18]:

$$\sigma_{ion./phot.} \propto \left(\frac{dE}{dx}\right) \tag{2.14}$$

Considering all other factors besides the energy loss in equation 2.13 to be the same for both proton and electron beams, it can be assumed that the relative fluorescent signal strength is determined only by the ratio of ionisation cross sections for each beam, $\sigma_{ion./phot.}$. This relationship makes sense as we expect the photon flux to be proportion to the number of ionisation events. This means that the relative ratio of photons emitted due to the proton beam and electron shell is equivalent to that given by the ratio of ionisation as shown in figure 2.8 of section 2.3.1.

2.5.1 Proton Beam Fluorescence

Equation 2.13 remains a qualitative approximation to gauging beam induced fluorescence. To deduce an order of magnitude of the fluorescence, experimental data must be consulted. As mentioned in the previous section, the fluorescence is proportional to dE/dx representing the energy loss of the ions in question, in this case protons. Since experimental data only exists below 1 MeV, the Bethe equation which describes the energy loss of a fast ions travelling through matter can be used to estimate energy loss. The Bethe equation is given below [19]:

$$-\left\langle \frac{dE}{dx} \right\rangle = \frac{4\pi}{m_e c^2} \cdot \frac{nz^2}{\beta^2} \cdot \left(\frac{e^2}{4\pi\epsilon_0} \right)^2 \cdot \left[\ln\left(\frac{2m_e c^2 \beta^2}{I \cdot (1-\beta^2)} \right) - \beta^2 \right] \tag{2.15}$$

where in the model v is the proton velocity, x is the proton charge (in multiples of electron charge), c is the speed of light, ϵ_0 is the vacuum permittivity, $\beta = v/c$, e is the charge on an electron, m_e is the rest mass of an electron, I is the excitation potential given by the Bloch equation, $I = (10\text{eV}) \cdot Z$, and n is the electron number density which can be calculated from:

$$n = \frac{N_A \cdot Z \cdot \rho}{A \cdot M_u} \tag{2.16}$$

where ρ is the neutral beam density, Z is the atomic number of the neutral gas, A is its relative atomic mass, N_A is the Avogadro number and M_u is the Molar mass constant. Finally, the relativistic velocity of the proton beam, v used to calculate β, can be calculated from:

$$v = c\sqrt{1 - \left(\frac{m_0 c^2}{E + m_0 c^2} \right)^2} \tag{2.17}$$

where E is the proton beam energy and m_0 is the rest mass of a proton.

Combining equations 2.15, 2.16 and 2.17 for Nitrogen yields the result shown in figure 2.13.

As shown in figure 2.13 a proton beam with an energy of 7 TeV yields a fluorescence of around $185\times$ less than at 200 KeV where the majority of experimental data is available. It can be deduced from this that at 7 TeV the photons from the proton beam will be detectable with a sensibly designed and calibrated CCD camera.

A feasibility study on fluorescent monitors to image high intensity proton beams was conducted at the SPS in 1998 [20].

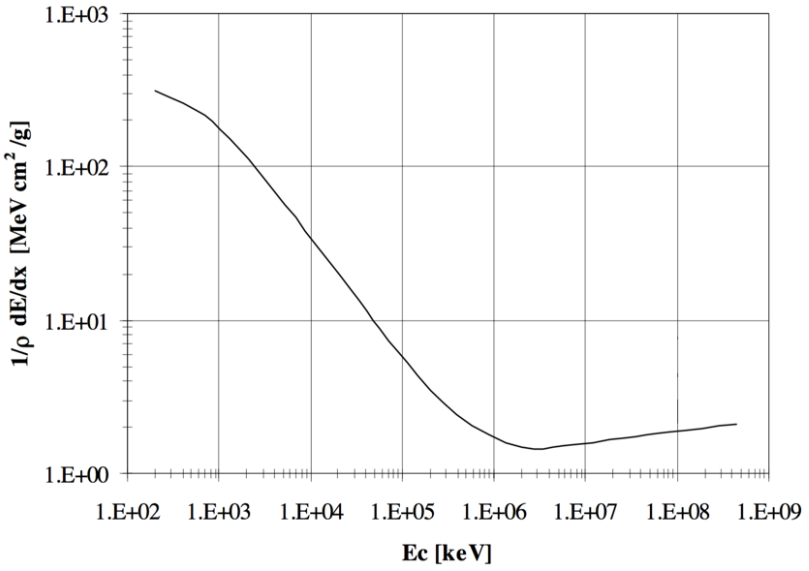
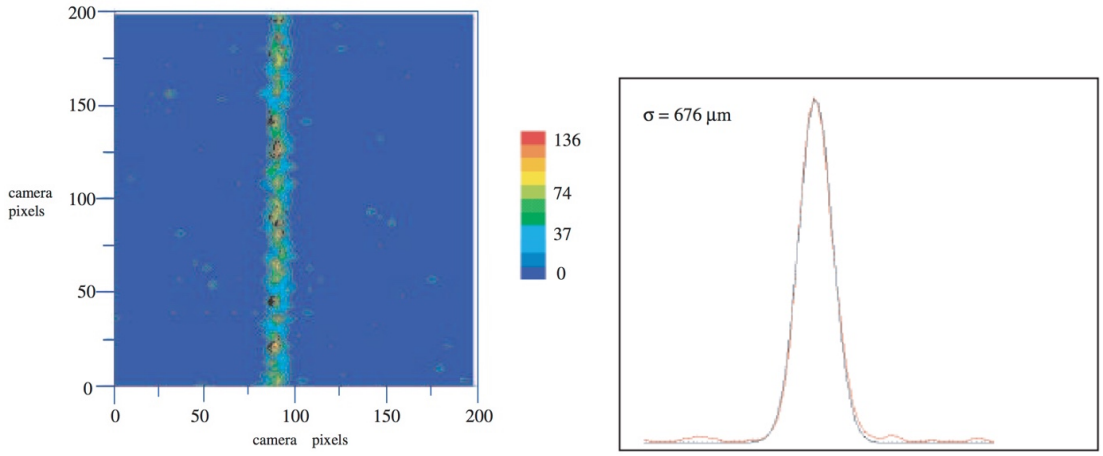


Figure 2.13: Normalised proton energy loss to Nitrogen as a function of proton beam energy given by Bethe equation [16].



(a) (b)

Figure 2.14: Experimental data conducted on a proton beam with properties: $\sigma = 676\mu$, $I = 140$ mA, 2×10^{13} protons, beam energy $= 450$ GeV, and nitrogen pressure 5×10^{-7} Torr with a Gaussian curve fitted to vertical profile [21].

2.5.2 Final Proposal

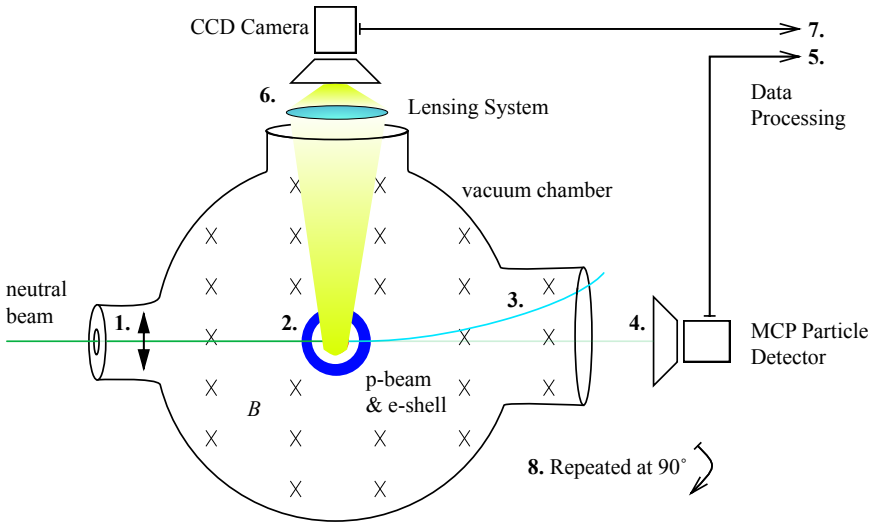


Figure 2.15: Representation of overall beam diagnostic configuration in one axis as described in section 2.5.2.

Following the research and analysis conducted in this chapter the initial proposal has been modified to attain the best possible profile information:

1. A thin beam of neutral gas atoms (neutral beam) as shown in Figure 2.15 is scanned linearly across the cross-section of the proton beam and electron shell.
2. The neutral gas atoms upon interaction with high velocity electrons or protons will become ionised.
3. Upon ionisation the particles are deflected away from the axis of the neutral beam due to electric and magnetic field influences already present within the vacuum chamber.
4. The gas atoms that are not ionised by a proton or electron continue on a straight trajectory towards a detector placed at the opposite end to the neutral beam source.
5. The detector measures the proportion of the neutral gas atoms that arrive unaffected by the protons and electrons with respect to position of the neutral beam. This profile should represent the inverse of the electron shell profile.
6. An optimised CCD camera is positioned perpendicular to the neutral beam axis and captures photons emitted due to the ionising effect of the proton beam only.
7. Image processing of the luminosity from the CCD camera along with neutral beam position allows reconstruction of the proton beam profile.

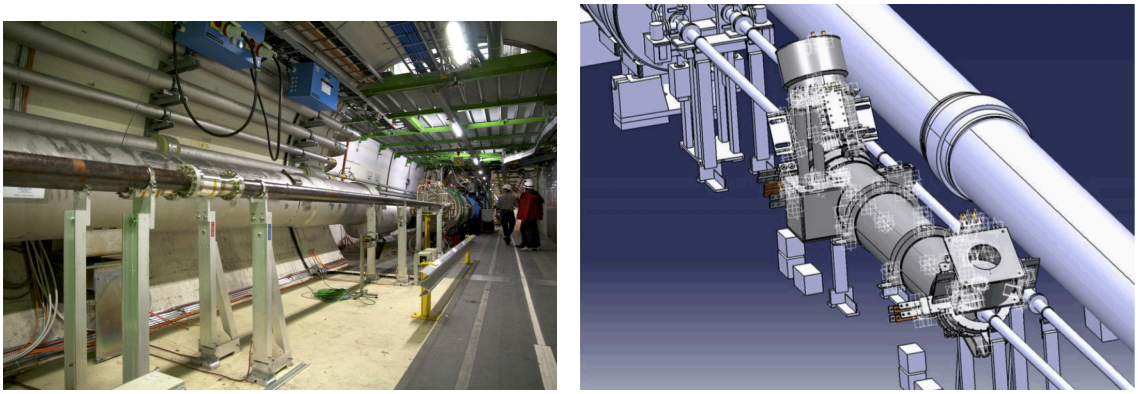
8. The process is repeated along two axes to yield corresponding x and y profiles. The process is repeated at a frequency of 60 Hz to yield an *in-situ* model of the beam for use in calibration of the electron collimator. The reconstructed profiles from both beams are combined to give relative beam position information.

2.6 Overall Device Design

Now that an understanding has been established of how beam profile information can be attained as per the specification, the design phase can be initiated. In the design it is important to carefully consider the availability of space, compatibility with the collimator (UHV conditions, Fields etc.) in which it will be installed and availability of resources e.g. power, cooling fluids, gas. The individual design for the neutral beam generator and detection systems will be addressed in the next chapters.

2.6.1 Location

The diagnostic tool would be situated within the beam collimator. The current candidate locations within the LHC are shown in figure 2.17. A photograph of the candidate location as well as a CAD representation of the collimator installed on the LHC beam is shown in figures 2.16a and 2.16b respectively.



(a) (b)

Figure 2.16: Photograph of the candidate location RB-46 from Figure 2.17 and CAD representation of implementation [1]

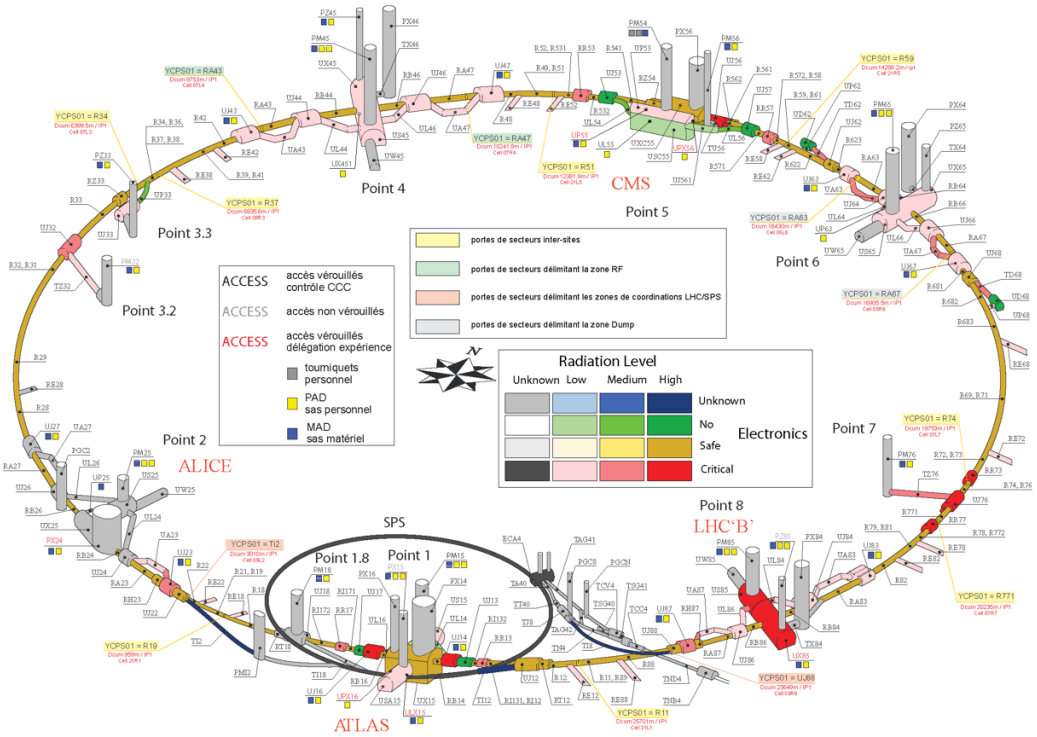


Figure 2.17: Candidate positions for the electron lenses are RB-44 and RB-46 at Point 4 [1]

2.6.2 Integration with Collimator

From the CAD renderings cited in figure 2.16b a 3D model of the electron lens and collimator have been reproduced as an aid for design. This is shown in figure 2.18. This model will help to decide upon the most suitable method of integration of the neutral diagnostic beam and relevant detection equipment.

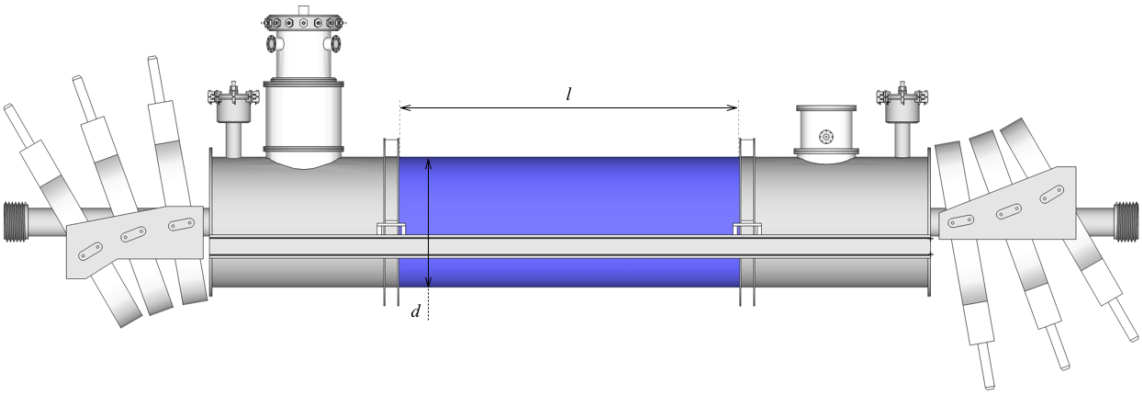


Figure 2.18: CAD model of electron lens with intended diagnostic observation region highlighted in blue where $l \approx 1010$mm and $d \approx 480$mm.

Within the observation area two identical diagnostic setups must be fitted perpendicular to each other such that the beam can be imaged in both axes and at $\pm 45^{\circ}$ to the horizontal so as not to interfere with the neighbouring beam shaft pictured in figure 2.16b. Each setup will contain three main components: a neutral beam generation unit, a neutral beam detection unit and a fluorescence imaging unit. The neural beam detection unit, as described in chapter 4, must be installed opposite the neutral beam generation unit. The fluorescence imaging unit, as described in chapter 5, must be installed perpendicular to the neutral beam axis. The three units require three openings looking into the beam chamber. All openings must be able to cope with UHV conditions.

The approximate dimensions for each unit is given in table 2.3.

Table 2.3: Approximate unit dimensions

Unit	Size (mm)	Colour
Neutral beam generator	Neutralisation chamber - 700×600(diam.) Ion source - 250×750	orange yellow
Neutral beam detector	$200 \times 140 \times 60$	blue
Beam fluorescence detector	$100 \times 100 \times 250$	green

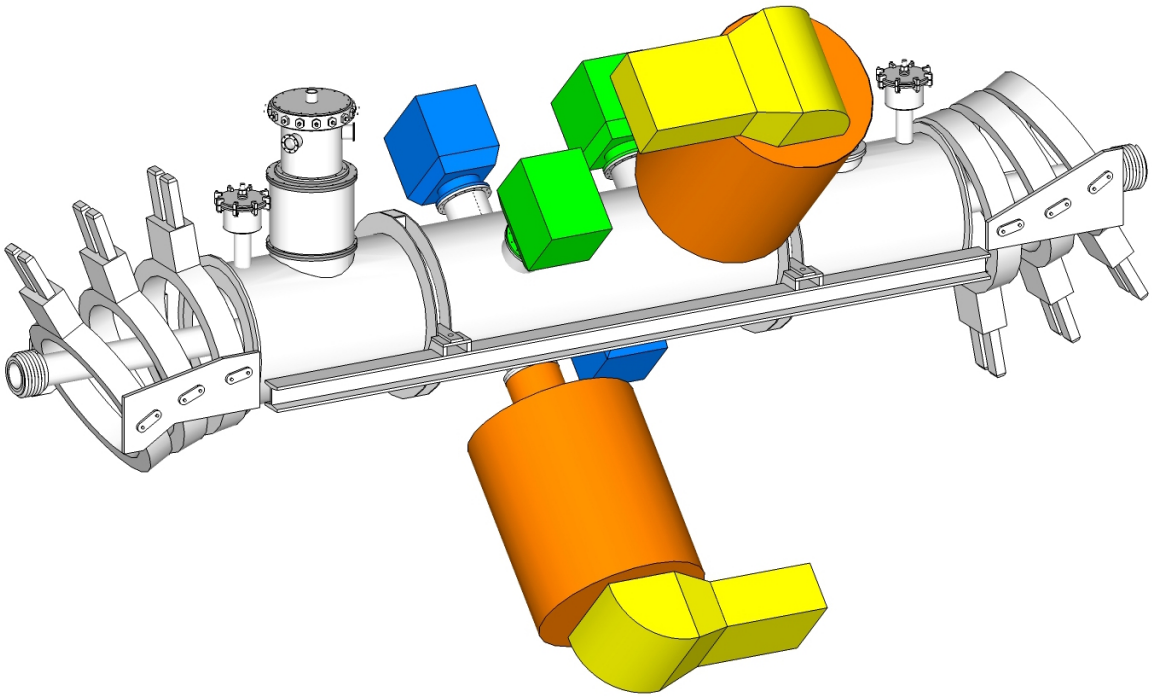


Figure 2.19: CAD representation of diagnostic configuration with constituent elements defined in Table 2.3.

2.6.2.1 Neutral beam generator

Two neutral beam generation units will be installed on the observation area, both perpendicular to each other. Since the neutralisation section of the beam generator will also be under UHV conditions there is no requirement for a seal between the beam generator and beam vacuum chamber.

An important consideration is the influence of the collimator's solenoidal magnetic field. Self-evidently the B-field will have no influence on the neutral particles. However, the field may be strong enough to influence the ion beam source within the generation unit. The ion beam source, as made clear in chapter 3, produces a stream of charged ions that will eventually be neutralised and go on to form the neutral beam. Prior to ionisation the ions will be susceptible to the collimator's B-field.

To determine the effect of the B-field on the ion source the strength of the B-field outside of the collimator solenoid must be calculated. This is achieved by approximating the magnetic field to be a uniform solenoidal field with a maximum flux density of 7 T [1]. Figure 2.20 shows an exaggerated field simulation of the B-field around the collimator solenoid.

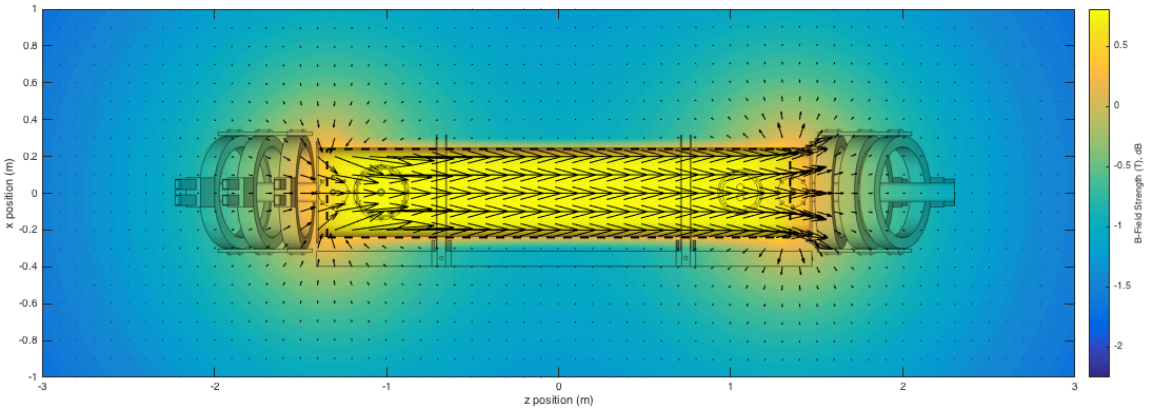


Figure 2.20: MATLAB B-field simulation around collimator solenoid with superimposed CAD outline of collimator.

From the simulation we can estimate the field strength at the proposed position of the ion source corresponding to $x \approx 0.94$m ($\sim (700 + 240)$mm from the centre line) to be $B \approx 0.070$T.

There are a number of ways in which the effect of the B-field on the ion source can be reduced including:

- Introducing magnetic shielding to the ion beam generator such as Faraday caging.

- Ensure that the ion beam path is as far away from the electron lens solenoid as possible to reduce the magnitude of B.
- Ensure that the ion beam path is parallel to the B-field direction such as the perpendicular B-field component is minimised.

Since Faraday caging is not possible (continuous B-field) and the second option of increasing the distance from the electron lens solenoid is not practical, the remaining option is to adjust the angle of the ion beam generator such that it lies parallel with the B-field direction. This has been incorporated into our final design model in figure 2.19 where the ion sources in question are shown in yellow.

2.6.2.2 Detectors

The neural beam detector and beam fluorescence detector, as outlined in chapters 4 and 5 respectively, will require a view port into the beam chamber. The view-ports must be able to withstand UHV conditions up to 10^{-11}mbar, temperature variation and intense magnetic fields. Vacuum compatible view ports are considered standard LHC components and are custom produced on-site.

2.6.3 Technical Specification Summary

From the analysis in this chapter the following design specifications are proposed for the neutral beam to optimise performance.
Table 2.4 below shows a summary of the chosen parameters.

Neutral Beam Composition	Neutral Atomic Hydrogen
Neutral Beam Energy	500eV
Beam Current	10mA
Beam Shape	Round Pencil Beam
Beam Radius	1σ where $\sigma = 1$mm
Beam Format	Continuous
Beam Scan Frequency	60Hz

Table 2.4: Neutral Beam Parameters

Chapter 3

Neutral Beam Generation

Neutral particles are unaffected by both electric and magnetic fields. Therefore, when scanning a neutral particle beam across a hadron beam, in spite of the strong magnetic field present, the neutral beam only interacts with the hadrons. This quality which prevents interference of the scanning beam also makes its generation and acceleration difficult. In section 2.3.1 a optimal particle energy of 500 eV was established. At this energy, hydrogen atoms will be accelerated to a velocity of 3.1×10^5 ms^{-1} and helium atoms will be accelerated to a velocity of 1.6×10^5 ms^{-1}.

3.1 Generation Methods

This section explores the general methods available for generating an accelerated neutral beam. The chosen method is explored first and the remaining methods are briefly described and an explanation is given for why they are not used.

3.1.1 Negative Ion Neutralisation

Generating negative ions is relatively difficult compared to generating positive ions as most atomic species have low electron affinities, and in some species the ions are only metastable. However, for negative hydrogen ions, various ion source architectures have been developed for their use in particle accelerators such as the one in Fermi National Accelerator Laboratory. Hence in this case, the negative hydrogen, H^- ions are the most suitable as they are stable with an electron affinity of -0.754 eV [22].

Once generated, the H^- ions can be accelerated through electrostatics which is trivial, although beam shaping may be more difficult. After this, the beam will have to be neutralised. The ionisation electron can be removed *via* two main methods. The first is through collisions with neutral atoms or molecules and the second is through photo-detachment.[23]

In the case of neutralisation by gas collisions, the process is a passive one and no further addition of energy is required. The ion is neutralised as follows:

$$H^- + H_2 = H + H_2 + e^- \tag{3.1}$$

However, the accelerated neutral atom can then undergo a second collision to create a positive ion in reionisation:

$$H + H_2 = H^+ + H_2 + e^- \tag{3.2}$$

This is undesirable as it reduces the overall production of neutral particles. Furthermore, multiple collisions would add momentum uncertainty to the neutral atoms, which is undesirable for a precision neutral beam. Hence, this method was unsuitable for this context.

For neutralisation *via* photo-detachment, photons interact with the outermost electrons of the H^- ions, and if the photons contain sufficient energy, an electron would escape the ion as a photo-electron, producing a neutral atom. This method requires additional energy in the form of illumination but does not add momentum uncertainty to the generated neutral atoms and if the photon energy is correctly selected, will not wastefully produce positive ions. For these reasons, this method was ultimately chosen.

3.1.2 Positive Ion Neutralisation

Positive ions are more easily generated than the negative ions but are harder to neutralise. Ion production can be achieved via many established ion source architectures, such as the Penning Gauge and Magnetron. Hence, the production of ions is relatively easy and the ions can be accelerated *via* electrostatics.

The first method one can consider is to let the ions pass through an electron plasma. In this particular method, ion-electron recombination rates can be low. This is compounded by reionisation of neutralised atoms when atoms of sufficient energy collide with electrons.[24]

The second neutralisation method is to allow the ions to collide with neutral gas particles of the same species causing a charge transfer process. Similar to the related method with negative hydrogen ions, this method has problems of reionisation and momentum uncertainty and is similarly unsuitable.

3.1.3 Accelerated Neutral Atom Beam (ANAB)

Exogenesis[25] developed a method for generating an accelerated neutral beam, ANAB. It is a modification of the Gas Cluster Ion Beam (GCIB) methodology. In the process, gas clusters are produced by specialised nozzles. These gas clusters then have a few of their member atoms ionised, giving the entire cluster a small overall charge while still maintaining

a majority of neutral atoms. These partially ionised gas clusters are then accelerated *via* electrostatics and passed through a chamber of gas atoms.

Upon collision with an atom in the gas chamber, the gas cluster would dissociate, releasing the neutral atoms from the ions. The ions can then be deflected and dumped while the neutral atoms would continue on its original path. This process has only be implemented in a single product by the company, the nAccel 100 unit which is used in semi-conductor fabrication[25]. Exogenesis was contacted about adapting their technology for the neutral beam generation. However, a representative from the company stated that the current technology limits beam energies to 100 eV. Hence, this technology is not suitable for this application.

3.1.4 Quantum Gas Jet

A thin pencil gas jet of neutral atoms/molecules can be generated by using pressure differentials to accelerate a gas followed by using the gas particle's De-Broglie wavelength to focus the atoms through an "atomic sieve". Unfortunately, this method is unable to produce neutral particles of sufficient energy for this application. While supersonic gas jets can be generated *via* pressure differentials, they still fall far below the specified requirements. For example, the maximum velocity achieved by researchers in 2001 was 1000 ms^{-1} for helium, two orders of magnitudes smaller than in the project specification. [26]

3.2 Negative Hydrogen Ion Source: Penning Ion Gauge

The various sources available to produce H^- ions can be categorised into surface sources and volume sources. In general, volume sources can produce higher beam currents than surface sources, but are also larger and have more complex architectures. As the system specification has a size limitation and large beam currents are unnecessary, surface sources are considered over volume sources. In particular, the Penning Ion Gauge(PIG) is proposed for the system.

3.2.1 General Mechanism

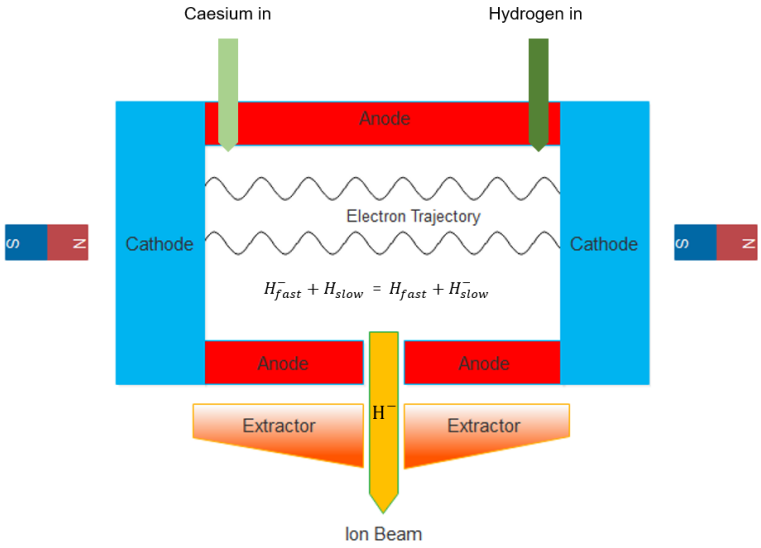


Figure 3.1: A 2-D representation of the Penning Ion Gauge

In the Penning Ion Gauge(PIG), a cylinder is formed by the cathodes at the two ends and the anode being the curved surface. An extractor is placed in the anode wall, normally equidistant from the cathodes. The cathodes produce electrons which are repelled away, travelling down the cylinder. The PIG cylinder is fed with hydrogen gas, which on collision with an electron, undergoes one of the following reactions:

$$e^- + H_2 = H^- + H^+ + e^- \tag{3.3}$$

$$e^- + H_2 = H^- + H \tag{3.4}$$

To increase the collision and hence reaction rate, a magnetic field parallel to the length of the cylinder is also set up. The lengthwise magnetic field causes any electrons with a

non-lengthwise velocity component to travel in a helical path towards the other cathode. This increased the total path travelled within the hydrogen gas and hence increases the production of ions. In the above reactions, positive H^+ ions are also produced. These ions are accelerated towards the cathodes by their electric fields. Upon impact with the metal cathode surface, metallic electrons tunnel from the cathode to the ions to produce either hydrogen atoms or negative hydrogen ions as follows:

$$2e^- + H^+ = H^- \tag{3.5}$$

$$e^- + H^+ = H \tag{3.6}$$

These processes can be made more frequent by coating the surface of the cathodes with caesium, increasing ion beam current. The caesium coating lowers the work-function for the electron tunneling process, increasing the probability of negative ion production per ion impact. The optimal caesium layer thickness is 0.6 monolayers which lowers the work-function to 1.5 eV from 4.6 eV[27]. The produced H^- ions are accelerated by electrostatic repulsion away from the cathodes they were produced at. These negative ions have a significant velocity variance due to differences in where the ions are produced and their subsequent acceleration. This velocity variance makes them non-ideal for extraction and use. With the extractor placed along the anode walls, their extraction becomes unlikely. Ridges preventing line-of-sight from the cathode to the extractor can be utilised to further reduce the probability of extraction of fast ions.

Instead, these fast ions can undergo a resonant charge exchange with slow thermal hydrogen atoms in the volume of the PIG, producing slow thermal H^- ions[28].

$$H^-_{fast} + H_{slow} = H_{fast} + H^-_{slow} \tag{3.7}$$

The slow thermal ions produced near the extractor can then be easily extracted with a low velocity variance. At the specified ion energies of 500 eV, the extractor can be designed to accelerate the beam to its needed energy without the need for a post-accelerator.

3.2.2 Practical Concerns

To extract the H^- ions an electrostatic field is used, with the extractor electrodes having a higher electric potential than the PIG plasma. This accelerates all the negatively charged particles near the extractor out, while repelling positive ions back into the PIG. As both the desired H^- ions and plasma electrons share the same charge, they will be co-extracted by the electric fields. Furthermore, the electron population will be larger than the H^- population, sometimes by an order of magnitude. Another issue that may arise is the diffusion of

caesium vapour from within the PIG source as they are uncharged and hence not contained by the electric field.

3.2.2.1 Electron Co-extraction

The large population of electrons within the extracted beam harms the beam quality in two ways. Firstly, electron-H^- collisions can result in the collisional detachment process[27]:

$$e^- + H^- = H + 2e^- \tag{3.8}$$

This greatly reduces the H^- density within the beam, worsening with the length of path shared by electrons and the H^- ions. Furthermore, the electrons increase the total charge density of the combined ion-electron beam while not improving the number of useful H^- ions. This strengthens space-charge effects which can express itself as increased beam divergence.

To maintain beam quality, the co-extracted electrons need to be removed from the beam as soon as possible after extraction. This can be achieved by bending the combined beam through 90 degrees with a magnetic field. While the electrons and H^- ions share the same particle energy, the electrons have a mass 3 orders of magnitude smaller than the H^- ions. Hence, electrons will have a much faster speed than the ions. Equating magnetic force with centripetal force:

$$Bqv = mv^2/r \tag{3.9}$$

where B is the magnetic field, q is the electron charge, m the mass of the particle and r the radius of circular motion. By neglecting relativistic effects, the above can be arranged to an expression for the rotation radius in terms of the energy:

$$r = \sqrt{2mE}/Bq \tag{3.10}$$

It is clear from the above that with identical charge, energy and magnetic field, the radius of the electrons' motion will be approximately 43 times smaller than that of the H^- ions. Therefore, controlling the geometry of the bending chamber and the magnetic field, the electron and H^- ion beams will naturally separate and then the electron beam can be dumped. The electron dump would require cooling to prevent localised heating which may damage components.

3.2.2.2 Caesium-induced Breakdowns

Caesium can promote high-voltage breakdown if it reaches a high voltage surface. As the ion-lenses used further down the beam path may require high voltages, this can potentially

become a hazard. Some existing H^- ion sources solve this issue by having a cold box right after the source along the beam path. Here, the cold box allows any caesium vapour that escapes from the ion source to condense onto the cold surface, trapping it before it can diffuse down the beam path. This can be easily implemented alongside the electron dump as both systems can share the same cooling system[29].

3.2.3 Design Choices

3.2.3.1 Penning Ion Gauge vs Other Sources

The Penning Ion Gauge as an ion source is relatively compact compared to volume sources. In fact, most examples of surface sources such as the PIG and magnetron have dimensions within 20 cm$\times$20 cm$\times$20 cm, which is ideal given the limited space available in the application context. Within the surface sources, the PIG architecture was chosen over the magnetron architecture as the PIG is able to produce ions at higher duty factors, and even at continuous beam. This is due to the cathodes being accessible externally, and so can be cooled to allow for longer active periods without cathode damage from ion-impact heating. Another advantage of the PIG over the magnetron is its lower ion traverse energy at output as only thermal ions are extracted. This reduces beam emittance which improves beam quality[30].

3.2.3.2 Geometry and Magnetic Field

The geometry of the PIG ion source is small and may change with optimisation. To design the minutiae of the source goes outside the scope of this report; such development would require experimental feedback to optimise the source designs. Nonetheless, a safe assumption on the basic geometry is that the source would be contained by a cylinder 20 cm long with a 10 cm diameter.

This ion source will output into a cold-box caesium trap with a magnetic field parallel to the axis of rotation. As the beam-pipe further down has an external diameter of 50cm and requires the ion beam to be positioned at its centre, the design turning radius is 25cm. Given a design beam energy of 500 eV, this corresponds to a magnetic field strength of 0.01293T(4s.f.) from equation 3.10. A metal tube that follows the beam as it travels from the source will provide additional surface area for both the caesium atoms and the electrons to be adsorbed onto.

3.2.3.3 Further Development and Concerns

In designing the ion source, a few parameters need to be experimentally tuned. These are the hydrogen gas input flow rate, caesium input flow rate, source plasma and cathode temperatures, and the cold box temperature. These will have to be tuned to optimise the ion production rate. The extraction electrodes will also have to be designed to best optimise for beam divergence. There exists the Pierce Geometry which can focus the extracted ion beam into a parallel beam upon extraction should the ions be surface emitted at extraction. However, in our application, the ions will be extracted from the plasma with varying starting conditions[31]. This limits the usefulness of this electrode geometry. Hence, further design is needed on the extractor.

A common issue with the Penning Ion Gauge is that the cathodes erode with time due to ion impact and heating. This results in a limited lifetime ranging from weeks to months[27]. This issue should be kept in mind when the source is developed and used.

3.3 Ion Beam Lensing

In order to obtain useful information about the hadron beam, the neutral beam must scan it with sufficient resolution. This can only be achieved if the neutral beam used is sufficiently small, as specified in section 2.3.1. In order to ensure that the neutral beam is sufficiently small, it would have to be focused prior to neutralisation as an ion beam. However, as the space charge density is increased, so does the repulsion between ions. This is summarised by the space charge effects of the ion beam, which will cause the beam to diverge. When focusing the ion beam, one has to account for this opposing effect. The ion beam can be focused by either electrostatic lenses or magnetic lenses. At high beam energies, magnetic lenses are superior as the lensing magnetic force scales with particle velocity. However, electrostatic lenses are easier to implement, not requiring large currents and cooling. At the design particle energy of 500 eV, electrostatic lensing is preferable.

3.3.1 Electrostatic Lens Basics

One of the basic electrostatic lenses is the immersion lens. It consists of of two electrodes with a potential difference $\Delta V = V_2 - V_1$ between them. The electric potentials can be set up as either an accelerating or decelerating lens which changes the particle energy while focusing the ions according to the focal length as given:

$$\frac{f}{L} = \frac{4(\sqrt{V_2/V_1} + 1)}{V_1/V_2 + V_2/V_1 - 2} \tag{3.11}$$

where f is the focal length and L the distance between the electrodes[31].

3.3.2 The Einzel Lens

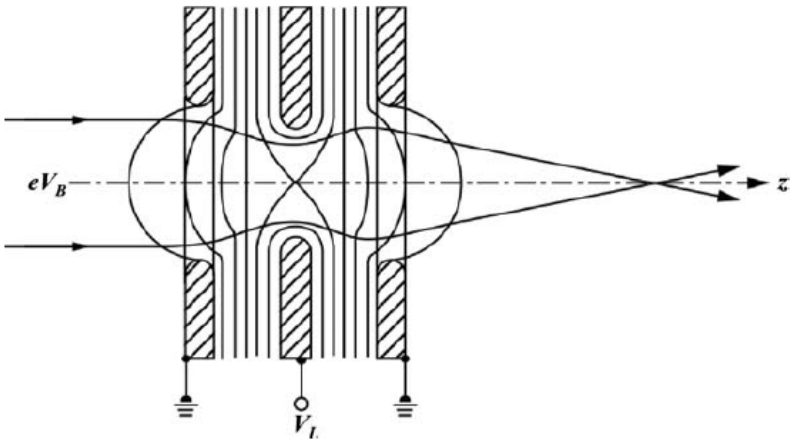


Figure 3.2: 2-D representation of an Einzel Lens focusing a beam[32]

Two such immersion lens can be combined into a three-electrode Einzel lens. In this this layout, the two end electrodes share the same beam-line potential V_0 and the middle lens have a different voltage V_L. Einzel lenses are focusing lenses and the focusing strength of the lens is determined by two sets of parameters. The first parameter is the mode of the lens. If the middle electrode potential is such that the ions in the beam are accelerated towards it, the lens is in a accelerating(accel-decel) mode, while if the ions are accelerated away from the middle electrode, the lens is in a decelerating(decel-accel) mode. The second parameter is the ratio of the middle electrode potential,V_L to the beam energy,$(e)V_B$. Together they control the focusing power of the Einzel lens.[32]

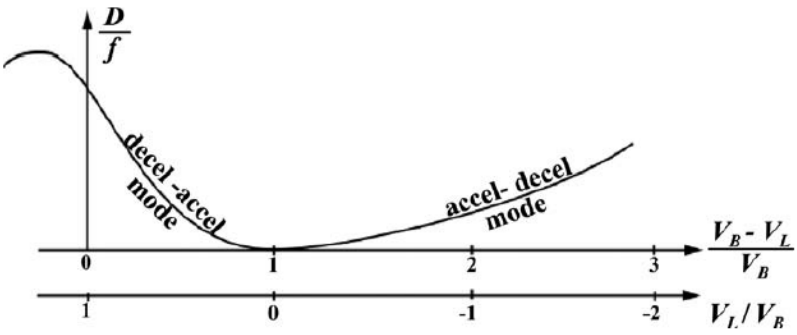


Figure 3.3: Graph of Einzel lens focusing strength against voltage ratio[32]

3.3.3 Focusing Lens Design Considerations

A desirable quality of the Einzel lens is that it does not change energy of the beam it focuses. While the particle does gain energy moving towards the centre electrode, it proceeds to lose

the gained energy as it moves away from it. Where ion velocity control is important, the ability to vary focusing power without affecting the ion speed is a very useful trait. For this reason, the Einzel lens was chosen as the focusing method. In particular, the Einzel lens would be implemented as concentric cylindrical electrodes in series to ensure symmetric focusing.

3.3.3.1 Einzel Lens Mode

Comparing the Einzel lens modes, the decelerating mode has stronger focusing power for the same voltage ratio. However, it also has larger chromatic and spherical aberrations. For the relatively low ion energy used, it is more desirable to use the accelerating mode as the necessary potentials are attainable. This results in smaller aberrations in focusing the ion beam. For these reasons, the accelerating mode of the Einzel lens was chosen. It should be noted that even with the accelerating mode, spherical aberrations will not be eliminated, resulting in a finite beam size that the ion beam can be focused to.

3.3.3.2 Centre Lens Electrode Potential

Choosing the focusing power of the Einzel lens is of utmost importance when controlling the size of the outputted neutral beam. A naive approach would be to focus the beam such that the focal length would coincide with the centre of the hadron beam pipe that is being scanned. This approach limits the maximum spread of the resultant ion beam evenly across the the hadron beam. However, this method neglects space charge effects that attempt to disperse the H^- ion beam even as the Einzel lens focuses it.

Accounting for space-charge effects, perfect focusing action will result in the H^- ion beam becoming parallel just as it is neutralised, forming a neutral atom beam with zero divergence. Note that when the beam has been neutralised, space-charge effects are no longer active. The above methodology assumes that the H^- ion beam is entirely neutralised to H atoms at a specified point along the beam pipe. This is not the case. As further described in a later section of the report, the neutraliser consists of a length along the H^- ion beam pipe in which the ion beam will be irradiated by photons resulting in the neutralisation of the ions to atoms. As neutralisation of a H^- ion can occur with varying probabilities anywhere along the length of the neutraliser, the ions are exposed for varying lengths of time to the space-charge repulsion before neutralisation, resulting in differing trajectories. Furthermore, with charge density being reduced by both divergence of the ion beam and loss of charged ions in the beam, the space-charge effects will weaken along the length of the neutraliser [33]. Ultimately, finding the optimal Einzel lens focusing strength

analytically becomes difficult to the point of impracticality and is best approached by tuning *via* experimental calibration.

3.4 Beam Deflection and Scanning

To scan the neutral probe beam across the hadron beam, the probe beam must be deflected prior to neutralisation. Post neutralisation, the H atoms will not be affected by any magnetic or electric field. Therefore, the probe beam must be neutralised while it is still an ion beam. Deflection of the charged ion beam can be achieved by one of two ways, either by electrostatic deflection or magnetic deflection. Similar to the case of focusing described in section 3.3, magnetic deflection is more effective than electrostatic deflection at high beam energies. For the present context of a 500 eV beam energy, the easier to implement electrostatic deflection is more applicable.

3.4.1 Parallel Plate Condenser

The simplest way to implement electrostatic deflection is to pass the ion beam between a pair of parallel plates, each at a different potential. The plates will set up a uniform electric field between them which steers the ion beam. This arrangement is also called a parallel plate condenser.

The deflection properties of the parallel plate condenser can be derived from first principles. Consider a 2-dimensional (x-y) space with the ion beam travelling along the x-axis starting at origin with energy eV_b, and zero initial velocity and acceleration in the y-direction. If the x-axis is at potential V_b with the parallel plates symmetric around the x-axis both in potential and space, the ions will experience a deflection force:

$$qE = my'' \tag{3.12}$$

where m is the ion mass, q its charge. The above expression can be integrated twice with respect to time to give:

$$y' = \frac{q}{m}Et \tag{3.13}$$

$$y = \frac{q}{2m}Et^2 \tag{3.14}$$

Keeping in mind that the x-direction velocity remains unchanged at $v_x = \sqrt{2qV_b/m}$ throughout the process, the time starting from the start of deflection at the origin, is given by $t = x/v_x$[32]. For a deflection plate of effective length L, the total y-direction deflection and velocity at the end of the effective length is:

$$y = \frac{EL^2}{4V_b} \tag{3.15}$$

$$y' = \frac{EL}{2V_b} \tag{3.16}$$

The electric field E is controlled by the potential difference and spacing between the parallel plates, ΔV and d respectively. The approximate relation is given by $E = \Delta V/d$. This relation is approximate as it does not account for fringe fields. To get around the problem, the effective length, L which accounts for the fringe field effects is used instead of physical length. From the above, one can control the deflection of the ion beam via the deflection plate voltages, spacing and lengths.

3.4.2 Angle of Incidence on Hadron Beam

When using a single parallel plate condenser, as long as the output ion beam has a positional deflection, it will not be parallel to its original axis. This deviates from the original design intention of a neutral beam scanning the hadron beam at a fixed angle of incidence. To ensure that the ion beam remains parallel to its undeflected axis for all positional deflection, a second parallel plate condenser in series to the first is proposed. The second parallel plate condenser is to be geometrically identical to the first, with its plate voltages switched. In other words, if the top plate of the first condenser has a potential V_1, the second condenser will have a bottom plate of potential V_1 and vice versa. These two parallel plate condensers will form a matching pair for deflection in one direction. As both parallel plate condensers share the same voltage levels, the second unit can share the same voltage control systems as the first, reducing implementation complexity.

By having two identical deflectors with opposite electric fields, the second deflector will apply to the ion beam an equal but opposite impulse to the first deflector. From first principles, this results in the ion beam having a final y-direction velocity of zero with a non-zero y-direction positional deflection. If the two condensers have no spacing between them, the resultant y-direction deflection will be double that of one condenser alone, as given by equation 3.15. Should a greater deflection be needed, a spacing between the condensers can be introduced, allowing the y-direction velocity from the first condenser more time to deflect the beam positionally. To ensure that the proposed concept will have its intended effect, a simulation was conducted on MATLAB. The PDE Toolbox was used to generate the electric potentials and fields in a 2-D mesh and a MATLAB function, track_neg_H, was written to simulate parallel beam elements. In the model, the ion beam begins centred at the origin and travels along the x-axis with design energy 500 eV. A gap between the condensers was also added to allow for greater positional deflection. Initially, a full size model was attempted, but at the required mesh size for accurate simulation, a full size

model required too much memory to run. It was decided that a reduced model would be sufficient to test the concept. The parameters of the reduced model are tabulated as below:

Deflection Plates Length	0.04 m
Gap Between Condensers	0.2 m
Deflection Plate Separation	0.04 m
Condenser Plate Potential Difference	15 V
Ion Beam Initial Width	0.01 m

Table 3.1: Parameters of model used to test deflection concept

The simulation gave the result in the figure below:

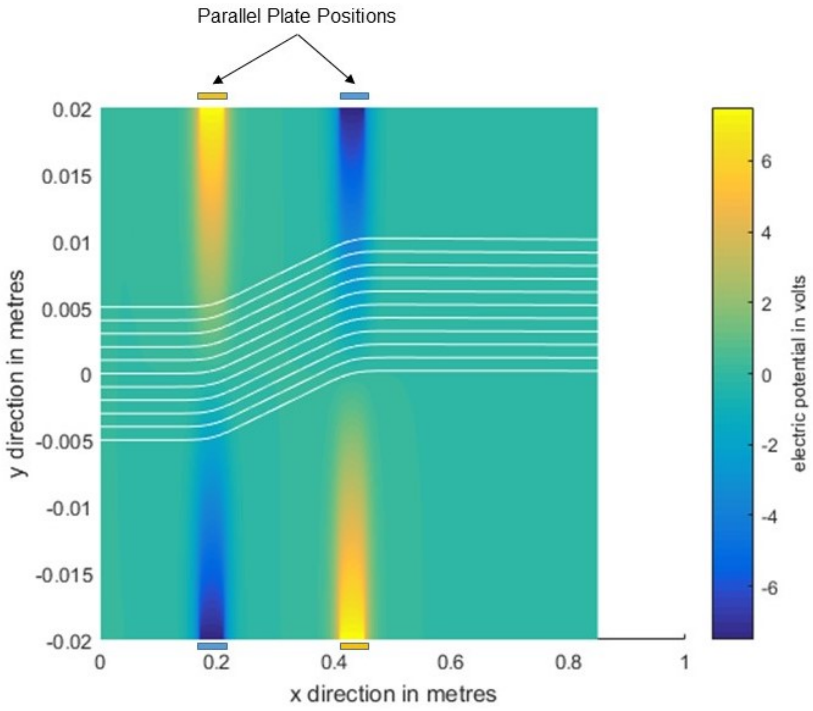


Figure 3.4: Deflection of ion beam with matched parallel plate condensers

The results of the simulation show that the proposed paired-condenser system will have its intended effect of ensuring that the ion beam remains parallel after deflection. Hence this design is feasible.

3.4.3 Effect on Focusing

As both the ion beam focusing and deflection alter the ion beam, there is a possibility of the ion beam losing focus after deflection. A possible work-around is to first deflect the beam into position before focusing the beam. In order for the focusing elements to function

identically for all beam positions, the relative position and velocity of the ion beam and the focusing elements must be maintained. This, however, requires that the ion lens be moved to match the deflection of the ion beam, a process that adds mechanical complexity and uncertainty into the system. Noting that the positional precision needed is high and that the apparatus has to function in a ultra-high vacuum, this approach should only be used as a last result due to its complexity. Hence, deflecting the ion beam after focusing it was investigated first.

3.4.3.1 Simulation of Ion Lensing and Deflection

To test the suitability of deflecting the ion beam after focusing, the MATLAB model used to simulate parallel plate deflection in section 3.4.2 was modified to add an Einzel lens before deflection, keeping all previous dimensions. Although Einzel lenses are made of cylindrical electrodes and hence are 3-dimensional, a 2-dimensional representation is valid for simulation purposes as both the proposed Einzel lens and the expected ion beam are rotationally symmetric about the x-axis. The additional model parameters are tabulated as follows: Noting symmetry about the x-axis, the results are given in figure 3.5. From the

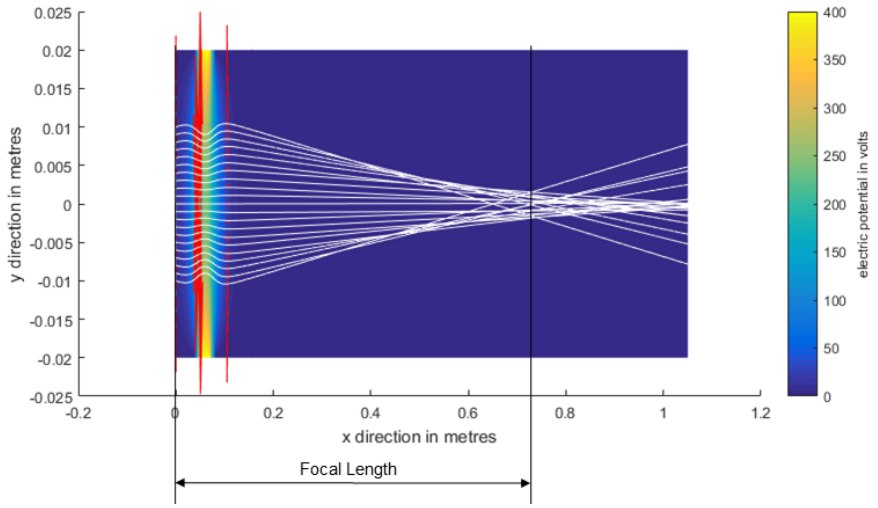
Einzel Lens Plate Separation	0.04 m
Einzel Lens Electrode Gap	0.01 m
Einzel Lens End Electrodes Length	0.04 m
Einzel Lens Middle Electrode Length	0.02 m
Einzel Lens Middle Electrode Potential	420 V
Einzel Lens End Electrodes Potential	0 V
Condenser Plate Potential Difference	0 V, 20 V

Table 3.2: Parameters of model used to test compatibility of deflection after focusing

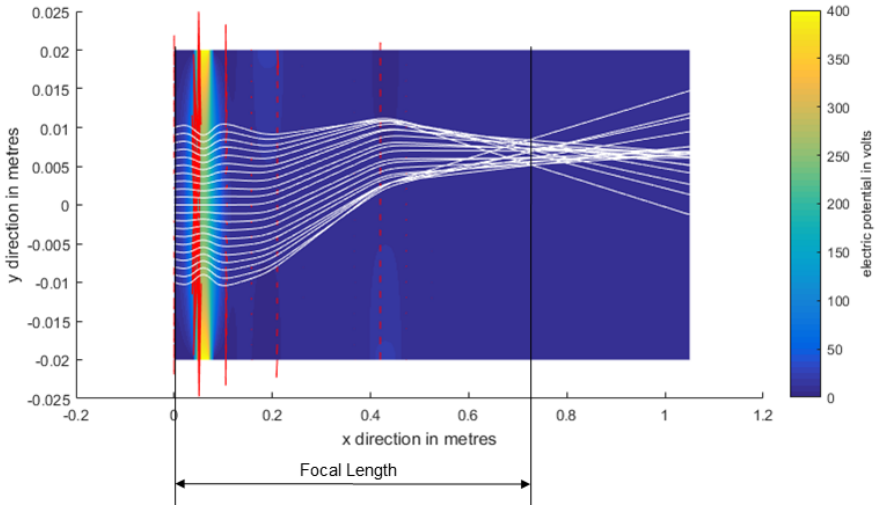
results in figure 3.5, the focal length is unchanged by the deflection process. Hence, having the deflection of the ion beam after focusing is a viable design.

3.4.4 Practical Concerns

For the parallel plate condensers, electric field strength is governed by the equation $E = \Delta V/d$ as mentioned in section 3.4.1. Hence, a stronger field can be achieved by increasing the potential difference or decreasing the plate separation. Increasing the potential difference requires generating higher voltages, with difficulty of generation increasing with voltage. On the other hand, the deflection plates must be adequately separated so that the deflected ion beam will not collide with the plates themselves. For a set deflection



(a) Undeflected focused ion beam simulation



(b) Deflected focused ion beam simulation

Figure 3.5: Comparison of Focal Lengths of Deflected and Undeflected Ion Beam

range, the electric field must be large enough to deflect the ion beam sufficiently. Therefore, the design of the condenser is a compromise between maintaining plate separation while avoiding large electric potentials.

From equation 3.15, it can be seen that the deflection is proportional to the electric field applied. Thus, from $E = \Delta V/d$, the deflection simulation in figure 3.4, and assuming a plate separation twice the specification beam deflection range of $\pm$30 mm, the required range of the deflection plates' electric potentials is estimated to be $\pm$ 550 V.

3.5 Ion Beam Neutralisation

In this section, the neutralisation chamber design parameters are first discussed separately, with each of the parameters and their relationship with system performance explored. This is done as some aspects of the design have competing effects on system performance. The proposed design of the neutralisation chamber will then be described after the various design considerations have been explained. As mentioned in section 3.1.1, the chosen method of ion beam neutralisation is photo-detachment. In photo-detachment, the negative hydrogen ions are irradiated with photons of sufficient energy, producing neutral hydrogen atoms in the reaction:

$$H^- + \gamma = H + e^- \tag{3.17}$$

This is the process by which the negative ion beam is used to create an accelerated neutral beam. As mentioned briefly in section 3.1.1, further ionisation of the produced atoms can be prevented by careful selection of the photon energies. With photon energies less than the binding energy of the H atoms' remaining electrons, the electrons will not be stripped from the atoms to form positive ions. At the scale of beam-beam interaction, an approximate relation for the fraction of beam ions neutralised has been formulated:

$$f = 1 - e^{-\sigma(E)Ft} \tag{3.18}$$

where $\sigma(E)$ is the energy dependent cross-section, F the photon flux and t the time the ions are in laser light[34].

The main purpose of the neutral beam gun is to generate accelerated neutral particles. To this end, it needs to maximise the fraction of neutralisation of the ion beam. From equation 3.18, it is evident that to achieve this, the cross section of the reaction, ion irradiation time and photon flux must be maximised. However, in the subsequent sections, it is shown that these parameters are limited by various constraints and so in section 3.5.6, a target efficiency of 50 % was set.

3.5.1 Maximising Cross Section of the Reaction

The cross-section of the reaction described by equation 3.17 is dependent on the energy of the photons used. The relationship between the photo-detachment cross section and photon energy has been confirmed experimentally by various groups, showing that the cross-section is maximised at a photon energy of about 1.5 eV [35][36][37]. This corresponds to a cross section of about 4.0×10^{-17} cm^2. Hence, to maximise the cross section,

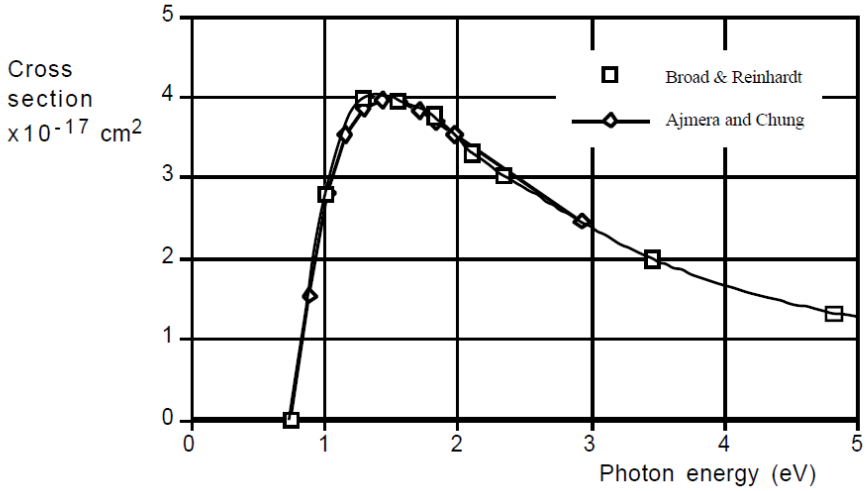


Figure 3.6: Plot showing experimental data of photo-detachment cross-section against photon energy [35]

the laser wavelength has to be chosen to match this energy. The matching wavelength can be calculated as follows:

$$\lambda = \frac{hc}{E} \tag{3.19}$$

where h is Planck's constant, c the speed of light and E the photon energy. This equation gives a wavelength of 827 nm, which is in the near-infrared range. This is an important parameter with which to select a laser source. Other pertinent considerations include the laser beam-shape and the divergence of the laser source.

3.5.2 Maximising Irradiation Time

To maximise the time the ions have to undergo photo-detachment, the length through which the ions travel in laser light has to be increased. This can be achieved by increasing the ion-direction number of the laser sources used. However, the environment the overall system is working in is limited by space. Furthermore, for a fixed laser intensity, increasing the area of laser illumination will also increase the input power requirement of the system. One detail to note is that the number of photons involved is far larger than the number of ions within the ion beam. As such, the laser beam is relatively unchanged by passing through the ion beam. Thus, the total energy required to neutralise the ion beam can be reduced by using mirrors to pass the same laser beam through the ion beam multiple times, increasing the path of the ion beam irradiated by each laser source.

However, no mirror has perfect reflectance, and this results in intensity loss with each consecutive laser beam reflection. After a number of reflections, the laser beam will have

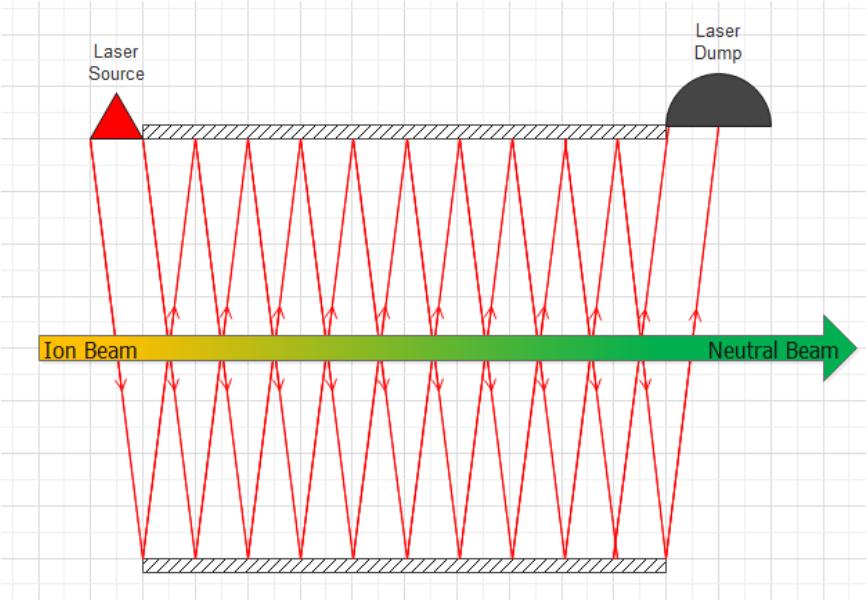


Figure 3.7: 2-Dimensional abstraction of laser beam path as it reflects in the chamber, relative to the ion beam

too low an intensity to achieve the desired neutralisation fraction. At this stage, a new laser source can be added increase laser intensity back to the required levels. The number of reflections allowed is determined in section 3.5.6.3 by considering the laser source and mirror quality.

3.5.2.1 Mirror Design Considerations

In this application, two main criteria govern the choice of mirrors. The first is reflectance, the percentage of incident radiation that is reflected. A high reflectance will allow the beam to reflect more times before the laser intensity falls too low for use. The second criteria is the Laser Induced Damage Threshold(LIDT), the maximum incident laser intensity before mirror damage occurs. This limits the power of the lasers that can be used. For most mirrors, the reflectance is dependent on the wavelength of incident light while the damage threshold is dependent on both the wavelength and the laser mode, that is if the laser is continuous wave or pulsed. As the ion beam needs to be constantly neutralised as it is scanned across the hadron beam, the continuous wave mode is more applicable. With an initial laser intensity of I_0 and reflectance R, the resultant laser beam intensity after N reflections, I_N is given by:

$$I_N = I_0 R^N \tag{3.20}$$

3.5.3 Maximising Photon Flux

In the previous subsection, it was stated that mirrors have a limited tolerance for laser intensity incident on it. Thus, the choice of mirrors used provides an upper limit of laser intensity that is suitable. A similar limitation is present for laser sources, with the difficulty of fabricating laser sources increasing with their power. Should the photon flux required for the designed neutralisation fraction be above these limits, the effective photon flux neutralising the ion beam can be increased by crossing the ion beam with multiple lasers from different angles. Each of these lasers will have its own source and mirror system, thus circumventing the individual intensity limits.

3.5.4 Neutralisation Variation While Scanning

3.5.4.1 Beam Geometry

To prevent laser light from being reflected back into its source and damaging it, the incident angle of the laser must be non-zero. For the laser source to illuminate multiple beam widths worth of the ion beam path, it should be angled in the direction of ion beam path. This angle, however, causes the length along which the ion beam is irradiated to depend on its transverse position. Furthermore, there is a variation in the laser intensity along the beam path depending on its transverse position due to how the laser beams intersect. This is best visualised in the 2-dimensional representation in figure 3.8. This variation on beam path intensity and length can be analytically determined and accounted for, either by normalisation in the reconstruction process or beam current variation to ensure constant hydrogen atom output. As the neutralisation fraction as described by equation 3.18 depends on the photon flux-time product, it is also dependent on the photon flux-beam path length product. From the diagram above, by simple geometry the angle in question and relationship between the transverse deflection and the photon flux-path length product is given by:

$$\theta = tan^{-1}(\text{beam width/chamber diameter}) \tag{3.21}$$

$$\text{path-intensity product} = \frac{I_0 * L}{r}((2N+2)r - N\Delta h) \tag{3.22}$$

At the small angle of the laser, the variation the neutralisation due to beam geometry may be much smaller than other sources of output beam noise. Should this be found to be the case in experiment, no further measures will need to be taken to correct it.

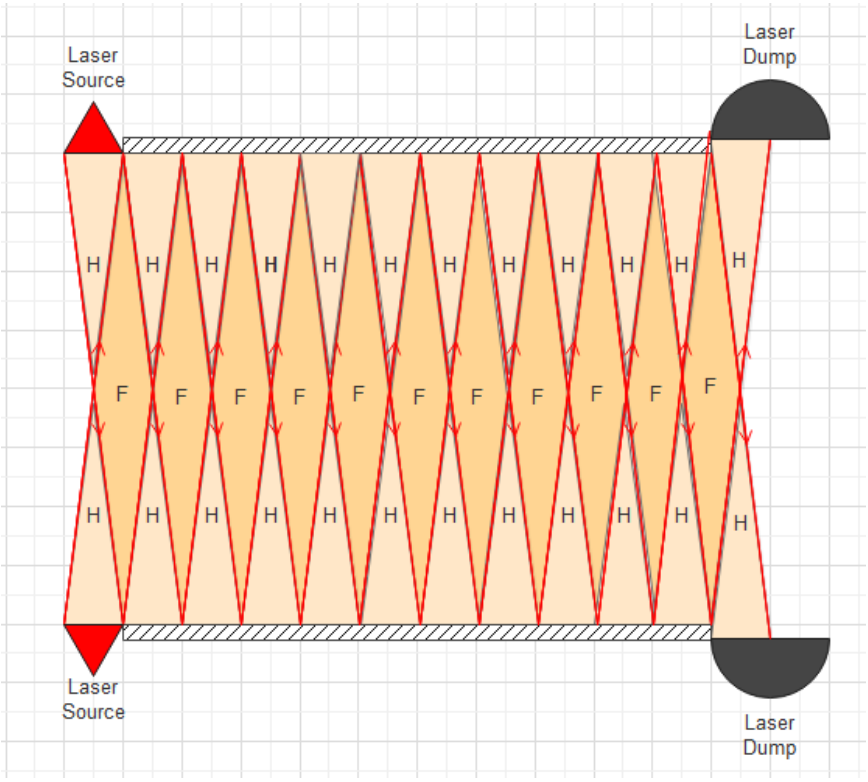


Figure 3.8: Diagram to illustrate variation of intersecting laser intensity, where H represents half design intensity and F full design intensity *(note laser angles are exaggerated to illustrate the concept)*

3.5.4.2 Laser Interference

As lasers of the same wavelength are coherent light, they can interfere to give minima and maxima. The proposed design involves crossing the ion beam with multiple laser beams which can interfere to form an interference pattern. The maxima spacing is dependent on the number of laser beams crossing each other and the angle between them. For two intersecting laser beams, the maxima spacing, d is given by the equation [38]:

$$d = \frac{\lambda}{\sin(\theta)} \tag{3.23}$$

where θ is the angle between the two laser beams.

From the above equation, it can be seen that orthogonally directed laser beams give the smallest maxima spacing while parallel or anti-parallel beams give the largest maxima spacing. For a finite ion beam-width scanning across the interference pattern of a laser, the effective laser intensity incident on the ion beam will vary as the ion beam scans across maxima and minima. It can be reasoned that the largest variation in total intensity is one maxima's worth of radiation.

Consider a interference pattern with maxima spacing d, and an ion beam width of 2.5 d travelling in the x-direction. At maximum, the ion beam can intersect 3 maxima, and 2 minima. However, as it deviates from this position, its intersection with the maxima at one end will decrease, with a corresponding increased intersection with a minima at the opposite end. It will then reach a state where the ion beam intersects with 2 maxima and 3 minima.

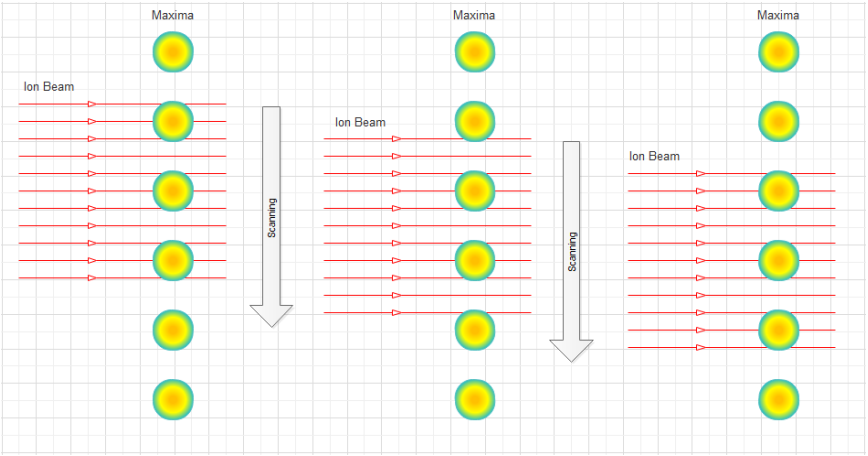
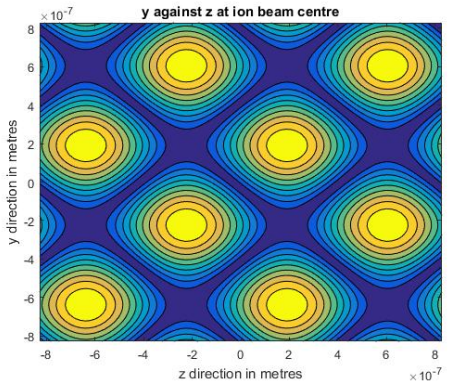


Figure 3.9: Variation of intersecting laser intensity as ion beam is scanned

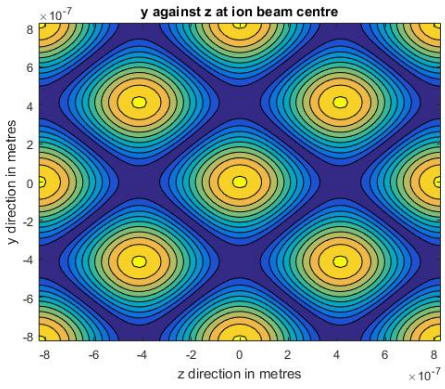
The minima do not contribute to the effective neutralising irradiation on the beam and so the effective neutralising radiation has been reduced by one maxima intensity's worth. Further ion beam deflection will then return the beam-laser intersection to its maximum state. Thus, the greatest variation in photon flux incident on the ion beam due to beam scanning is one maxima's worth. To reduce the fractional variance of the photon flux incident on the ion beam, the number of maxima intersected by one beam width should be maximised. As the beam width is set by the project specifications and the wavelength of the laser is determined by the maximum cross-section, the remaining way to decrease the maxima spacing is by maximising the angle of intersection according to equation 3.23.

A program was written in MATLAB to simulate multiple lasers interfering in a 3-dimensional space, centred around the centre of the ion beam. From the 3-dimensional interference space, sections of the three principle planes are then extracted to show the interference pattern. Figure 3.10 shows the interference patterns in the transverse plane(perpendicular to ion beam) for various laser arrangements. Note the result that increasing the number of non-orthogonal lasers intersecting increases the maxima separation.



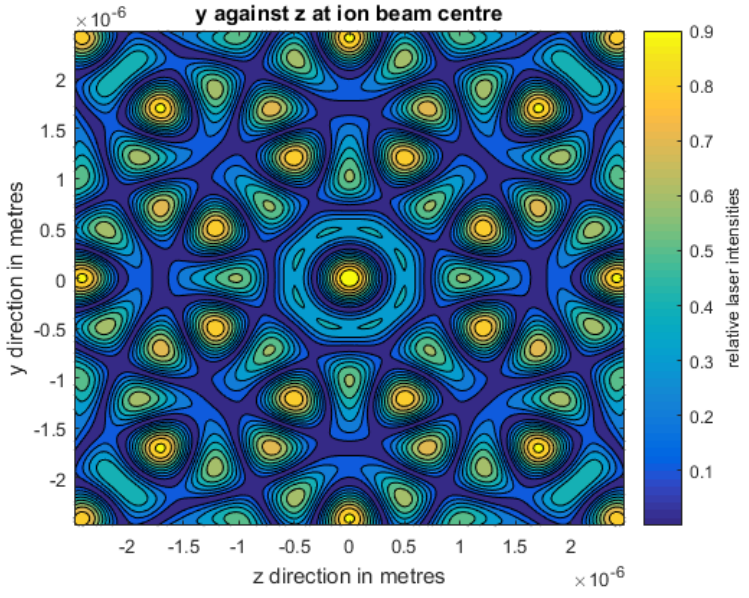
a

(a) 2 Orthogonal Lasers



b

(b) 4 Orthogonal Lasers



c

(c) 8 Orthogonal Lasers (note larger scale to show maxima distance)

Figure 3.10: Transverse plane interference patterns for various number of lasers

The above analysis assumes that interferences occurs but this is not necessarily so. The Fresnel-Arago Laws state that two orthogonal, coherent linearly polarised waves cannot interfere[39]. Hence, we can prevent two laser beams from interfering with each other by using orthogonally polarised lasers. However, there are only two linearly orthogonal polarisations available, and so this method can only be used to remove the interference between two lasers. If a third laser is added, it will have to interfere with at least one of the existing sources.

In spite of this, the method can be used to reduce the unwanted effect of interference by minimising maxima spacing. As previously mentioned, multiple laser beams will be used to cross the ion beam. By dividing the lasers between two linear orthogonal polarisations, the number of interfering lasers in the pattern is effectively halved; the resultant interference

patterns from the two polarisations are just superposed. Furthermore, from equation 3.23 it can be seen that anti-parallel light will interfere to create the largest maxima spacing. Thus the maxima spacing is minimised by setting opposite laser sources at orthogonal polarisations.

3.5.5 Other Practical Considerations

This section briefly explores other considerations in designing the system.

3.5.5.1 Incomplete Neutralisation of the Beam

As not all of the ions will be neutralised within the chamber, an ion dump at the end of the neutralisation chamber is required. This same ion dump will also have to remove the electrons stripped from the ions in the neutralisation process. This can be achieved with a electrostatic beam dump. With the relatively low energy of the system's ion beam after neutralisation, a metal target such as a plate of tungsten and an electrostatic deflector to direct the beam into the target would suffice.

3.5.5.2 Laser Induced Damage of Components

Another important consideration to note is that laser light at the required intensities form very high energy beams that can damage equipment. In particular, the laser beams from one source can destroy other laser sources should they be incident on them. In the proposed system, once the reflected lasers' intensities become too low due to multiple reflections, a new laser source is used to provide a new laser beam of equal intensity. However, if the laser beam from the previous source is incident the new source, the new source will be damaged. Hence, it is necessary to dump a degraded laser beam before starting a new one. Most laser dumps for the mid-energy range consists of a cavity leading to a cone shaped depression in an anodised aluminium block to absorb the laser energy and dissipate the resultant heat.

3.5.5.3 Magnetic Field of the Environment

From the analysis shown in figure 2.20 in chapter 2, the entire accelerated neutral atom gun will reside in a moderate magnetic field of 0.07 T. This magnetic field will influence the trajectory of the H^- ions within the neutral beam generation system prior to neutralisation. Thus it is important to magnetically shield the probe beam path from the ion source to the exit of the neutralisation chamber. Fortunately, the cylindrical shape of the system is compatible with many magnetic shields available. For the accelerated neutral atom gun, a

customised Magnetic Shield Corp. MuMETAL® Zero Gauss Chamber[40] will be applicable.

3.5.6 Neutralisation Chamber Design Process

With the design parameters and criteria discussed in the previous sections, this section explains the final design choices for the neutralisation chamber.

Initially, an ambitious 99% neutralisation fraction was considered. Using equation 3.18 and the maximum cross-section of photo-detachment of 4.0×10^{-17} cm^2, the photon flux-irradiation time product was found to be $Ft = 1.19 \times 10^{17}$ cm^{-2}. The irradiation time,t is determined by both the ion energy and the length of the neutralisation chamber. Due to the space limitation on location at the Large Hadron Collider(LHC), the neutralisation chamber length is set at 0.5m. The beam energy has also been specified to be 500 eV in section 2.3.1 to optimise probe-hadron interactions. These correspond to a irradiation time of 1.6×10^{-6} s. With that, the photon flux,F was found to be 7.3×10^{22} photons cm^{-2} s^{-1}, giving a laser intensity of $I = 17.7$ kWcm^{-2}. This laser intensity far too high to be feasible.

Examining equation 3.18, it is evident that increasing the photon flux has an asymptotic approach to a 100% neutralisation fraction. Hence, decreasing the neutralisation fraction will have a more than proportional decrease in the photon flux required. Therefore, a more modest 50% neutralisation fraction was chosen as a design guideline. This translates to a photon flux of $F = 1.11 \times 10^{22}$ photons cm^{-2} s^{-1} and a laser intensity of 2.67 kWcm^{-2}. This laser intensity is more feasible and the following analysis is based on this laser intensity.

3.5.6.1 Mirror Choice

Many commercial manufacturers produce laser-dedicated mirrors tuned to various wavelengths. These commercially available mirrors were assessed based on their reflectance and damage threshold. Of the various mirrors examined, the most suitable mirrors were found to be Thorlabs' broadband dielectric mirror with E03 coating. This mirror has a high reflectance of 99% for the required wavelength range [41]. Although their website had no information on the Laser Induced Damage Threshold(LIDT) for continuous wave lasers, Thorlabs' indicated in an email that an incident laser intensity of 1000 Wcm^{-2} would not damage the mirror. Hence the dielectric mirror is ideal for reflecting the laser beams in the neutralisation chamber.

3.5.6.2 Laser Source Specification

While many laser systems are available commercially, at the specification wavelength of 827nm and intensity in the order of 1.0 kWcm^{-2}, none of the readily available lasers are suitable. The closest to specification is a laser diode stack by Cutting Edge Optronics that a choice of wavelengths from 790 nm to 1550 nm and a quasi continuous wave power of 900 W[42]. However, this source has an unsuitably large divergence of 7 degrees. As none of the commercial laser sources are suitable, a tailor-made laser system will need to be commissioned, possibly using diode pumped fibre lasers to achieve the required high intensity and small divergence. Any further analysis assumes a common beam thickness of 5 mm and that the laser source will be made to specification.

3.5.6.3 Laser Source Arrangement

Earlier in the report it was established that maxima spacings were to be minimised that increasing the number of interfering lasers would increase this spacing. It was also established that by using orthogonally polarised lasers, the number of interfering lasers can be reduced to the number of orthogonally polarised pairs. With this in mind, the minimum number of laser pairs to meet the required intensity of 2.67 kWcm^{-2} is 2, that is 4 laser sources. These laser sources will be placed 90^o to each other around the neutralisation chamber's transverse plane, with opposite laser sources orthogonally polarised. This results in a maxima spacing of one wavelength, 827 nm as calculated from equation 3.23 and shown in figure 3.10a. This is less than 0.05 % of the ion beam width and hence the neutralisation variation due to interference is less than 0.05 % of the atom beam flux.

In order to create a continuous irradiated path for the ion beam to travel through, every laser source should share the same angle to their chamber walls so as to ensure that all laser beams travelling in the same direction are parallel. There should also be no gaps between parallel laser beams. Thus the tilt angle of the laser sources is such that as one beam reaches the opposite side of the chamber, it will also have travelled a length of one beam thickness in the direction of the ion beam. Here beam thickness is the laser beam thickness in the direction of ion beam. Thus the laser beam just misses the laser source opposite to its own, then reflecting off mirror. This can be seen in figure 3.8. This beam angle is found to be:

$$\theta = tan^{-1}\left(\frac{\text{beam thickness}}{\text{chamber diameter}}\right) \tag{3.24}$$

To ensure that the laser intensity never degrades below the design value before dumping, the required initial laser source intensity is found by rearranging equation 3.20. For one

Outer Diameter	0.5 m
Length of Neutralisation Chamber Cavity	0.5 m
Cross-section of Neutralisation Chamber Cavity	0.2 m $\times$ 0.2 m
End Plate Thickness	0.025 m
Number of Laser-Mirror Stages	2
Number of Lasers per Stage	4
Length of Stage	0.215 m
Laser Source Intensity	1000 Wcm^{-2}
Mirror Dimensions	0.2 m $\times$ 0.2 m

Table 3.3: Neutralisation Chamber Parameters

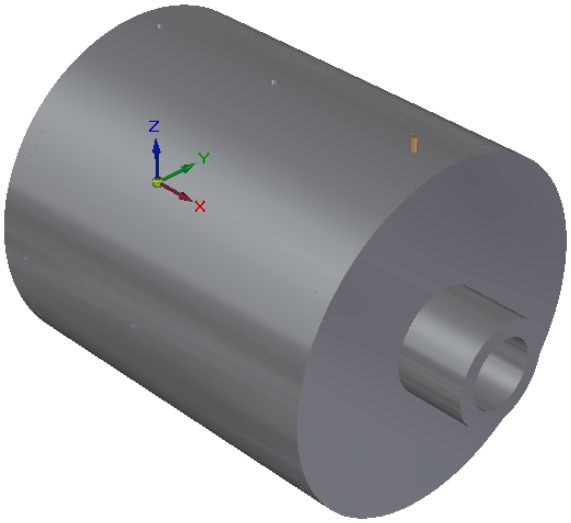
set of lasers to be reflected through the the whole length of the neutralisation chamber, corresponding to 99 reflections, the required initial total intensity is 7.4 kWcm^{-2}. This would require 8 laser beams instead of 4 to stay within the mirror LIDT, resulting in larger maxima spacing that is undesirable. Instead, it would be more feasible use a more moderate initial intensity and start with a new set of laser sources once the laser intensity becomes too low.

To determine the maximum number of laser reflections that can be used for a 4 laser beam system, let each initial laser intensities be at the mirror LIDT of 1.0 kWcm^{-2}. Thus the initial total intensity is 4.0 kWcm^{-2}. From equation 3.20, the maximum number of reflections, given a initial intensity of 4.0 kWcm^{-2}, is 40. With the lasers travelling 5 mm in the beam direction for each reflection, the laser beams will need to be dumped every 205 mm. Noting that some space is needed for the ion beam dump within the neutralisation chamber, the system can be split into two stages of laser and mirrors followed by an ion dump.

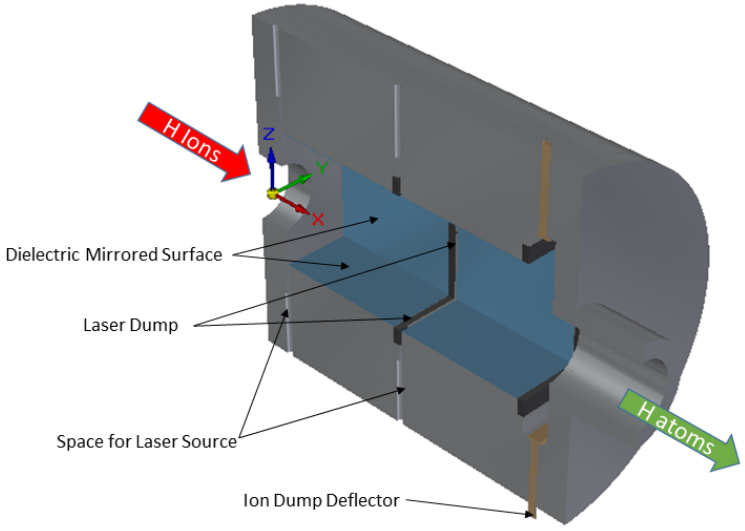
3.5.6.4 Neutralisation Chamber Model

From the above analysis, and noting the spatial constraints of system, the parameters of the neutralisation chamber are:

To get a better idea of what the overall neutralisation chamber would look like, a Solid Edge CAD model was made. This is shown in figure 3.11. As the closed surface of the external view does not show most of the salient features, a second figure showing the section view is included.



(a) External View



(b) Section View

Figure 3.11: CAD Model of Neutralisation Chamber

3.6 Overall Architecture

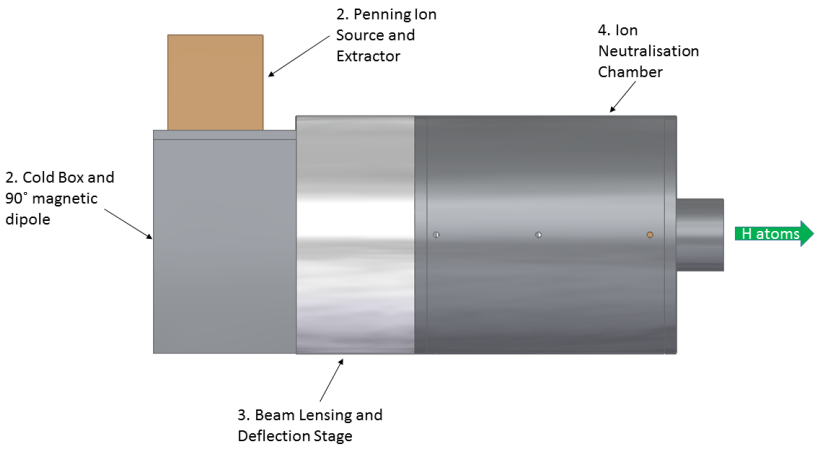


Figure 3.12: Overall Beam Line Architecture

The above figure shows the main beam-line components of the overall system. Referring to the diagram above, a brief summary of the accelerated neutral atom generation process is as follows:

1. Negative hydrogen ions are generated in a penning ion source and extracted at 500 V.
2. The extracted ion beam is passed through a 90^o magnetic dipole and cold box to remove electrons and caesium atoms respectively
3. The cleaned ion beam is then focused to achieve the desired beam shape and deflected to achieve the desired beam position.
4. The negative ion beam is neutralised *via* photo-detachment to form a neutral hydrogen atom beam which retains its previous beam shape and particle energy.

Chapter 4

Hollow Electron Beam Imaging

The atomic hydrogen beam is detected after being scanned across the charged particle beams to image the hollow electron beam. The neutral atoms are counted at the detector and compared with the original atomic beam flux to give the density profile of the hollow electron beam in one direction. The signal based on the interaction of H atoms with protons is much lower than that of H atoms with electrons. It is assumed here that the signal from the proton beam is negligible in the detection of neutral particles.

There are two neutral particle detectors to obtain orthogonal 1D projections. Methods to reconstruct the 2D profile and to extract useful parameters will be discussed.

4.1 Neutral Particle Detector

A micro-channel plate (MCP) detector is chosen for neutral atom detection. Two other types of detection method considered in the project are also presented below, namely, the semiconductor detector and the neutral particle detector (NPD).

4.1.1 Semiconductor Detector for Atomic Hydrogen

The semiconductor detector to be described in this section is sensitive to atomic hydrogen whilst insensitive to molecular hydrogen. The major contribution to the detection signal is assumed to be the change in conductivity of the semiconductor when atomic hydrogen becomes chemisorbed to the detector surface and generates heat during the chemical process.[43] Chemisorption is a phenomenon in which the atomic hydrogen becomes chemically bound to the oxide surface when in physical contact. The semiconductor acts as a thermistor, and information is obtained through measuring its temperature-dependent resistance. A Wheatstone resistance bridge, along with a phase-sensitive amplifier, is proposed for monitoring the varying resistance. The detection system is shown schematically in Figure 4.1

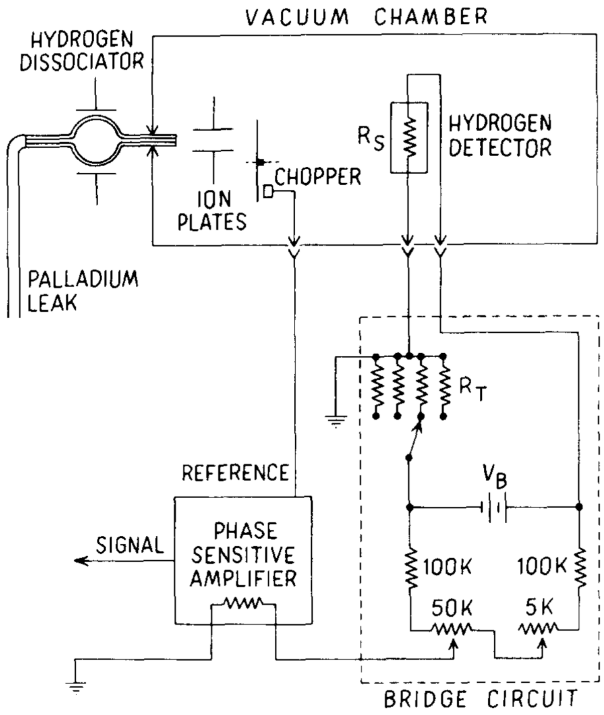


Figure 4.1: Semiconductor Detector System[43]

The resistors in the resistance bridge are of 1% precision. The semiconductor material used in this case is a sintered combination of nickel oxide, manganese oxide, and cobalt oxide, which is commercially available. Sintering is the process of compacting and forming a solid mass of material by heat and/or pressure without melting it to the point of liquefaction.

The detector response is susceptible to various sources other than the incident atomic beam which affects the conductivity of the material. For instance, sources that affect the temperature of the detector, or those that induce photo-electrons. Therefore, isolation of the detector is required. The detector is placed in an aluminium block which acts as a heat sink.

The response of the semiconductor material to ranges of atomic hydrogen flux is not well-documented, hence careful calibration is necessary to obtain accurate results on the beam flux. Linearity of the detector response is not guaranteed. An accumulation layer with higher electron density than the detector is formed, thus increasing the conductivity. Kinetic energy of the hydrogen atoms which impinge on the semiconductor surface, recombination of the atoms into hydrogen molecules when the atoms stay long enough on the surface may also change the conductivity of the detector to some extent.

More importantly, the semiconductor detector may not meet the need of a real time imaging system. Spatial resolution is not discussed in the source. It is only stated that the detector is moving on a sliding rail, so the assumption that it should move synchronously

with the scanning atomic hydrogen beam in our system should be made. System response time is slightly faster than 2ms. This means that by using a H beam source of 1mm spot size, signals from neighboring positions are not separable if the beam source is scanning faster than the response time. Even though the sintered semiconductor material used in this system is less likely to saturate than pure crystals, it is still possible for the detection surface to saturate due to high intensities of the atomic hydrogen beam. Once saturated, the semiconductor will have to be baked before replacement, which is certainly undesirable for a real time measurement.

4.1.2 Neutral Particle Imager (NPI)

The neutral particle imager (NPI) has also been considered as a choice to detect neutral atoms since it's being widely used in spacecrafts for energetic neutral atom (ENA) detection. This system is much more well developed in its use for neutral particle detection than the previous semiconductor detector. The system is based on indirect detection of neutral particles through converting the charge state of atoms before detecting them.

For energetic neutral particles of energy <600 eV, thin foils such as carbon or silicon foils ionise the atoms during foil passage. The penetration of the foil results in change of initial charge states and secondary electron emission. The ions formed are then collected by a system which is a combination of an ultra-thin foil with position sensitive micro-channel plates.[44] Small atomic number of the material reduces scattering and energy loss of the atoms. However, this works better for hydrogen atoms with energy >0.9 keV because of the fact that the ionisation efficiency reduces significantly as particle energy decreases. Figure 4.2 shows such trend for H and O.

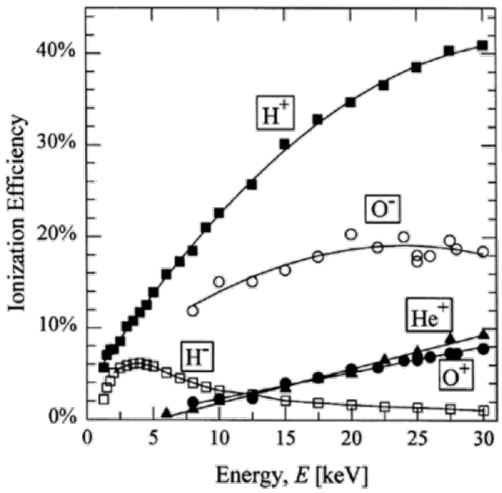


Figure 4.2: Ionisation Efficiency for Atoms as a Function of Energy [44]

In addition, spatial information is most likely lost as the hydrogen beam passes through the foil since scattering might happen.

For less energetic particles, there isn't sufficient energy for foil passage. Consequently the ionisation is based on surface interaction with conversion surfaces. An alternative approach might be to use a high frequency shutter that ideally doesn't have energy constraints. The high-frequency shutter is shown schematically in Figure 4.3

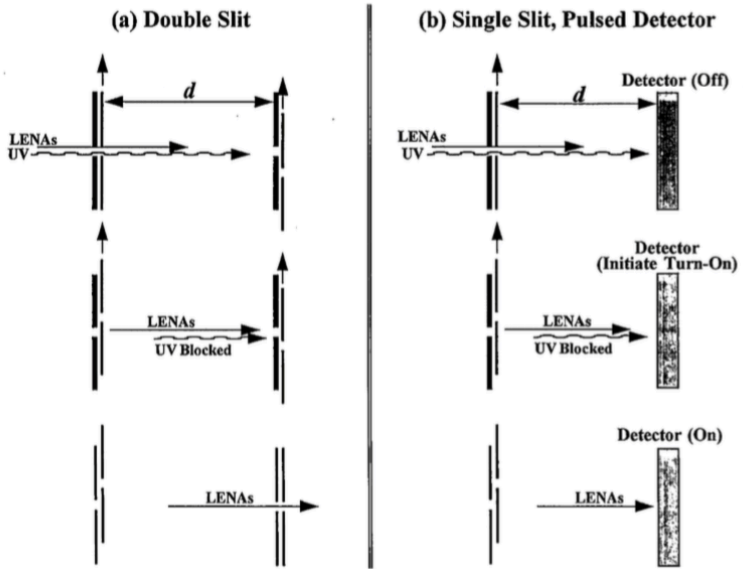


Figure 4.3: Schematic Views of High Frequency Shutter [44]

Each shutter contains a set of plates, of which one is fixed and the other is movable at high frequency. For one high-frequency shutter system, there are two shutters being out of phase, in order to let the neutral particles enter the detection region. This scheme is very useful in rejection of undesirable particles other than the useful signal. However, the high frequency shutter senses single neutral particles as they pass through the shutter, which might result in poor detection of intensive neutral particle beams.

4.1.2.1 Surface Interaction

In this section, the surface interaction process is discussed. One such interaction process is by means of neutral atom reflection on a reflection surface. According to NASA, one of the cameras for PIPPI (Prelude in Planetary Particle Imaging) neutral particle imager in the Astrid-1 mission is a MCP camera.[45] The technique can be described as: incoming neutral atoms cause charged secondary particles to be emitted from a graphite target; the secondaries are then detected by a micro channel plate (MCP). The specifications for this

MCP are: detection energy range 0.1-70 keV; 16kbps bit rate. This detection concept is shown in Figure 4.4 .

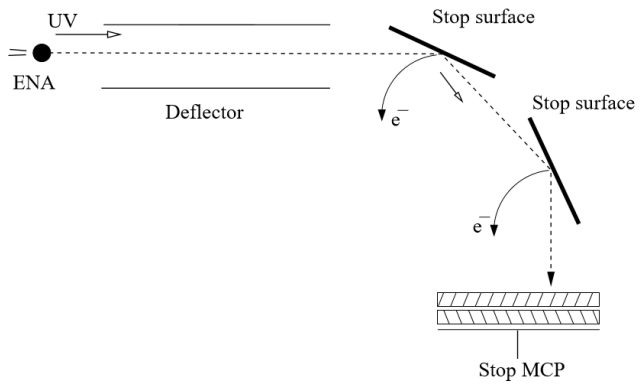


Figure 4.4: Detection by Reflection Surface [44]

The incident atomic hydrogen beam strikes the first reflection surface at an angle <30°. The exciting particles could be negatively charged, positively charged or neutral. After another reflection, the particles reach the micro-channel plate detector (MCP). Negatively charged particles are repelled by the negative potential applied at the front surface of the MCP. A V-stack or Chevron stack of two MCPs at a certain angle is used to reduce ion feedback.

The reflection surface reflects the incident atomic beam as mirrors reflect light. The difference between these two schemes is that the charge state of the atoms might change due to interaction with the surface. LiF or graphite can be used as the reflection surface. The advantage of LiF is that it's transparent to UV photons. An MCP is also sensitive to UV radiation, thus the use of LiF eliminates this possible source of noise.

Another way to implement surface interaction is based on secondary electron emission.

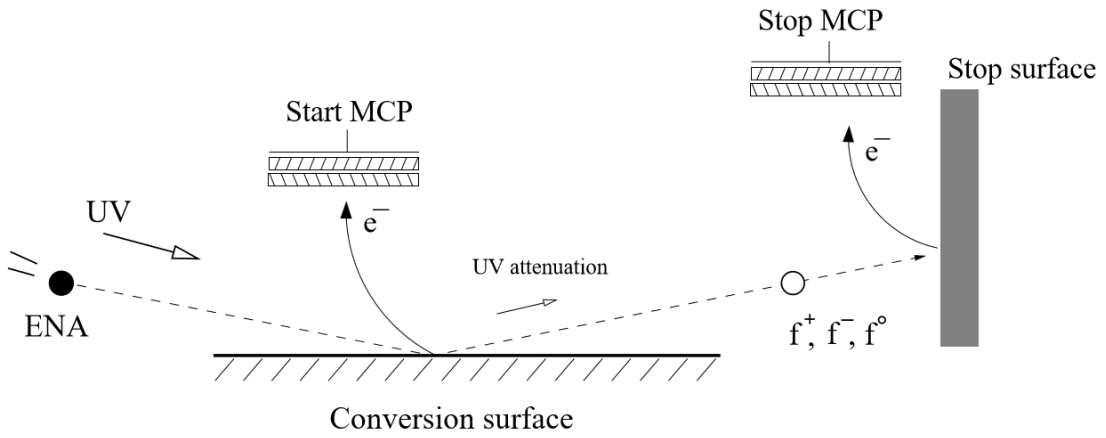


Figure 4.5: Concept of Detection based on Secondary Electron Emission [44]

This detection method is utilized in the ASPERA-3/ASPERA-4 NPD sensors. The emitted secondary electrons are released from the conversion surface and are detected by the start/stop MCP's. This system has the advantage of high efficiency compared to the system based on the reflection surface, as no charge separation is required before striking the stop surface. On the other hand, two sets of MCP's for collection of start and stop signals seems unnecessary for obtaining 1D projections of the hollow electron beam. This is devised for a time-of-flight (TOF) analysis for the neutral particles in space.

Calibrations are required for both the NPI and NPD described above. Information on the characteristics of MCP to be used and efficiency of the whole system has to be obtained.

The mechanical design (produced by CAD software) for the NPI system modified from the design in [44] to meet the requirements of this project is presented in Figure 4.6 The NPI used in space missions for ENA detection is generally cylindrical in shape to give an angular resolution, which is unnecessary in the detection of atomic H beam in this project.

By simple geometric calculations, angles and as noted in the model should meet the constraint:

$$a + b = 45^\circ \tag{4.1}$$

where a = 15° and b=30° is set in the 3D model above. The material for the stop surface (reflection surface) is graphite coated by MgO, optimised for high secondary electron yield.

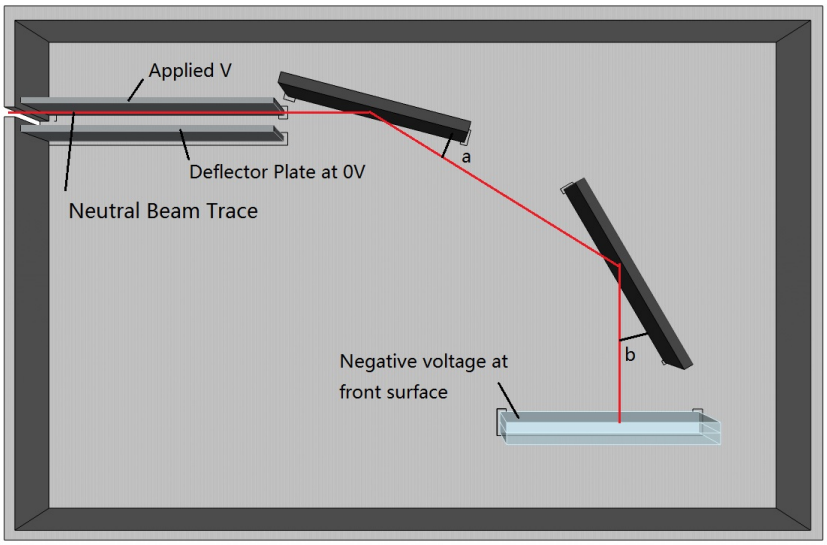


Figure 4.6: 3D CAD Model for NPI, Modified from the Model in [44]

Even though the NPI and NPD have been well developed, there is a disadvantage in creating secondary charged particles while the neutral detector is affected by the magnetic field in the collimator. The neutral detector is to be connected securely to an opening on the vacuum chamber. Charged particles created in the detection process would be affected by the electromagnetic field if no extra control is present and wouldn't follow the reflection path to the MCP detector. A possible solution is to model the path of the secondary charged particles under the effect of the magnetic field and redesign the positions of reflection surfaces and MCP. Potential problems are that: the reflection process could be altered in an undefined way; the reflection surfaces might have to be placed very close together which could lead to practical problems and would require a more accurate design; it is also possible to lose some charged particles which contribute to the signal, thus reducing the signal-to-noise ratio. Another proposed solution is to add magnetic shielding to the neutral detector. There should still be an opening for the neutral beam to enter the detection system. Consequently, a magnetic shielding combined with high-frequency shuttering at the entrance of the neutral beam might be a solution. If the shielding needs to be thick, then there could be practical issues with the high-frequency shutter. Moreover, the effect on reducing the magnetic field by the high-frequency-shutter would have to be decided.

Consequently, a simpler detection system, the MCP detector operating in the neutral mode, is proposed as the detection system to use for the detection of neutral beam deficit after scanning through the hollow electron shell.

4.1.3 Micro-Channel Plate (MCP) Neutral Detector

In general, the MCP detector is widely used in detection of charged particles.[46] The principle of MCP detection is based on secondary electron emission in micro-channels, caused by incident energetic particles. H atoms generated in the neutral atom generator are of 500eV energy, high enough to release secondary electrons. Consequently, the idea of atomic H beam detection by an MCP detector is explored further.

4.1.4 MCP Operation and Assembly

Each micro channel plate contains millions of glass capillaries, each with a diameter of a few microns, typically 4-25 μm. Each single channel functions similar to a multiplier. High voltage is applied across the MCP, to accelerate charged particles at the inlet across the channels. The incoming particle enters a channel obliquely and releases secondary electrons as it hits the channel wall. Repetitive secondary emissions leads to an avalanche process and achieves electron multiplication. Housing a huge number of multiplying channels within a compact area, an MCP provides a high spatial resolution. The pitch size determines the pixel size directly. Nevertheless, multiple charged particles entering the same channel would be indistinguishable at the exit. Hamamatsu[47] illustrates the principle for the MCP detector shown in Figure 4.7

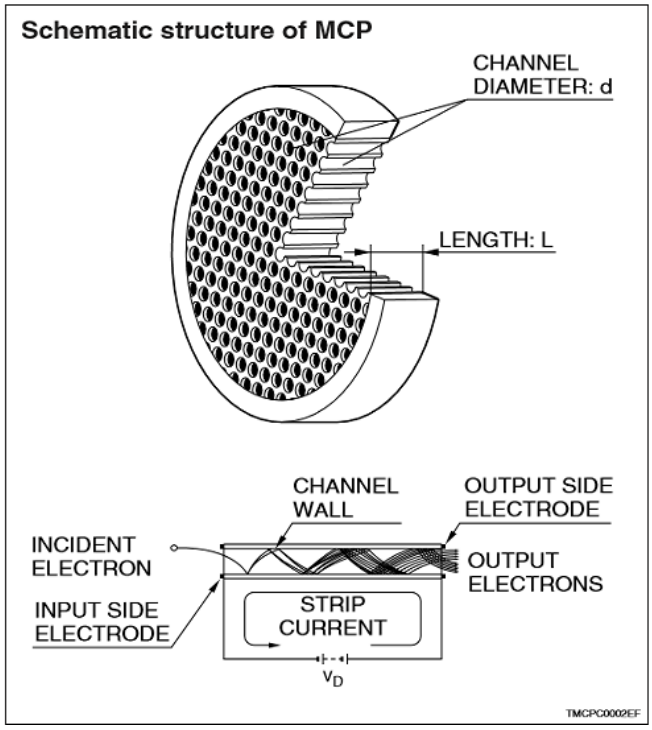


Figure 4.7: MCP Schematic Structure, Hamamatsu [47]

For photons as an input signal, a photocathode is placed before the MCP to convert the photons into electrons. The output electrons are collected by a phosphor screen to produce a visible image for the signal distribution. Alternatively, a multi-anode could be utilised to give the signal amount and position distribution. The latter choice gives much lower spatial resolution.

The magnitude of amplification is dependent on the voltage applied, the incident angle of a particle relative to the channel longitudinally, as well as the geometry of the micro-channels. Intuitively, higher voltage, greater inlet angle and longer channel, gives more amplification on the signal. One of the important geometrical factors for an MCP is the open-area-ratio, which will be discussed in the calibration section. When operating, an MCP is also sensitive to radiations such as UV light and X-rays. Every micro-channel takes time to recover before sensing another charged particle. This is the response time of the detector, typical value being a few hundred ps for both the rise time and fall time.

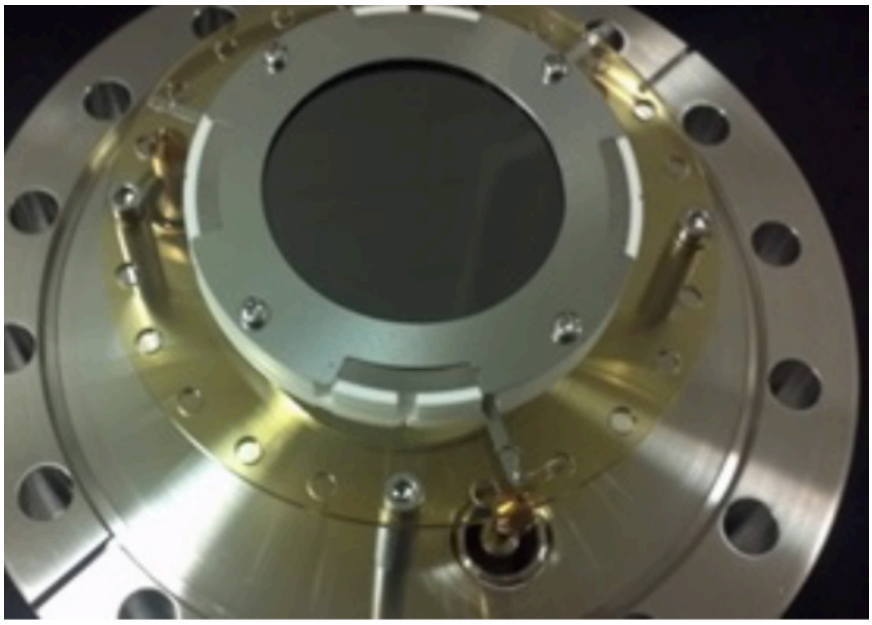


Figure 4.8: MCP CF Flange Assembly [48]

Multiple MCP's stacked together creates an even more multiplying effect. Another advantage of a double stack, also referred to as the Chevron stack, is in reducing ion feedback. Ion feedback is a major source of noise in the MCP, arising from adsorbed atoms on the channel surface being ionised as avalanche emission occurs. The ions released move towards the MCP front surface and induce more secondary electrons if no precautions are made. This not only reduces the signal-to-noise ratio but also possibly destroys the MCP through a permanent glow discharge. MCP's in a stack can be tilted at an angle to avoid such an effect and optimise performance. Another common configuration, the

Z-stack MCP, with 3 MCP's is also available. Stacks of MCPs are extremely useful in low-intensity signal detection. The downside of multi-MCP assembly is that pixel size increases as the multiplied electrons from the same channel enter a large number of micro-channels in the second stage.

Due to the fact that the neutral particle detection system is connected to the vacuum chamber, the MCP detector has to be ultra-high-vacuum (UHV) compatible. MCP's for use under UHV conditions are commercially available. MCP's mounted on a CF flange [48] to be used in vacuum systems is displayed in Figure 4.8

The additional advantage of this MCP detector is its low susceptibility to magnetic fields.

4.1.5 Delay-line layer

A three-layer delay-line readout technique has been developed for the MCP to enable detection of multiple hit events,i.e. large number of particles in a shower.[49] The anode is placed at the end surface of the MCP. As long as two particles don't arrive simultaneously at the same position, both temporal and spatial resolution information can be obtained. The limit is given by electronic dead-time and anode size.

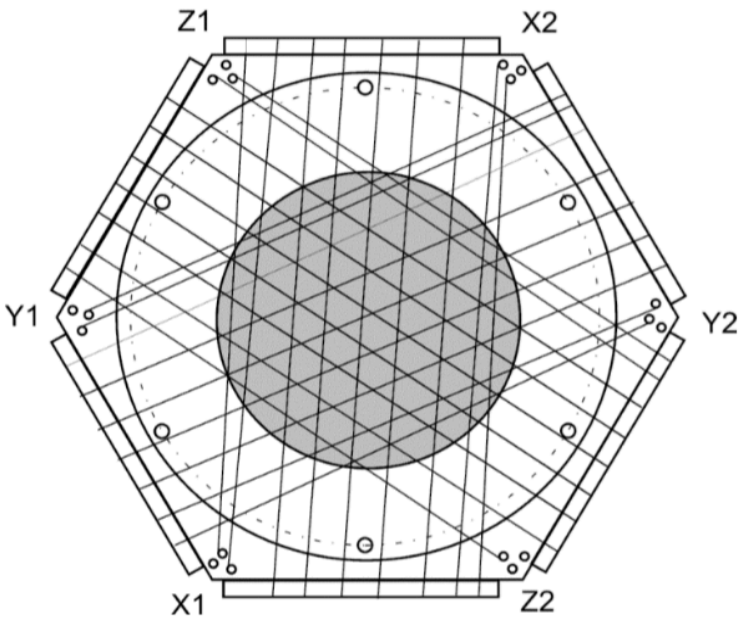


Figure 4.9: Schematic of the Hexanode [49]

Signals from any of the two layers give position information on the arriving particles, whilst the third layer resolves the issue of simultaneously arriving particles (different channels). Software can be used to process the resulting signal.

4.1.6 Mechanical Design

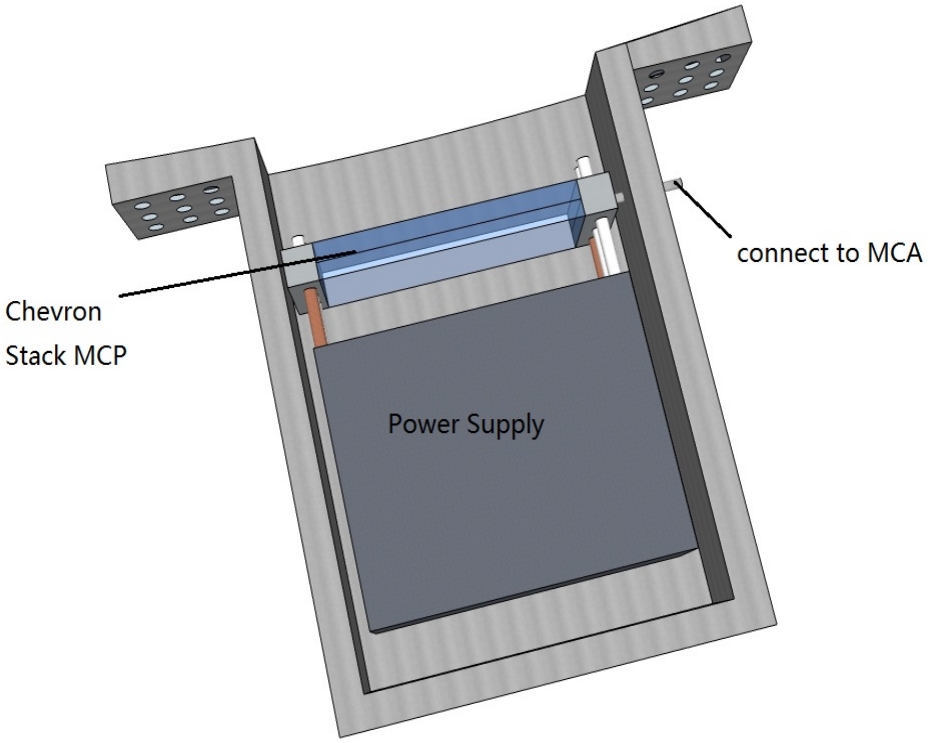


Figure 4.10: MCP Detection System
MCA refers to multi-channel analyser

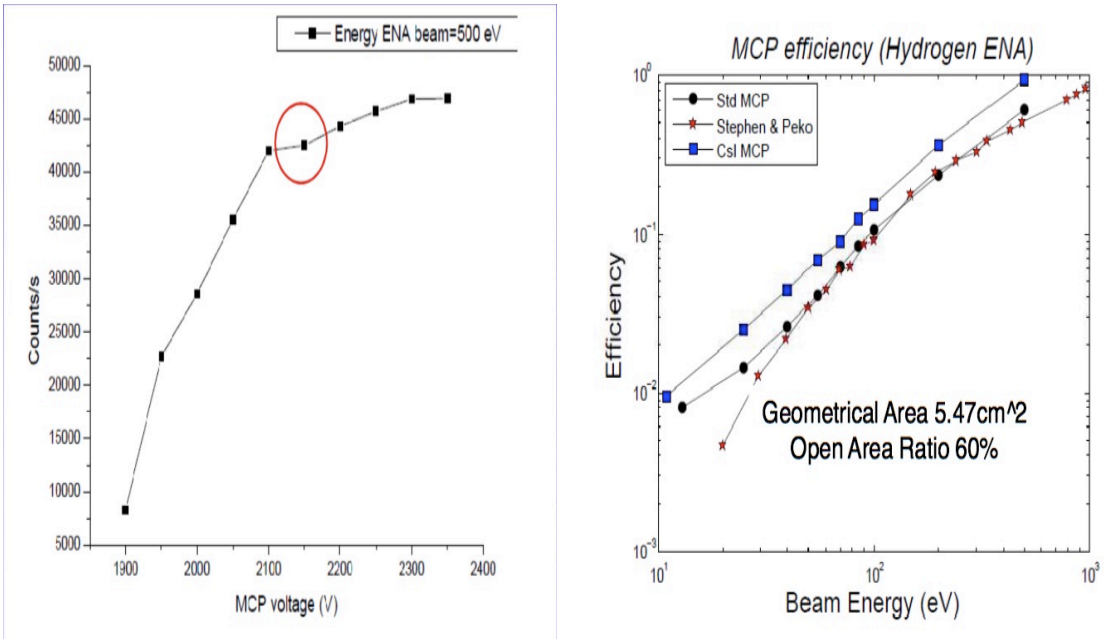
Figure 4.10 shows a model for the neutral particle detector produced using CAD software. The atomic hydrogen beam is incident on the MCP detector. The voltage output required for the power supply will be determined after the calibration of MCP operating voltage. For 0-1kV through 0-5kV, small size power supplies are commercially available. The output signal from the delay line layer is analysed by a position analyser, which is commercially available, to give position information on the output signals.

4.1.7 Calibration

4.1.7.1 MCP Characteristics

Calibration has to be done on the operating voltage and detection efficiency of the MCP detector.

The optimised operation voltage of the MCP is to be defined first. This is the voltage at which the count rate of the MCP saturates. Practically this is done by plotting the MCP count rate (given a preset beam intensity) against the voltage applied across its ends, as in Figure 4.11a. The operation point is marked as the voltage at which the gradient of the plotted curve begins to plateau. The following is an explanation of the saturating effect from [47]. The charge intensity at the end of the channel walls is very high due to the multiplication events. This is neutralised by strip current flowing through the walls. The strip current I_s is given by $I_s = V/R$, where V is the voltage across the MCP detector and R is the MCP resistance. I_s is typically of the order μA. Because of the fact that the strip current is very small, the detector gain decreases once output current reaches around 5% of the strip current. As for the operation voltage, it affects the output current significantly.



(a) Operation Voltage Calibration (b) Efficiency vs Beam Energy

Figure 4.11: Calibration Results of the neutral MCP Detector from [50]

After determining the operating voltage at a defined beam intensity, detection efficiency can be determined. Detection efficiency is determined by several factors, namely the geometry of the MCP used, and also the size and energy of the neutral atomic beam source.

One of the MCP geometrical characteristics that affects the detection efficiency is the open-area-ratio (OAR). The OAR is the ratio between the total open area to the total effective area of a micro-channel plate. It enables a preliminary evaluation of the detection efficiency, i.e. the proportion of inlet particles to the MCP front surface contributing to the final signal. For instance, particles that enter the space between micro-channels cannot be detected. Also as mentioned previously, particles entering the same channel are not distinguishable. Custom MCPs manufactured with glass wall channels can achieve 70% to 80% open-area-ratio. This 'input efficiency' is also dependent on the flux and size of the incident particle beam, given that the spacing between adjacent charged particles is comparable to the pitch of the MCP. Calibration can be done by focusing a neutral atomic beam onto the MCP detector within the expected flux range of the current system, and measure the proportion of particles detected by the MCP.

The MCP detection efficiency of neutral atoms is not as well documented as its detection efficiencies for electrons and ions. The reason for this lies in the difficulty of generating a well controlled low energy neutral atom source. Apart from the geometries of the incident beam and the detector, the energy of the low energy neutral atomic beam also affects the detection efficiency. Figure 4.13b shows the result for detection efficiencies against beam energy. [50] Calibration results differ for systems with different characteristics.

4.2 Reconstruction of the 2D Beam Profile

4.2.1 Challenges

Due to the fact that two hydrogen beam generators are incorporated in the imaging system design, only two orthogonal 1D projections are obtainable. This section demonstrates the difficulty in reconstructing an image from two projections. The reason behind using a simplified beam model will be discussed in Section 4.2.3.

Represent the reconstruction process by a system as linear equations:

$$\mathbf{Ax} = \mathbf{b} \tag{4.2}$$

where **A** represents the scanning process, **x** is the image and **b** represents the projections. For instance: given an image of size a $\times$ a pixels and 2 1D projections of size c$\times$1 each, the elements in the above linear system become:

$$\begin{aligned}
\mathbf{A} &= \begin{bmatrix} A_{1,1} & A_{1,2} & A_{1,3} & \cdots & A_{1,ad} \\ A_{2,1} & A_{2,2} & A_{2,3} & \cdots & A_{2,ad} \\ \cdots & & & & \\ A_{c,1} & A_{c,2} & A_{c,3} & \cdots & A_{c,ad} \\ \cdots & & & & \\ A_{2c,1} & A_{2c,2} & A_{2c,3} & \cdots & A_{2c,ad} \end{bmatrix} \\
\mathbf{b} &= \begin{bmatrix} P_{1,1} & P_{1,2} & \ldots & P_{1,c} & P_{2,1} & P_{2,2} & \ldots & P_{2,c} \end{bmatrix}^T \\
\mathbf{x} &= \begin{bmatrix} x_{1,1} & x_{1,2} & \ldots & x_{2,1} & x_{2,2} & \ldots & x_{a,b} \end{bmatrix}^T
\end{aligned} \tag{4.3}$$

For an image of a $\times$ d pixels and detector resolution of c $\times$ 1, a reconstruction without prior information becomes solving a $\times$ d unknown variables(pixel values) from only 2 $\times$ c equations. The above system could have a definite solution only if the original image is of 2$\times$2 or c$\gg$ a or d, while both are impractical. There are generally infinite solutions to such a system, which means an infinite number of possible images given the two projections.

Iterative methods are widely used in reconstruction from a limited number of projections. These methods can be summarised as a minimisation of cost functions, in which the exact form of the cost function may vary for different types of image. What's more, prior information must be obtained on the image to be reconstructed in order to limit the number of possible images given the projection data.

4.2.2 Explored methods of reconstruction

A preliminary model for the Gaussian electron shell is discrete particle-like. All the points with a value 1 represents the existence of 1 electron at the position and is plotted as white, while the background has a value 0.

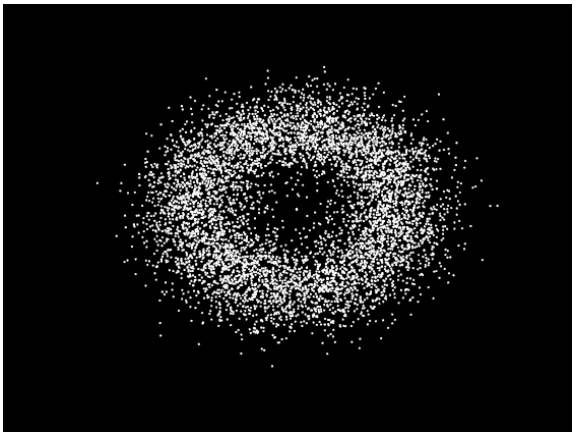
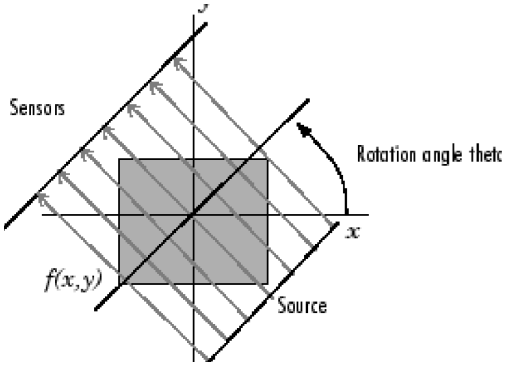


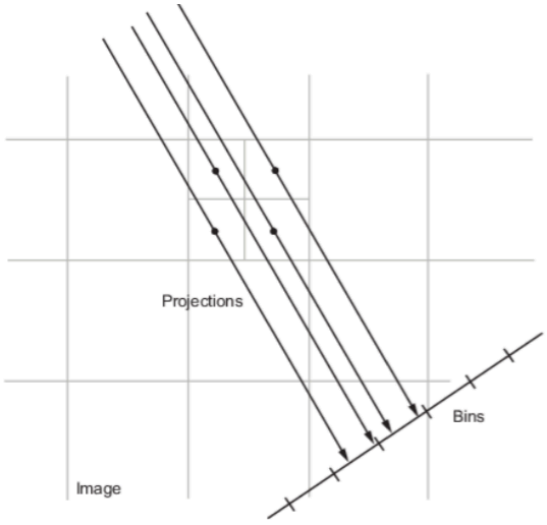
Figure 4.12: Discrete Gaussian Electron Shell Synthesised in MATLAB
resolution = 420×560, data type: uint8

4.2.2.1 Radon Transform and Inverse Radon Transform

The Radon Transform is defined as a series of line integrals through an image with offsets from the origin.



(a) Illustration of Radon Transform



(b) Radon Transform Implementation in MATLAB

Figure 4.13: Radon Transform from [51]

Both Radon transform and Inverse Radon Transform are built-in functions in MATLAB.

The Radon transform is an integral transform, in which each element of a 1D projection equals the line integral in this particular projection angle. As for the built-in MATLAB function 'radon', it is stated in the MATLAB help section that "the Radon transform of the image is

the sum of the Radon transform of individual pixels". What is done by default is that an individual pixel is divided into 4 subpixels and each subpixel contributes to the nearest two bins. For projections in the horizontal direction, for example, the overall number of bins in the projected data is greater than the number of rows of the original image. This certainly is not a good approximation of the real scanning process.

The Radon transform along with the inverse Radon transform produces no useful information from only a few projection angles. There are undesirable white bands where no particles are expected to exist in the reconstructed image.

4.2.2.2 Binary Image Reconstruction

The particle-like model for the Gaussian electron shell falls into the binary image category. One article [52] describes a min-cost-max-flow based algorithm. A binary image is reconstructed from two orthogonal projection angles using similar images to the unknown image as a priori information for the 2D image. Since the binary image to be reconstructed in the article is a vascular system, similar images used are images taken from the patient in previous instances, assuming that the patient's internal structure won't change much. The reconstruction algorithm is summarised as below.

- Compute cost matrix based on the set of similar images.
- Construct a network (weighted directed graph) using the projections data and cost matrix, define the cost and capacity of edges in the established network by elements from cost matrix and the projections.
- Compute min-cost max-flow for the network built in the previous step.
- Reconstruct image based on the rule that: an element in the unknown image is 1 if the corresponding flow in the network is 1.

The time complexity of this algorithm is *O($V^3\ log^2 V$)*, where V = m + n + 2, m is number of elements in row projection and n is the number of components in column projection.

The dependency of reconstruction quality on the set of similar images is also discussed in the article. The reconstructed image might be distorted if the a priori images are not close to the unknown image or if the number of similar images is very small.

On the other hand, the Gaussian hollow electron beam to be imaged may not have prior images from previous imaging instances. As a result, only synthesised images from the computer can form similar images. This requires prior information on approximate beam profile characteristics. Such information may be obtained from estimations based on the projection data with some efforts. However, for highly varying Gaussian distributions along

the beam cross section, estimations of good quality are difficult. Distortion in the reconstructed image will be possible.

A further problem with the application of min-cost max-flow on the reconstruction for the binary hollow electron beam profile is revealed by [53]. For N$\times$N digital images, ones which allow reconstruction from a few projection angles must meet the condition of being "mostly constant". This is defined mathematically as:

$$\begin{aligned} &\big|(t_1,t_2)|0 \ \leq t_1,t_2 \ < N-1 \ and \\ &p(t_1+1,t_2) \neq p(t_1,t_2) \ or \ p(t_1,t_2+1) \neq p(t_1,t_2)\big| \ \leq B \end{aligned} \tag{4.4}$$

(t_1, t_2) refers to the position of point in the original image, and $p(t_1, t_2)$ is the pixel value at the point, either 0 or 1 for binary image. For being 'mostly constant', it is generally the case that $B << N^2$. For the particle-like Gaussian electron shell model, such condition doesn't hold. Hence the min-cost max-flow algorithm can't be used to reconstruct the beam profile from 2 orthogonal 1D projections.

4.2.2.3 Other Reconstruction Methods

Several other reconstruction algorithms have also been tested. [54]

- Sum Algorithm:

$$I[x][y] = P_x[x] + P_y[y]/2 \tag{4.5}$$

  P_x and P_y are 1D projections in x and y directions. Accurate center of beam is obtained but defect 'bands' similar to the ones appeared in Radon transform method

- Weighted Sum Algorithm, which weighs the projections when only one of the two projections is high at a point. The weight depends on the difference between the projection data for the two directions at the particular point.

The weighted sum algorithm has been tested for a Gaussian electron beam profile reconstruction from two projections in [54]. The centre of the beam is recovered accurately while there exists slight distortion defect. This algorithm didn't give desirable results for the hollow Gaussian beam profile.

Image reconstruction from fewer views is an issue of concern in image tomography. Reduced projection views enables rapid scanning as well as reduced doses. This is desirable in medical imaging as well as many other applications, thus various algorithms have been developed over the past few decades to meet the need. Iterative reconstruction methods, though with higher computational complexity, perform much better than traditional reconstruction techniques in general. Apart from this, there are lower bounds or conditions on projection angles for various iterative methods to produce quality reconstructions. These will be discussed in detail in the further developments section at the end of this chapter.

4.2.3 Hollow Electron Beam Profile Model

Section 4.2.1 has described the difficulty in reconstruction based on two projections. The limitation posed by two projections is that few information can be deducted for the original image and there could be an infinite number of images with the same set of orthogonal projections. Although iterative methods are used to reconstruct images from a small number of projections, there hasn't been any published paper on reconstruction from only two projections without a simplification assumption on the unknown image. What this indicates is that, in an approach to reconstruct the unknown profile susceptible to transient variation in the Gaussian characteristic along the ring, innovations on the iterative method must be made. This requires advanced understanding and skills in tomography.

In most iterative methods, prior information on the beam profile is required to limit the possible solutions given the projection information. The approach to be described below could be applied on the hollow electron beam profile in reality, which shows deviations from the idealised profile. However, the deviations recovered in this case are distorted and show complexity to be processed into a prior image for the subsequent reconstruction. Also, for a real beam profile, update of the whole image instead of beam model parameters, has to be devised when minimising the least square projection error, presenting more complexity and will form the major part of a new iterative algorithm. As a result, an idealised Gaussian profile is used to demonstrate the reconstruction algorithm (back projection combined with least square error minimisation) in this project.

A gray-scale Gaussian ring is synthesised for the purpose of obtaining 1D projections and reconstruction analysis. The synthesised profile is continuous and the pixel intensity at a point indicates relative intensity of the beam.

The simplified model of the Gaussian hollow electron beam profile is an axisymmetric Gaussian ring, i.e. the standard deviation σ of the Gaussian distribution along the ring is uniform. The parameters of such model are:

- standard deviation σ of the Gaussian distribution
- position (x_1, y_1) of the hollow electron beam
- radius r, the distance from the centre of beam profile to the centre of Gaussian distribution

For (x,y) being the pixel position, the beam model is described as:

$$
\begin{aligned}
&R = (R_{inner} : 0.01 : R_{outer}); && \text{define the inner and} \\
& && \text{outer radius of the Gaussian ring} \\
&r = \frac{R_{inner} + R_{outer}}{2}; \\
&\theta = \pi * (-1 : 0.01 : 1); \\
&x = R * cos(\theta); y = R * sin(\theta); && \text{define in polar coordinate} \\
&C = -e^{(-|x^2+y^2-r^2|/2\sigma^2} && \text{C represents the intensity of the pixel}
\end{aligned}
\tag{4.6}
$$

A MATLAB script is written based on the above model along with the built-in function 'pcolor' as follows: p = pcolor(x,y,C); set(p,'LineStyle','none'); colormap gray

The image produced is in uint8 type. Functions 'rgb2gray' and 'imcomplement' were called to produce Figure 4.14

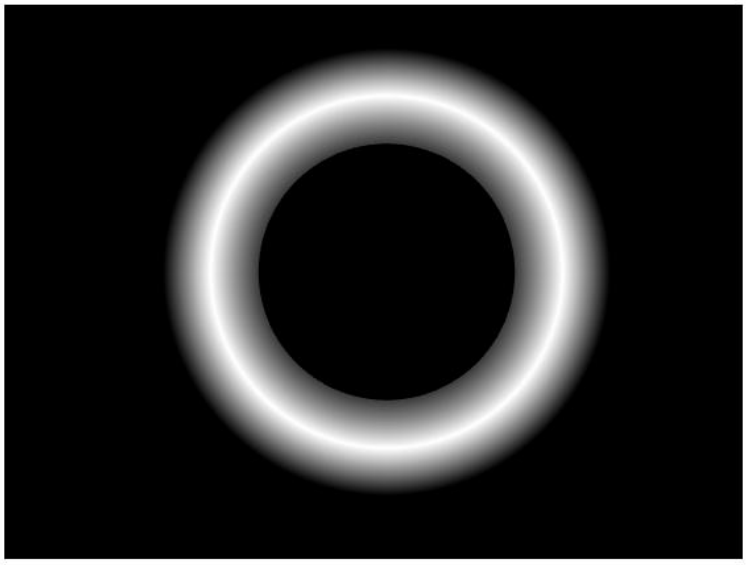


Figure 4.14: Synthesised Gaussian Electron Shell Profile from MATLAB, 420×560

4.2.4 Produce 1D Projections

Two orthogonal projections are utilised for image reconstruction. Each element of a 1D projection is essentially a line integral across the original object. Here the line integral is approximated as the sum of values of pixels along a straight line in the projection angle, which is equivalent to the row and column sums of the digital image matrix. As an illustration, for an image of size 128 $\times$ 64, the x and y projections based on the above model

will be of size 128×1 and 64×1. The exact size of the projections are dependent on the scanning process and detector resolution. For lower detector resolution, there is less information content in the projection data.

For a synthesised profile of data type uint8 (2^8 unsigned integer from 0 to 255), the pixel values cannot simply be added to produce 1D projections. Instead, the 'double' function was called before taking column and row sums of the image. Figure 4.15 shows the 1D projection data:

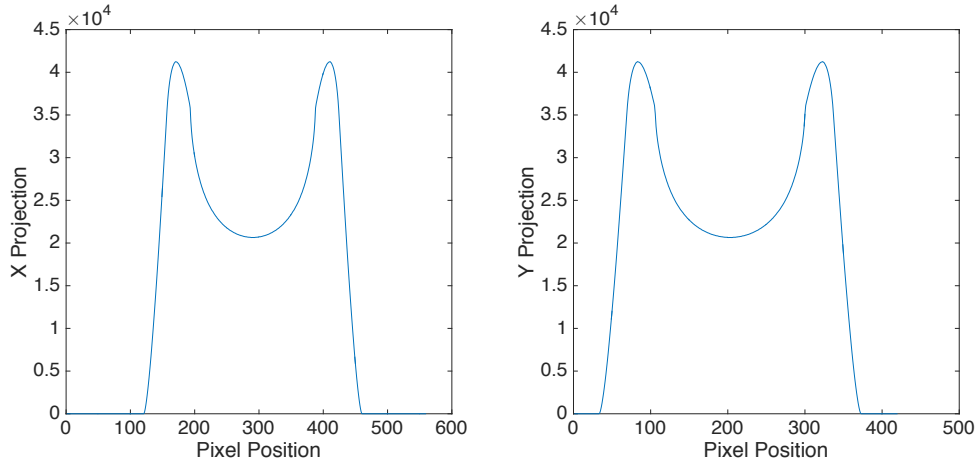


Figure 4.15: Projections in 2 Orthogonal Directions for Figure 4.14

The 1D projections of the hollow electron beam are complementary to the signals against position from detector.

4.2.5 Back Projection and Improvements

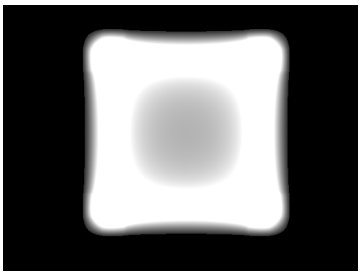
Back projection algorithm is as below:

$$\begin{aligned} m_x &= min\{P_x\} & M_x &= max\{P_x\} \\ m_y &= min\{P_y\} & M_y &= max\{P_y\} \\ f_x(x) &= \frac{P_x x - m_x}{M_x - m_x} \\ f_y(y) &= \frac{P_y y - m_y}{M_y - m_y} \\ I[x][y] &= \frac{P_x[x] \cdot f_y[y] + P_y[y] \cdot f_x[x]}{2} \end{aligned} \tag{4.7}$$

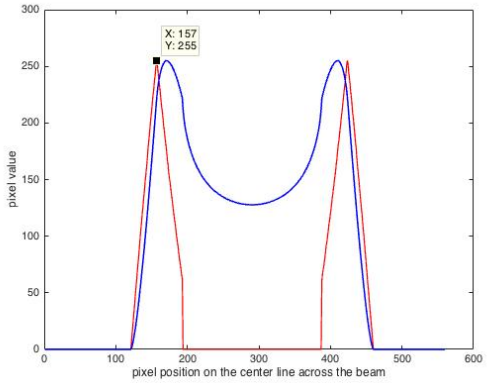
The above algorithm is implemented in MATLAB and the preliminary result shown as an image in double is a 'white' square located at the original position of the beam profile. Nevertheless, by plotting the pixel value against pixel position in the horizontal direction across the centre of square, the pixel values are varying in similar form as the Gaussian

ring profile. The reason for an all 'white' square is due to the pixel intensity saturation, which means that the pixels are white for pixel values above a certain threshold in double.

To visualise the reconstructed beam profile from back projection, the region of non-zero pixels is selected and a threshold is applied. The selected matrix is then normalised to display the beam profile in Figure 4.16a



(a) Reconstructed Beam Profile Based on Back Projection



(b) Plot pixel values along a line across the centre of the beam profile, red: reconstructed profile, blue: original synthesised profile

Figure 4.16: Back Projection Reconstruction

The reconstructed profile shows a square shape, which is wrong but is expected from the back projection algorithm. There is no band distortion as in Radon transform or sum algorithm because the back projection only reproduce a non-zero pixel if both projections are non-zero at a certain point. A horizontal line across the center of beam profile is selected for the reconstructed image and pixel value is plotted. The same line is plotted for the original image as a comparison. The two lines have similar forms at the two ends beyond the peaks. The possibility of estimation of beam profile parameters by fitting to these two end sections then arises.

In reality, only the pixel value plot for the reconstructed image is known (the blue curve in Figure 4.16b). In Figure 4.17 a pixel plot (red) is fitted to the end sections of the blue curve in the least-square sense. The red curve represents the pixel plot of a synthesised profile based on the parameter estimation. A new beam profile is constructed from the estimated parameters and is similar to the original profile.

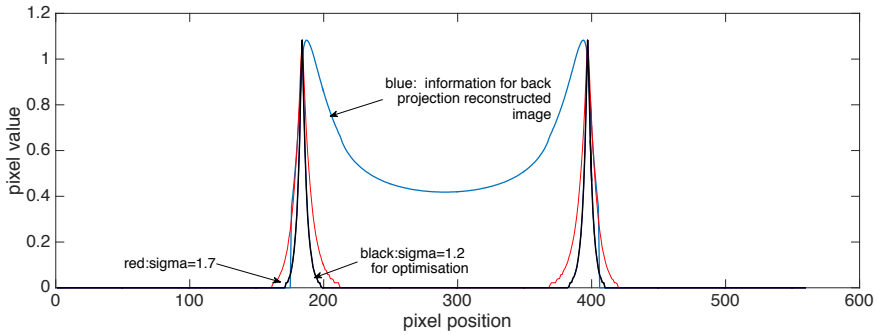


Figure 4.17: Fitting to the Ends for an Estimation of Parameters

4.2.6 Determination of Parameters

The estimated beam profile parameters are updated to minimize the error between 'measured' projections from the original profile and projections obtained from estimated models (will refer to these as 'estimated projections' below) in the least-square case. The centre of the beam is determined exactly by the back projection and the outer radius from projection data boundaries, leaving only r (defined in Section 4.2.3) and σ defined in the beam model to be updated. The expression below illustrates the problem:

$$\arg\min_{\sigma,r} norm\{P_x - P'_x\} \tag{4.8}$$

P_x is the projection measured and P_x' is the projection of the synthesised profile based on model parameters.

By comparing the position and spread of peaks in estimated projections with those in the measured projections, a rough conclusion can be drawn on whether the estimated r and σ are smaller than the true value. The estimated parameters are then incremented or decremented and the least-square error for the projections is calculated for each parameter update.

A MATLAB script for this optimal parameter search has been written. The first step is to generate the original beam profile and store its x and y projections as measured projections. The outer radius R_outer and position of the beam is assigned the value obtained from back projection. Inner radius R_inner is set to R_{inner} = (R_{outer} + r)/2. It turns out that given a prior estimate of the parameters which is close to the real value, r and σ can be updated separately and finally reach the minimum point of the least-square error. That is to say, in updating r while keeping σ constantly equal to the preliminarily estimated value, projection error reaches a non-zero minimum as r reaches its true value. A subsequent search for σ then produces the minimised least-square error. Reducing the step size of each update increases the time complexity of the search, but it ensures a more accurate resultant beam

model. For the beam model in section 4.2.3, the exact beam model is recovered by back projection and 15 overall updates of estimated parameters.

4.2.7 Practical Issues in Reconstruction

4.2.7.1 Obtaining 1D Projection Data from Detector

The 1D projections used for reconstruction are complementary to the signals measured from the detector, since the neutral particle detector measures the neutral atomic beam after interaction with the charged particle beams. Projection data acquisition depends on the scanning mechanism and the atomic hydrogen beam distribution.

If the time taken by the hydrogen beam source to move 2mm (size of H beam) is longer than the dead time of the neutral particle detector, then there will be overlap between two successive readouts. This is very likely to happen because of the fast response of the detector, and can be easily eliminated by introducing a gating function to the detector. After all, the detector provides temporal as well as spatial resolution for the signals, which enables separation of such spatially overlapping signals by simple manipulation of received signals.

The cross-sectional profile of the atomic hydrogen beam must also be taken account of when recovering the 1D projection data. The line through the centre of each beam spot on the detector is used to deduct the 1D projection. However, the distribution of the atomic hydrogen beam profile must be acquired first and be taken into account when reproducing the projection information. This can be determined by a calibration of the atomic beam or during the generation process.

4.2.7.2 Noises

The MCP detector presents a dark noise. Dark noise is background counting distributed uniformly across the detector.

The dark noise of the detector should be determined under the operation voltage. Dark current arises from the following factors:

- electric field emission from channel walls
- ionisation of residual gases in the channel
- local discharge by the high voltage applied
- photo-electron emission by photons produced by electric field scintillation of the MCP support parts

Among these factors, the local discharge effect can be reduced during the fabrication process. Threshold values can possibly be set to distinguish dark noise and the signal from neutral atoms.

Smoothing of the 1D projection data can be done to avoid any unexpected noises, simply by applying a low-pass filter. The order of the LPF should not be too high to avoid over-smoothing and loss of information.

4.3 Extensions to a more general beam profile

4.3.1 Elliptical Beam Profile Reconstruction From Two Orthogonal Projections

A non-circular shaped beam profile can also be reconstructed from 2 orthogonal projections if the Gaussian ring is elliptical. This, however, poses the problem of projections not being aligned with the major and minor axes. Angle θ in Figure 4.18 is an additional parameter for the elliptical beam profile.

Instead of R_x and R_y, R'_x and R'_y are obtained. The relationship between these two sets of parameters is:

$$R_x^2 + R_y^2 = R_x'^2 + R_y'^2 \tag{4.9}$$

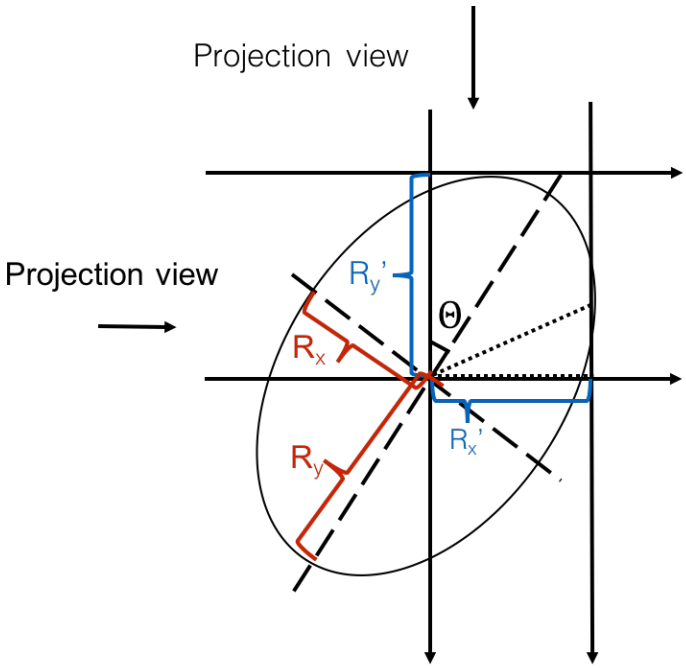


Figure 4.18: Obtaining Projections from the Oblique Elliptical Beam Profile

As for the angle $\theta \in (0°, 45°)$, it has a one-to-one correspondence with set of (R_x',R_y')

values given that the unknown geometry of the elliptical ring is fixed, yet the relationship is non linear. This clarifies that the new parameters R_x, R_y and θ are not independent of each other, and that the minimisation of the projection error needn't be conducted separately for individual parameters. However, the projections in this scenario cannot differentiate between positive or negative θ's with the same magnitude (for example, θ = +30° and -30° give the same projection data for an ideal elliptical profile).

4.3.2 Reconstruction of True Beam Profile From Few Projections

Extensive research has been carried out on quality image reconstructions based on reduced projection views. The reconstruction methods have moved over simple analytical methods to iterative methods. Iterative reconstruction techniques mostly rely on minimisation of a certain cost function. One of such processes has been introduced in 4.2.2 for binary images under certain conditions. Other widely-used algorithms include total-variation (TV) minimisation[55], simultaneous iterative reconstruction technique (SIRT)[56], as well as their modified versions[57]. Many of them were patented. It is generally accepted that with more projection views, the quality of image recovered is better or otherwise the computational complexity reduces.

Among these research results, the least number of projection angles required for reconstruction is 22. A perfect reconstruction from 22 sparse view-angles is claimed by [58] mainly based on the total-variation minimisation.

With only two projection views, there are limitations on the reconstruction. The analysis relied on simplified beam models, whilst the aim of the beam profile imaging is the monitoring of variations of the Gaussian distribution along the electron shell. To meet such requirement, more projection view angles or breakthroughs in image reconstruction technique will have to be achieved.

Chapter 5

Imaging the Proton Beam

Earlier research showed that the number of photons due to fluorescence by the proton beam would be 12 orders of magnitude smaller than that of the electron beam. Therefore, a separate system was required to image the proton beam on it's own. Initially a simplistic pinhole and camera design was considered. However, a lens can have a large aperture allowing for greater light collection and therefore it will have more accurate results.

5.1 Lens Modelling Techniques

5.1.1 The Thin Lens Equation

The thin lens Equation can be used as long as the assumption that the lens radius is much smaller than the distance to the object holds true [59]. This allows the simplification that $\theta \approx \sin\theta \approx \tan\theta$.

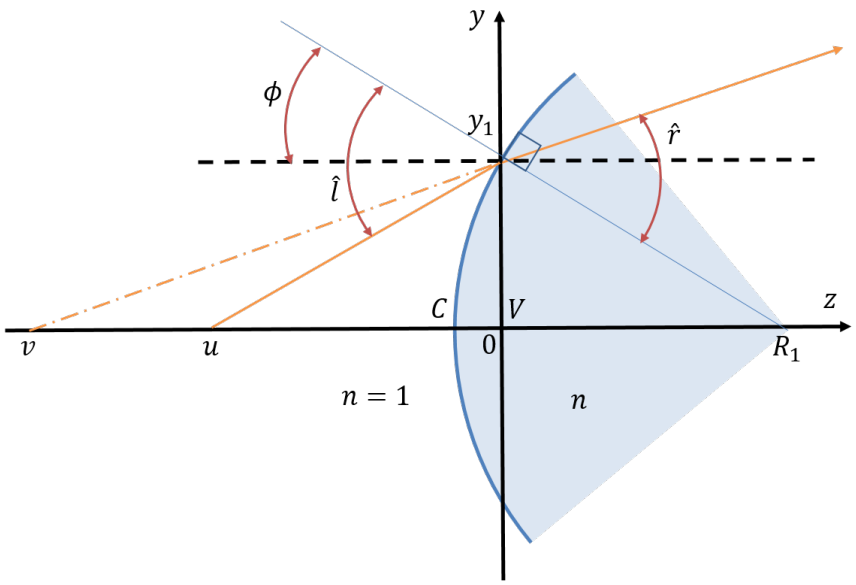


Figure 5.1: Thin Lens Equation from [59]

Equations derived from figure 5.1 after making the approximation that $y_1 \ll R_1$ and $0 \approx VC \ll R_1$

$$\hat{l} - \phi = -y_1/u \qquad \hat{r} - \phi = -y_1/v \qquad \phi = y_1/R_1 \tag{5.1}$$

Rearranging these three equations gives:

$$\frac{\hat{l}}{\hat{r}} = n = \frac{y_1\left(\frac{1}{R_1} - \frac{1}{u}\right)}{y_1\left(\frac{1}{R_1} - \frac{1}{v}\right)} \tag{5.2}$$

Which can be simplified to:

$$-\frac{n}{v} + \frac{1}{u} = \frac{1}{R_1}(1-n) \tag{5.3}$$

For a second coincident surface of radius R_2 the image produced by the first surface is treated as the object of the second surface. For just the second surface, by following the earlier steps it gives:

$$-\frac{1}{v'} + \frac{n}{v} = \frac{1}{R_2}(n-1) \tag{5.4}$$

v' is the position of the final image. We can now put equations 5.3 and 5.4 together to obtain:

$$-\frac{1}{u} + \frac{1}{v'} = \frac{1}{f} \quad \text{where} \quad \frac{1}{f} = (n-1)\left(\frac{1}{R_1} - \frac{1}{R_2}\right) \tag{5.5}$$

On the left is the thin lens equation and on the right is the lens-maker's equation.

5.1.2 Matrix modelling

The main method for modelling compound lenses, as used by optics designers and built into professional optical software, is the matrix representation of a lens. From before it would mean representing the thin lens equation in a matrix form allowing transformation matrices to be used to map the input height y and angle θ from the optical axis on to outputs of the same form.

$$\begin{bmatrix} y_2 \\ \theta_2 \end{bmatrix} = \begin{bmatrix} 1 & 0 \\ -\frac{1}{f} & 1 \end{bmatrix} \begin{bmatrix} y_1 \\ \theta_1 \end{bmatrix} \tag{5.6}$$

This method would give the most realistic results, however it has a number of drawbacks. Firstly, it requires knowing the dimensions and surface function of every individual lens within the compound lens. Secondly, since all the rays leaving a point on the object plain must arrive at the same point on the image plain regardless of the direction they set off in. Assuming they pass through the aperture, if the sensor is situated away from the

image plain, then the only way to build up the total image, is to initialise a large number of rays from each point in the object. Using a random number generator, each ray would be assigned an angle. From here, by multiplying by the transformation matrix of every individual lens in the system, the ray can be mapped on to a point on the sensor plane. By doing this for every ray a full image will be produced on the sensor.

Considering this is a proof of concept study and that computing power is limited. This approach of modelling every individual ray is far too computer intensive and for test purposes would take far too long to build up a single image. Taking into account it also requires information about pre-manufactured lenses that is not normally available, this does not seem like an approach that is likely to work.

5.1.3 Aberrations

While modelling is most easily done by using the thin lens equation in reality it is not practical to use a single thin lens. This is due to optical aberrations which are corrected for in well-designed compound lenses. Notable aberrations are: spherical aberrations, which cause images to appear blurred, as rays hitting the edge of the lens focus at a different point to rays at the centre and coma, which causes off axis point sources to appear comet shaped due to the angle at which light hits the lens [60]. For well corrected systems the Abbe sine rule will mostly hold true:

$$\frac{n \sin \theta_1}{n' \sin \theta_2} = constant \tag{5.7}$$

θ_1 and θ_2 are respectively the angle of any ray leaving a point object and the angle forming the image, relative to the optical axis. n is the refractive index. If the Abbe condition holds true, the entire surface perpendicular to the axis is imaged perfectly [61].

However, this assumption does not apply to rays with angles greater than the marginal ray i.e. a ray with the largest angle admitted by the system aperture. Due to the proton core being extremely small and since the front of the lens will have to be a safe working distance away from the high energy beams, it is unlikely the proton core being imaged will produce rays which exceed the marginal ray, therefore this is not an issue in the design.

Since it would be beneficial to ignore the effects of spherical aberrations and coma, a pre-built, well-corrected compound lens will be used. This means that a brand new optical system will not be designed from scratch as this would require specialist software not available for this project to design it to sufficient accuracy.

5.1.4 Depth of field

Since the system being developed has a 2 mm wide neutral beam, at any one time, a large proportion of the proton and electron beams will be excited. Therefore, it is imperative that we are able to model how out of focus light is perceived on the sensor so that we can make sure blooming does not occur if light from the electron shell is to hit the sensor.

When a point in an object is out of focus, it creates a circle of intensity rather than a point on the image plane [62]. As long as the diameter of the circle formed is smaller than the resolution of the imaging device, which in this case, is the size of the pixels in the camera sensor, then the level of defocus present will not be noticeable. The requirements of the system mean that a shallow depth of field would be beneficial to our application. This would mean only the centre of where the neutral beam is excited would be imaged.

5.2 Computer Modelling

Since there was no access to any professional grade optical design software, a much simpler tool was built using MATLAB so that potential lenses could be tested to see if they meet the necessary requirements.

5.2.1 Using the thin lens equation to model the blur circle

The issue with all earlier methods was that they only modelled points from a single object plane to a single image plane [63]. Therefore, since perfect focusing would not be possible except for a single plane, a model was built to simulate light from points away from these planes. Using similar triangles the diameter of the blur circle is found to be:

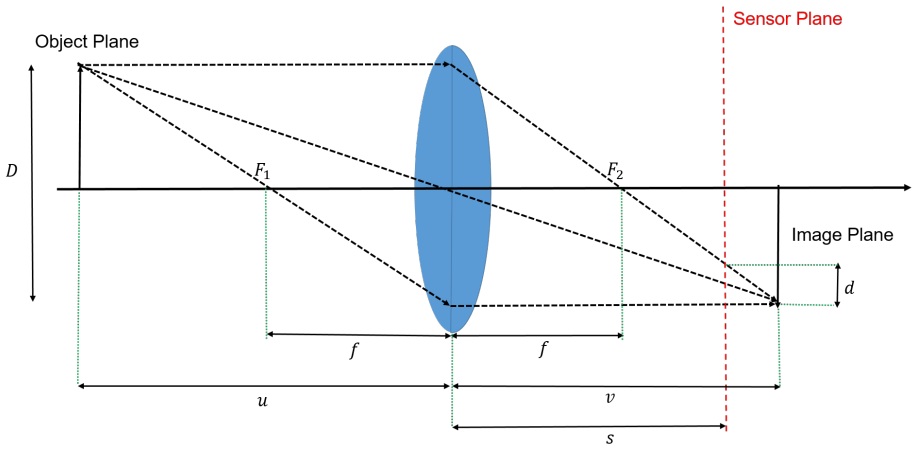


Figure 5.2: Blur Circle diameter formula

$$d = \frac{D|s-v|}{v} = \frac{f|s-v|}{Nv} \tag{5.8}$$

All lengths are shown in figure 5.2. N is the F-number of the lens and f the focal length. From the thin lens equation, where M is the magnification:

$$v = \frac{uf}{u-f} \qquad M = \frac{-v}{u} = \frac{-f}{u-f} \tag{5.9}$$

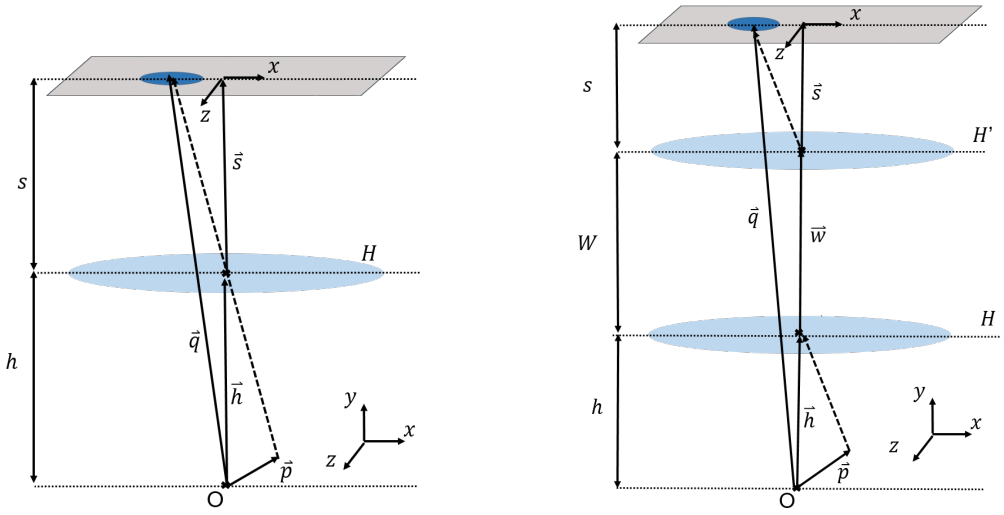
Therefore, the radius of the blur circle becomes:

$$r = \frac{D}{2}\left|\frac{s}{v} - 1\right| = \frac{D}{2}\left|-\frac{s}{Mu} - 1\right| \tag{5.10}$$

In the system the $x-y$ plane is taken to be the cross section of the proton and electron beams i.e. the final output image that is to be achieved. The origin is taken to be the centre of proton beam and z to be the distance towards the lens and camera. By using the principal that the direction of a ray going through the centre of the lens does not deviate [64], we are able to calculate the centre of the blur circle on the sensor plane. The vector $\vec{q}$ is determined to be:

$$\vec{q} = (1+k)\vec{h} - k\vec{p} \qquad where \qquad k = \frac{s}{h-y} \tag{5.11}$$

As shown in figure 5.3a, h is the distance from the origin to the thin lens, $\vec{p}$ is the vector to the point we are calculating the blur circle for and y is the corresponding coordinate in $\vec{p}$.



(a) Blur Circle centre formula

(b) Accounting for Lens Thickness

Figure 5.3: Vector approach to Light Mapping

5.2.2 Accounting for Lens Thickness

It was quickly found that while the thin lens equation for the purposes of computer simulation provided a reasonable solution, as a virtual representation of a real-world lens it was lacking in enough detail to display the output accurately. The changes made involve separating out the principal planes of the system as shown in figures 5.3b and 5.4. While the equation for the blur circle radius remained the same, the equation to calculate vector $\vec{p}$ is altered to:

$$\vec{q} = (1+k)\vec{h} + \vec{w} - k\vec{p} \qquad where \qquad k = \frac{s}{h-y} \tag{5.12}$$

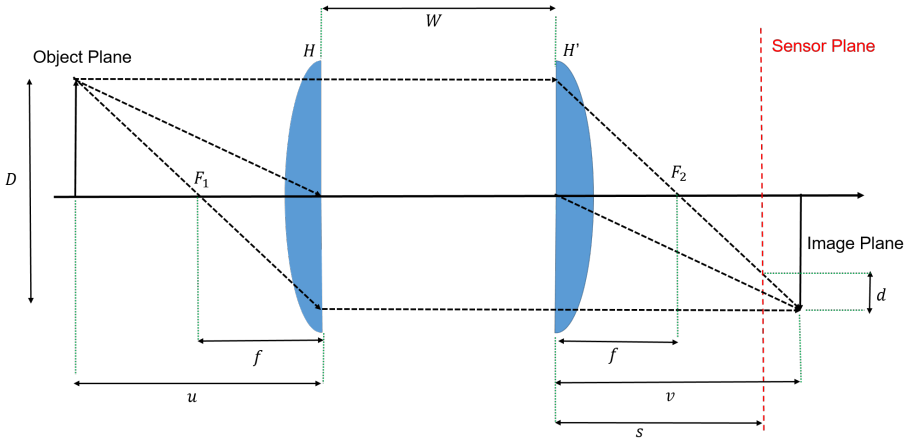


Figure 5.4: Thick lens Representation

5.2.3 Test Data

Initially the test data was composed using the formula for a Gaussian distribution in terms of the radius from the centre of the beam. Using the diagram given in the brief shown in figure 1.1a, the boundaries were taken to be: $r_a = 3\sigma$, $r_b = 4.5\sigma$ and $r_c = 7.5\sigma$ starting from the centre and going outwards, where $\sigma = 1mm$. It was quickly decided that the model would run quicker if a grid based system was formed and the number of particles in each cell was represented rather than having a huge array storing the coordinates of individual particles as shown in figure 5.5.

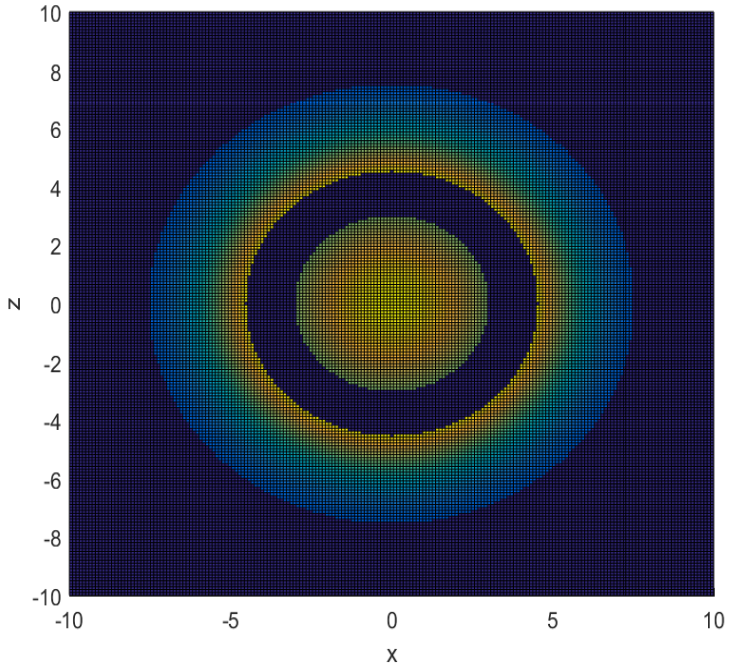
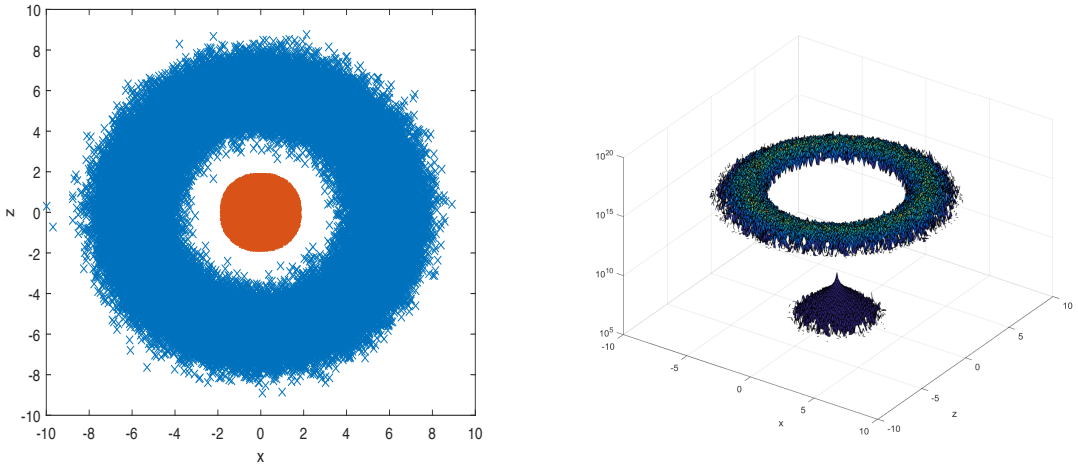


Figure 5.5: Profile formed using Gaussian formula

This was fine for preliminary testing, however, since it always provides the exact same data, it would prove to be less useful when it would come to reconstruction in section 5.5.

To randomise the data, functions in MATLAB were used which generate random numbers from a normal distribution for the radius, and a standard random number generator was used to generate an angle between $-\pi$ and π. For this section we only model the light output due to fluorescence. From section 2.3.2 it is clear that the proton beam signal would be a factor of 1×10^{12} smaller than the electron signal. Therefore, tuning factors were added into the script to alter the relative sizes of each beam profile. Figure 5.6b has a log axis to show the relative strengths of the beams. Earlier it was discussed that the equation for fluorescence used a constant that was based on experimental data which is not available.Therefore, this is an unfortunate unknown in the analysis and so an arbitrary constant has been added to the number of photons produced which could be changed at a later date when the data does becomes available. However, the relative strengths of these signals is known and the outcomes of the simulation still prove true regardless of the constant used.



(a) Particle Representation (b) Discretised Grid Representation

Figure 5.6: Randomly generated data

5.2.4 Aperture

The proportion of light entering the aperture is equal to the solid angle produced by the aperture divided by the solid angle of a sphere which is 4π. The solid angle is defined by equation 5.13 [65] where $\hat{\boldsymbol{n}}$ is a unit vector from the origin, $d\hat{\boldsymbol{a}}$ is the differential area of a surface patch, and r is the distance from the origin to the patch:

$$\Omega \equiv \iint_S \frac{\hat{\boldsymbol{n}} \cdot d\boldsymbol{a}}{r^2} \tag{5.13}$$

To calculate this to a very high accuracy for a circular disk requires finding the solution to Legendre's form of the complete elliptic integrals of the first and third kind. It also requires finding solutions to Heuman's lambda function [66]. While this is possible using MATLAB, it is computationally complex to perform and would greatly slow down the simulation. Considering that a much simpler approximation can be used - that the proportion of light that enters the aperture is approximately $D^2/16r^2$ where D is the diameter of the aperture and r is the distance to the lens opening, it seems sensible to avoid doing this calculation.

5.2.5 Sensor Noise

Currently, the system has been modelled as an idealised form of a real-world system. While the assumption to ignore aberrations can be justified, ignoring noise as a result of sensor phenomena is less convincing. There are two types of sensor noise present. Shot noise, which is the result of current being made up of discrete charge packets, electrons, which

fluctuate following Poisson's distribution. There is also thermal noise, which is dependent on the operating temperature of the CCD camera [67].

From section 5.4.2 it was decided that by using an image intensifier, the signal to noise ratio could be dramatically increased. Therefore, these two issues become far less of a problem. Thermal noise can be reduced by extra cooling if required, which seems unlikely to be a problem considering the level of cooling already in place around the LHC. Therefore only shot noise will be added to the model which is given the standard power of $\sqrt{signal}$ [67].

5.2.6 Final Model

In the model, beam position, refers to the current centre y-position of the neutral beam with reference to the pipe centre origin. Figures 5.7 and 5.8 show examples of perfect and imperfect focusing at beam position 1.2 mm. Figures 5.9 and 5.10 show the model at beam position -5.6 mm.

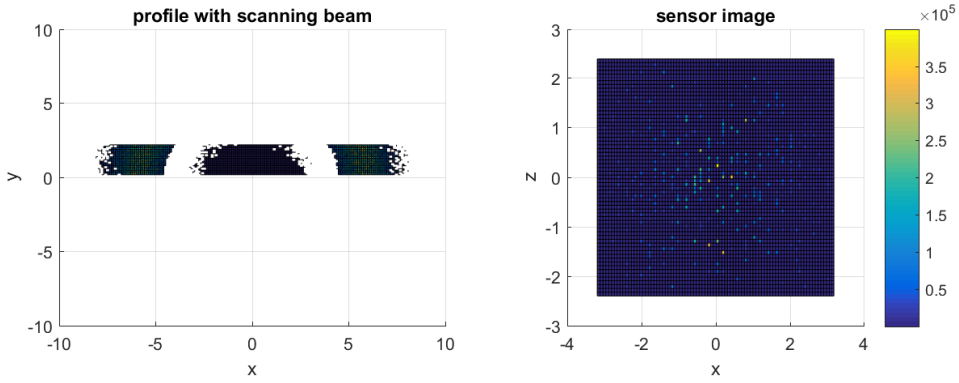


Figure 5.7: Perfect Focusing, beam position 1.2 mm

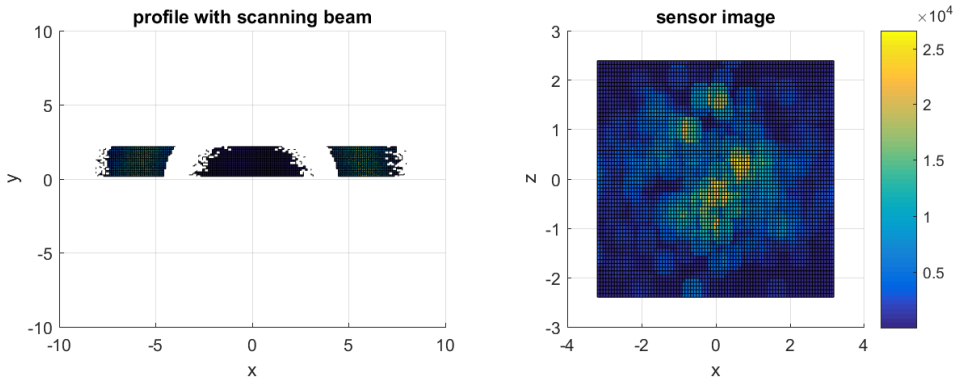


Figure 5.8: Imperfect Focusing, beam position 1.2 mm

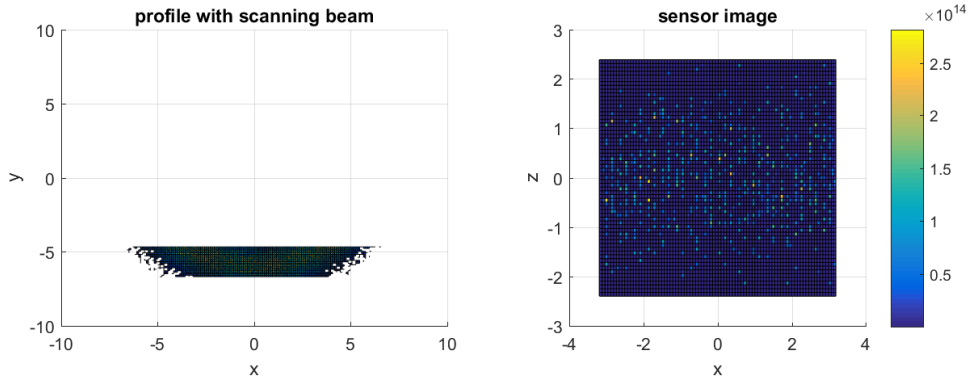


Figure 5.9: Perfect Focusing, beam position -5.6 mm

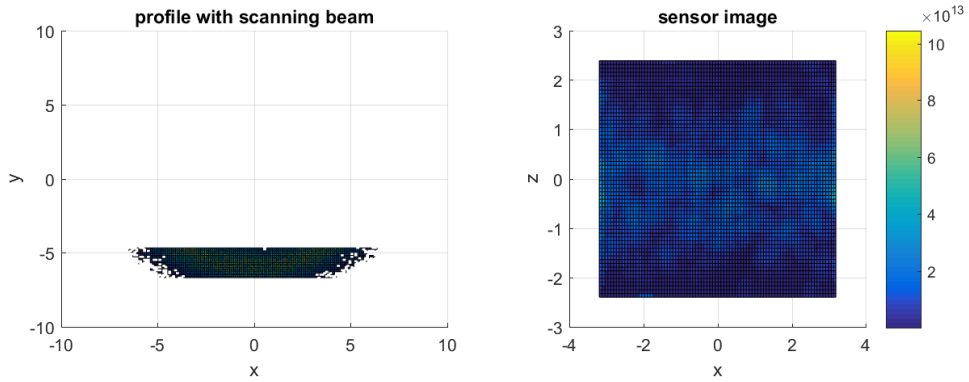


Figure 5.10: Imperfect Focusing, beam position -5.6 mm

5.3 Choice of Lens

Now that a fairly accurate model of a lens has been built and the parameters of the system can be tested by means of a computer simulation, a lens could now be selected. There are many different types of lenses available. To decipher which would have the most promising properties, a table of comparison was used, shown below with the justification explained in the text.

5.3.1 Single Lens

Single lenses, as mentioned earlier are good from a design point in that all the parameters of their use are easily calculable. However, their limitations apply not only to aberrations. The depth of field calculated for tolerated distances is much too high and the angle of view is unalterable. Magnification is dependent entirely on the distance the object is placed to the lens and there is no easy method of altering this while keeping alignment perfect. Small apertures are determined mostly by the diameter of the lens which means very little light

collection, unless placed very close to the beams. Extremely small working distances are required, so that they would have to be placed less than 10 mm from the centre of the beam which is almost within the given dimensions of the beam and would be completely unsafe.

While aspherical lenses can be used to lessen the effects of aberrations, due to their simplistic design, some will still remain. The more pressing issue is that there is no flexibility in the design and the distances they are designed to work at make these totally infeasible.

5.3.2 Bi-Telecentric Lenses

Shallow depth of fields are available suited for this application. However, there is a trade off between depth of field and working distance so that a shallow depth of field requires a working distance which would possibly place it too close to the high energy beams and would therefore be unsafe. Large fields of view are also a problem, which would unavoidably capture images of the electron shell as well making it impossible to differentiate between the two. These lenses offer constant magnification across the depth of field, which would mean the magnification would not change independent of the object location. However, this means only set magnifications are available which may mean that those required fall outside the range needed. Typically very low apertures- the minimum f-number available is only as low as f/3.7. This means low light collection and leads to higher depths of field. However, there are a large number of working distances available so it is likely one is found which falls within the required range.

Aspects of this camera type do match the requirements - however, there is always a trade off between desirable characteristics which make it not so ideal for this task.

5.3.3 Standard Fixed Focal Length Lenses

These lenses have large depths of field since they are designed for capturing images of objects at a reasonable distance. Their field of view is similarly big however, this can be reduced by choosing a smaller sensor format which would unfortunately mean a loss in resolution and lower image quality. Limited magnifications are available for these lenses therefore, it's unlikely a matching magnification would be found for a set focal length and working distance. Large apertures are available as f-numbers as low as f/1.4 are common meaning a large collection of light and therefore will be useful for faint signals. Typically large working distances are required with these, which equate to large fields of view, which places these in severe conflict with system requirements.

Fixed focal length cameras are unlikely to work as their large depth of field and relatively high field of view makes them unsuited for imaging only the proton beam over a small finite area.

		Types of Lens			
Weighting	Attribute	Bi-Telecentric Lenses	Single Lens	Zoom	Standard Fixed Focal Length
4	Depth of Field	4	2	5	2
5	Field of View	1	2	5	3
3	Magnification	2	2	5	3
3	Aperture	2	1	5	5
4	Working Distance	4	0	4	2
	Weighted Score	3.3	1.8	4.8	2.9

Table 5.1: Lens Type Comparison

5.3.4 Zoom Lenses

Zoom lenses can be made to have very shallow depth of fields, however there is a trade off between this and the working distance. Therefore, they must be placed very close to the beams to achieve shallow depths of field. However, a large range of working distances is available so that it's likely the system can be placed a safe distance from the beams. These lenses can have extremely narrow fields of view. In this respect these lenses are the most suited for the task, since they are most likely to allow imaging of just the inner proton core. High variability in magnification means these are the most likely to have a magnification that falls within our range. A large aperture variability within single models is also available due to fine tuning of focal length.

These are by far the most suited to the task. While having parameters that match most of the requirements, they give the most flexibility in terms of zoom and fine focusing. Most of all, the narrow field of view is a requirement that none of the other lenses seem to be able to match.

5.3.5 Final Choice

For the final choice of lens the model chosen is a combination Navitar Zoom Lens. It is comprised of a 6.5X Zoom Lens, a 0.67X Adapter Lens and a C-mount coupler which will be used to connect the lens securely to the camera chosen later. It has the following properties:

- Working Distance: 92 mm
- System Magnification: 0.47 - 3.00
- Depth of field: 0.95 mm - 0.10 mm
- Field of View: 2.01 mm - 34.02 mm

This specific lens was chosen for a number of reasons. Firstly the working distance means it is outside of the 'unsafe' region around the beams which is taken as being 80 mm from the centre of the proton beam. Therefore, there is enough of a safety factor so that there is no chance of the proton and electron beams ever coming into contact with the lens causing hazardous collisions with detrimental consequences. Depending on the sensor used a magnification of approximately 1.6 will be required and this number falls close to the centre of the limits for this model so there is room for fine tuning if needed. At 0.1 mm a reasonably shallow depth of field can be achieved for precise imaging of the single plane we are interested in at any one time. Entirely dependent on the sensor size chosen, the field of view can be made to be extremely narrow so that only a very thin selection of the proton beam can be picked out while ignoring the electron shell. A field of view of about 6 mm will be required in the centre of the beam down to an even smaller number while imaging the edges of the proton core.

Another interesting feature of this lens is the ability to have the focus and zoom controls motorised. This would allow the field of view to be finely adjusted as different depths within the proton beam are being scanned.

5.3.6 Motorised Control

The main choice of motors is between stepper and servo motors. A stepper motor works by exciting different coils at a time and therefore the rotor is positioned in discrete pre-planned positions. The servo motor contains a proportional - integral - derivative (PID) negative feedback controller [68], allowing it to correct itself for errors if it was too close to the solenoid field. This gives it a major advantage over a stepper motor which would have no way of correcting itself. A servo motor also provides greater flexibility to be reprogrammed if requirements change slightly.

While motorised control would allow much greater fidelity over the focus and magnification, the standard motor options would be unlikely to work in practice. This is because these attach near the front of the lens putting them in close proximity to the 7 Tesla magnetic field. They also require a much larger hole to be made in the side of the beam pipe which would mean removing more of the solenoid around the outside causing unpredictability in the electron lens.Therefore, a bespoke solution would be required as discussed in the further developments section.

5.4 Choice of Camera

5.4.1 Sensor

Two different sensor technologies are currently employed in modern cameras - complementary metal-oxide-semiconductors (CMOS) or charge-coupled devices (CCD). Historically, CCD cameras have been the norm due to simpler fabrication techniques, however CMOS cameras have matured in recent years to provide a suitable alternative. Both devices consist of an array of photodetectors which produce an output electrical signal as a result of incoming photons [69]. In CCD sensors, every pixel's charge is transferred through a very limited number of output nodes where it is converted to a voltage, buffered, and is output as an analogue signal. In CMOS sensors, every pixel has its own charge to voltage conversion. Each sensor often also includes amplifiers, noise correction, and digitisation circuits, so that chip outputs are digital bits [70]. Neither technology is perfect as both have advantages and disadvantages.

5.4.1.1 CCD

CCD sensors suffer from blooming, where overexposure causes charge to leak on to neighbouring pixels, causing distortion in large portions of the sensor. Smearing can also occur causing bright streaks to appear across the image. They have global shutter meaning that the image is collected all at once and therefore high speed objects are less subject to blurring. Noise is less of an issue with CCD sensors although shot noise is still inherently there as it is in all electrical systems. CCDs have a much higher dynamic range which means the ratio of the saturation signal divided by the base noise signal strength is large. This means that the camera is able to comfortably capture a larger range in signals, although it is unlikely the ratio will be the many orders of magnitude required for this application.

5.4.1.2 CMOS

CMOS sensors have naturally less blooming since each pixel is self contained and is not designed to distribute charge from one pixel to the next. They use a rolling shutter, meaning that pixel values are taken at slightly different times which can lead to high speed objects appearing blurred. Unfortunately, they have much higher noise which is a problem with low light intensity applications and their dynamic range is often much lower.

Although the exact level of fluorescence is an unfortunate unknown in this analysis, it is likely the amount of light produced will be quite small. Therefore, noise is an important factor as a small signal will be harder to distinguish with high noise present. Therefore, this has been decided as the most important factor. If it was found through experimentation that

the number of photons produced by fluorescence was quite high, then the anti-blooming capabilities of the CMOS sensor would become the most important factor however, it is assumed that through the choice of lens, the photons produced as a result of the electron shell should not hit the sensor at all.

		Sensor Type	
Weighting	Attribute	CMOS	CCD
3	Anti blooming	4	2
4	Shutter	2	5
5	Noise	2	4
4	Dynamic Range	3	5
	Weighted Score	2.6	4.1

Table 5.2: Sensor Comparison

5.4.2 Image Intensifier

Since we were aiming to limit sensor noise while improving the signal strength it was decided that the camera should have a built-in image intensifier. This is because these devices vastly improve the signal to noise ratio by amplifying the number of photons before they hit the sensor. An image intensifier consists of the following major components: an input window, an input phosphor and photocathode, several electrostatic focusing lenses, an accelerating anode, an output phosphor screen, and a protective vacuum case [71]. Incident photons hit the phosphor screen causing release of secondary electrons. These are then accelerated by an electric field where they collide with the second phosphor screen causing release of a far greater number of photons which are then measured by the CCD.

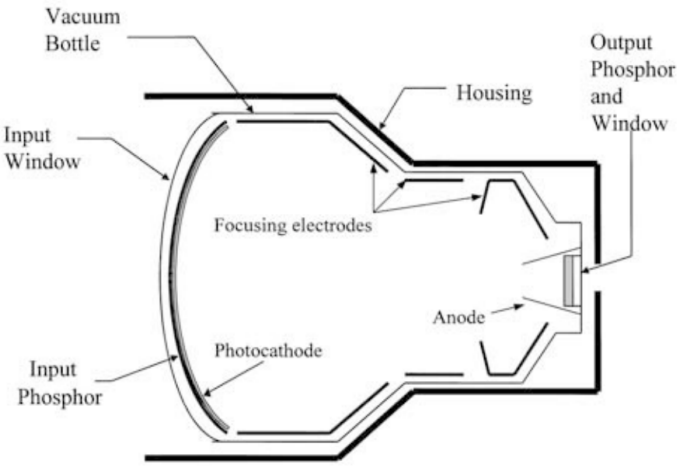


Figure 5.11: Image Intensifier from [71]

5.4.3 Final Camera Choice

For the choice of camera it was decided a nanosecond high speed ICCD camera from Stanford Computer Optics would be used [72]. Specifically, the '4 Quik E' model, which has the following properties:

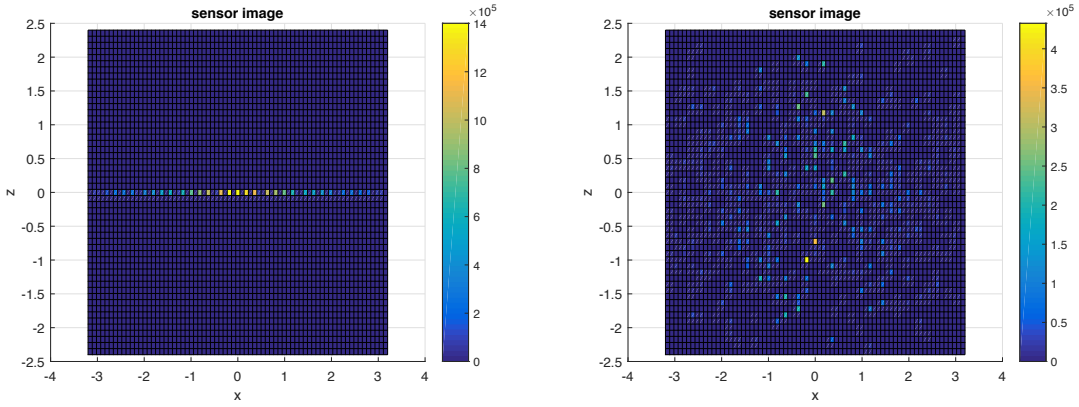
- Gate time down to 1.2 ns
- Very high resolution at 1360 x 1024
- C-mount optical interface
- Image intensifier is highly configurable:
  - S20 photocathode with spectral range 165 - 820 nm
  - Dual stage micro-channel plate
  - P46 phosphor screen
- Fiber optic coupling between CCD sensor and image intensifier for best image quality

This camera is an excellent choice for a number of reasons. The image intensifier can be used for vast improvement in the signal strength. The chosen photocathode has a large spectral sensitivity meaning it should be able to capture photons within the visible spectrum. By choosing a dual stage micro-channel plate the signal strength can be increased by a factor of 10^8 which accelerates electrons while maintaining spatial resolution. The best choice of phosphor screen is type P46 which has the following composition $Y_3Al_5O_{12} : Ce$ and has a decay time of 0.2 μs from 90% to 10%. Since the decay time is quite high relatively, a reasonable delay must occur between each image. This means that imaging of individual proton bunches will not be possible, although each image slice could be taken from a single bunch.

5.5 Proton Beam Reconstruction

Once the parameters from sections 5.3 and 5.3 had been input into the model from section 5.2. It was time to test whether the original proton profile could be reconstructed. The reconstruction process can be seen as having a number of steps associated with it:

- Integration along one dimension to form one-dimensional slices of the final image.
- Digital filtering to eliminate sensor noise and to smooth the data.



(a) Image due to Infinitesimal Beam (b) Image due to Wide Gaussian Beam

Figure 5.12: Image captured on camera sensor at Beam Position 1.2mm

- Compiliation of slices into a matrix.
- Approximation of data between slices to build up the full 3D image.

5.5.1 Integration of Data

If the neutral scanning beam was taken as having infinitesimal diameter, the image that would appear on the screen would consist of a single line of pixels. However, since the beam is better approximated by a 2mm wide Gaussian beam, the image that is produced becomes spread out in the z direction on the sensor. Assuming the camera and lens system is well aligned so that the z-plane of the proton and electron beams is the same for the sensor, then to represent a single slice of the proton beam, we integrate along the z-axis, which computationally can be seen as a summing function along one dimension.

5.5.2 Smoothing the Data

Smoothing the data is necessary because a high resolution camera is being used to model highly focused light, this results in a large number of pixels containing only the baseline noise signal. As a consequence, the final algorithm used has trouble reconstructing an accurate image as it considers these much smaller values to be actual data points when they are not. Therefore, cells which only represent sensor noise should be removed from the data.

There are several different techniques for smoothing the data using digital filters. For the most part digital filters are an example of weighted moving average filters [73]. Non-recursive, finite impulse response filters would be used over recursive filters, since recursive filters rely on past output values whereas non-recursive filters use only input values

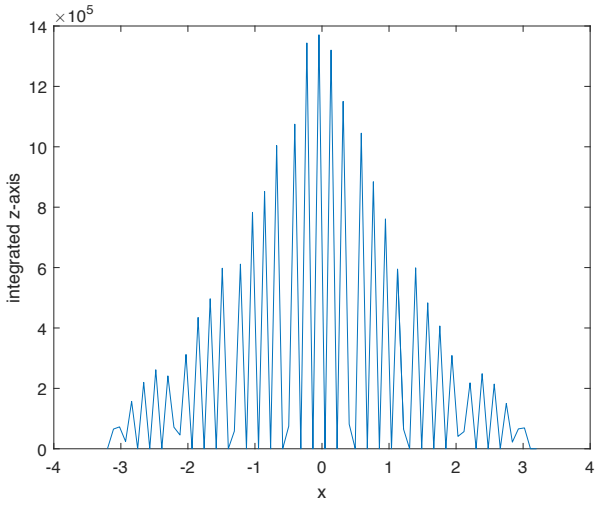


Figure 5.13: Integration of Image along z-axis from figure 5.12b

[74]. The other advantages of a non-recursive filter is that they are naturally stable and also by using a symmetric window have linear phase delay. This means all frequencies are shifted by the same amount and so this is easy to correct for. There are a huge number of window functions available for this process, each with their own characteristics.

5.5.3 Rectangular Window

Rectangular window functions are the most basic example compromising of equally weighted samples. Despite being the simplest, this discrete function is considered optimum for the problem of reducing white noise in the signal, while keeping the sharpest step response [75]. Each data point follows the formula given below, where $2N + 1$ is the size of the window function. Y_i is the smoothed value for the ith data point, where X values are the input values.

$$Y_i = \frac{X_{i+N} + X_{i+N-1} + \cdots + X_{i-N}}{2N + 1} \tag{5.14}$$

The effects of increasing the window size are shown in figure 5.14a. However, a number of issues can be seen in this graphic. As the window size increases the amount of smoothing and removal of base line noise points gets better. However, this also leads to a significant flattening of the peaks and therefore making important peaks less visible. As window size increases it also leads to a significant increase in skew of the data. This is due to the group delay of the window function. Converting equation 5.14 into the z-domain, as an example for the function with a window size of 5:

$$Y(z) = \frac{X(z)}{5}[z^{-4} + z^{-3} + z^{-2} + z^{-1} + 1] \tag{5.15}$$

By setting $z = e^{jwT}$:

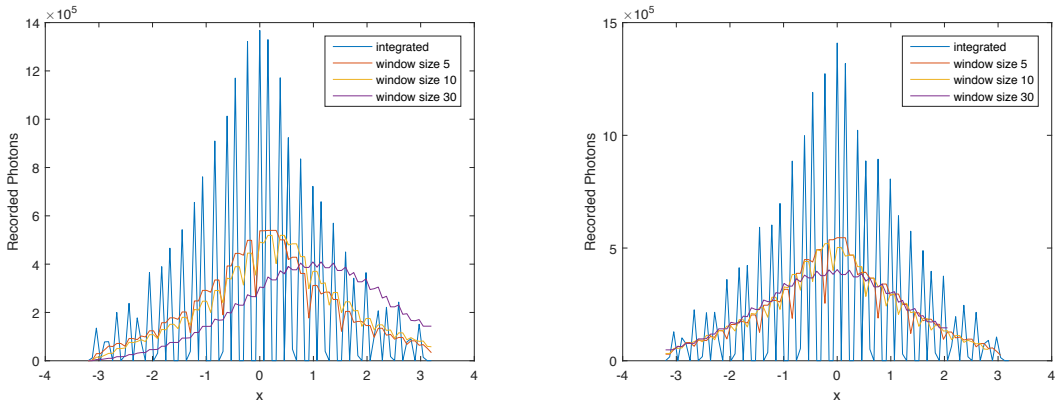
$$G(z) = \frac{e^{-2jwT}}{5}[e^{-2jwT} + e^{-jwT} + 1 + e^{jwT} + e^{2jwT}] \tag{5.16}$$

$$G(z) = \frac{e^{-2jwT}}{5}[2\cos 2wT + 2\cos wT + 1] \tag{5.17}$$

Group delay is defined as:

$$-\frac{d}{dw}(\angle G(w)) \tag{5.18}$$

Therefore, we find the group delay in this instance to be $2T$. The group delay of a rectangular window function can therefore generally be defined as being NT when the window size is equal to $2N + 1$. The group delay can therefore be found computationally, where it is subtracted from the filter outputs to give a corrected form as shown in figure 5.14b. From now on, all filters will be applied with the effects of group delay corrected for.



(a) Group delay unaccounted for

(b) Group delay accounted for

Figure 5.14: Different rectangular window sizes at Beam Position 1.2mm

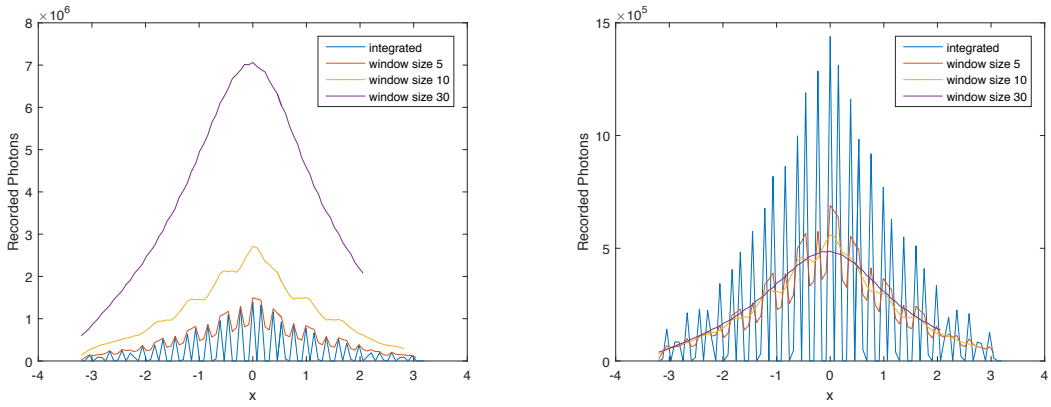
5.5.4 Hamming Window

The Hamming window was also considered. Generalised Hamming windows coefficients are of the form [76]:

$$\omega(n) = \alpha - \beta\cos\frac{2\pi n}{N-1} \tag{5.19}$$

Hamming window coefficients are taken to be $\alpha = 0.54$ and $\beta = 0.46$. These are optimised values, designed to minimise the amplitude of the nearest side lobe in their frequency

spectrum. An issue with applying a weighted function to the data as oppose to just averaging points is that the output of the filter requires scaling to be representative of the original data. Figure 5.15a shows the result without scaling applied and figure 5.15b shows the result when the output is scaled by the ratio of the integrated functions mean to it's own mean.



(a) Scaling unaccounted for

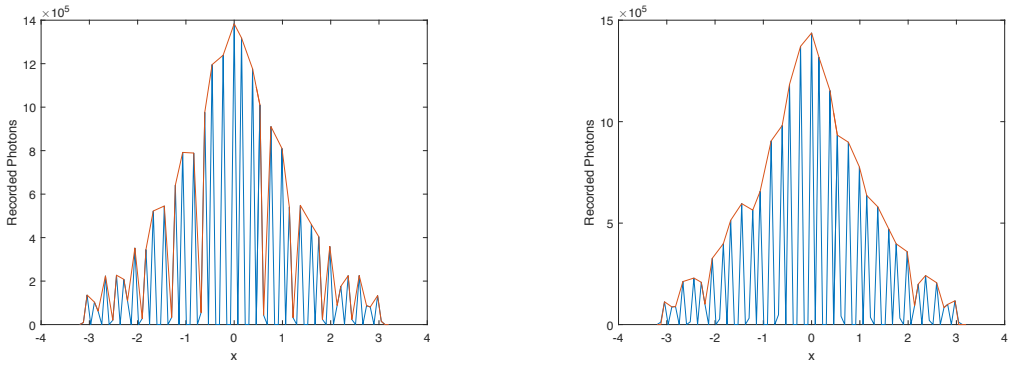
(b) Scaling accounted for

Figure 5.15: Different Hamming window sizes at Beam Position 1.2mm

The results from this are more promising - providing smoother results within a smaller window. However, this method still has the unfortunate consequence of reducing the amplitude of the peaks so that there will be a much smaller range produced in the final results.

5.5.5 Noise Removal

Therefore, a new approach is taken, using an algorithm which utilises a tunable threshold-noise parameter k so that, assuming the image intensifier is working and a large signal to noise ratio exists, meaning that the data points are largely separated from the noise, then all values below this value are removed and the point is interpolated linearly to estimate it's value. To account for large changes in signal strength, k is calculated proportionally to an estimated noise power. Since we assume shot noise is the most prevalent and is approximated by $\sqrt{signal}$ [67]. Since it will make little difference in terms of magnitude and because in reality we would not have access to the real noise power it is estimated as the root mean square of the original sensor image.



(a) $k = 100\times$Noise Signal (b) $k = 1000\times$Noise Signal

Figure 5.16: Integrated slices, threshold value removal, linear interpolation, at Beam Position 1.2mm

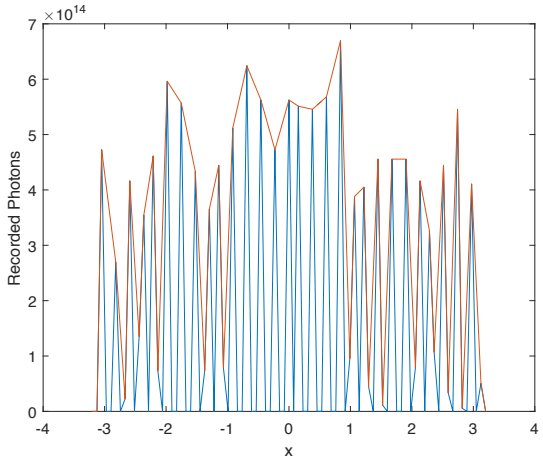


Figure 5.17: $k = 1000\times$Noise Signal at Beam Position 7.6mm

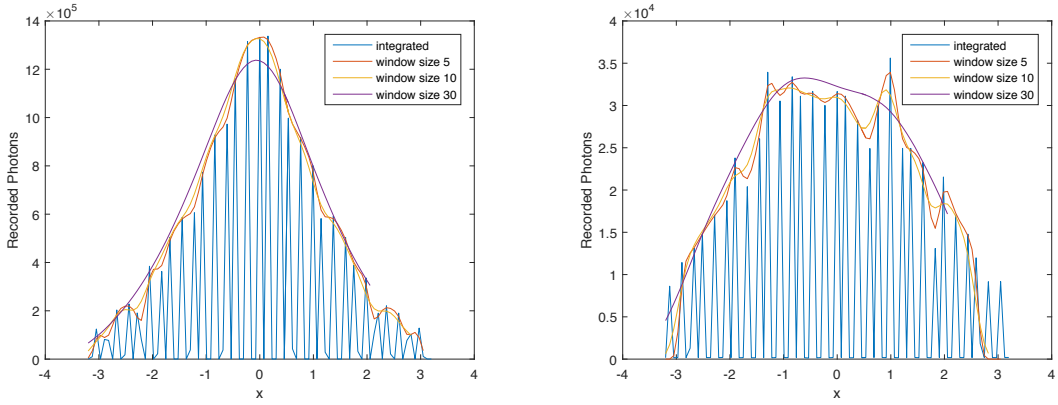
However, even at very high threshold values, this method still has issues at different beam positions as in figure 5.17. This method often gives the most useful results as it seems to best approximate missing data as in figure 5.16b without adding in any extra features that were not there before. However, no value of k was completely able to remove background noise points from the data. This leads to a situation where the final reconstruction still had unrealistic drops in the profile image which is not representative of the real profile.

5.5.6 The Final Approach

Since, the threshold value provided a good solution for removing many of the erroneous base noise signal values and the Hamming window proved to be more useful at smoothing then the rectangular window, then the process of correcting the data would follow these steps:

- Removal of baseline noise using threshold value $k = 1000\times$Estimated Noise Signal.
- Filtering using the Hamming window, with window size yet to be decided.
- Scaling so that the output represents the original input values.
- Correction for group delay of the Hamming Window function.

Figures 5.18a and 5.18b show this process for various window sizes, from which it was determined that a window size of 10 gave the best results between following the data and ensuring no loss of information and estimating the points that had been removed.



(a) Beam Position 1.2mm (b) Beam Position 2.8mm

Figure 5.18: Noise Removed, Hamming Window Filtered, Scale and Delay Corrected

5.5.6.1 Final Reconstruction

Now that all data correction techniques had been applied to each individual slice of the data, it was time for them to be compiled and the gaps between each slice to be estimated. The compilation of individual slices in shown in figure 5.19. To scale the axes correctly to their original values, the magnification factor must be known.

To estimate between the slices an interpolation function was used from [77] which is designed to fill in empty cells within 2-dimensional matrices by linear interpolation of surrounding cells. Due to the many orders of magnitude difference between the proton and electron signals, the interpolation function could not work around the boundary and therefore, it was necessary to segment and perform the function only on lines belonging to the proton core. The final reconstruction of the proton core is shown in figure 5.20. A comparison of the original data and the reconstruction is shown in figures 5.21a and 5.21b.

There was a number of issues with the final reconstruction. Firstly, there is an order of magnitude difference between the original data and the reconstruction, which is a result of

only a small fraction of the photons produced hitting the sensor at the end. However, this was to be expected and can be overcome by multiplying the reconstruction by the inverse of the proportion of light entering the aperture as described in section 5.2.4.

More notably, the shape of the reconstruction does not appear completely Gaussian. This is due to the proton profile being cut off at the top and bottom as a result of the much stronger electron signal being imaged at that point. To overcome this, it would require a control system whereby the 2 mm wide neutral beam would be centred so that it only just excites the edge of the proton core, while the lens system images the edge of the protons so that the electron shell is not excited at all during imaging. However, this might still prove unable to capture the full Gaussian shape, in which case it could be used in tandem with the second imaging system which works in the orthogonal direction to capture the top and bottom of the profile.

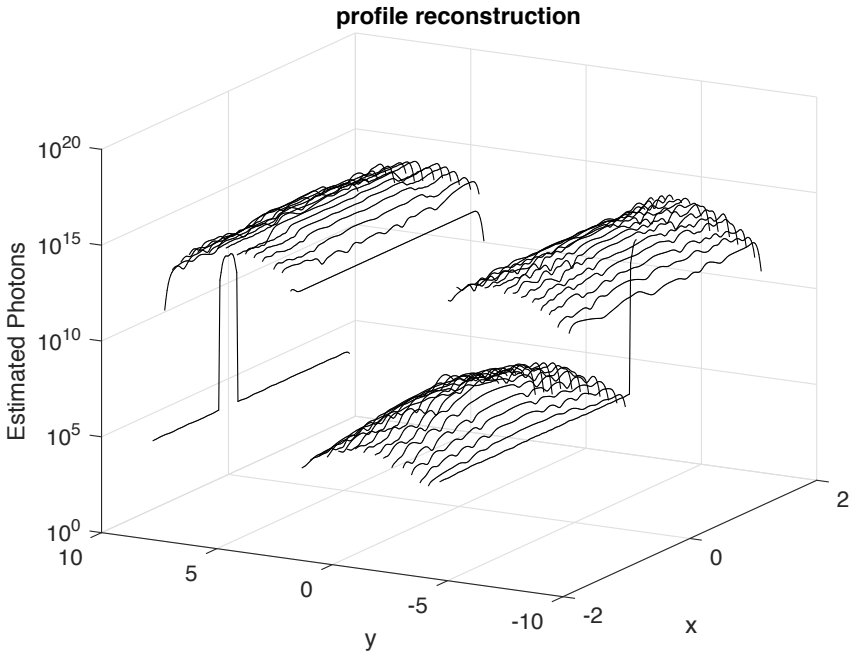


Figure 5.19: Slices compiled at their Beam Position

5.5.6.2 Further Testing

A reconstruction was attempted whereby, the proton core would now be off centre to see if the system could be used to locate the centre of the proton core. The proton core was placed at position $x = 1$ mm, $y = 1$ mm as shown in figure 5.22b. It was found that linearly interpolating the profile image between slices provided unpredictable results and

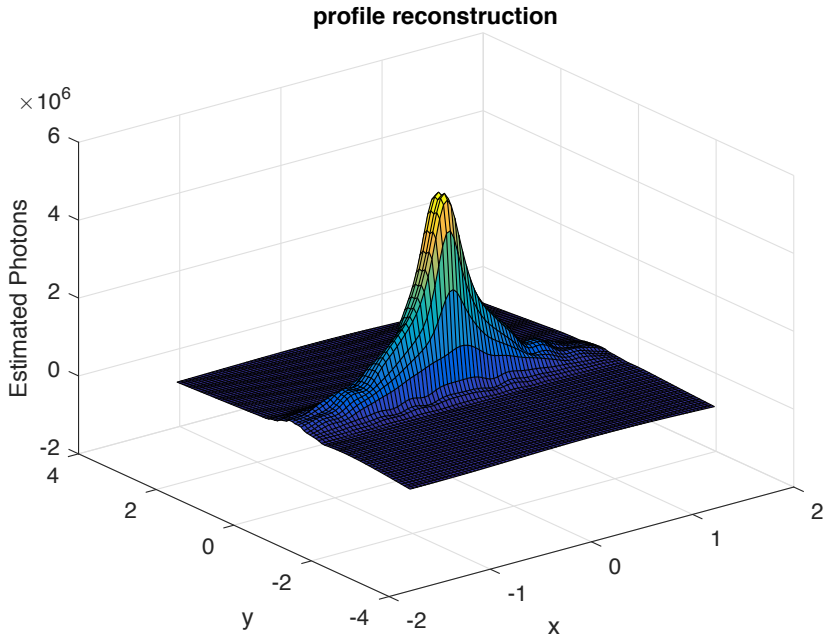
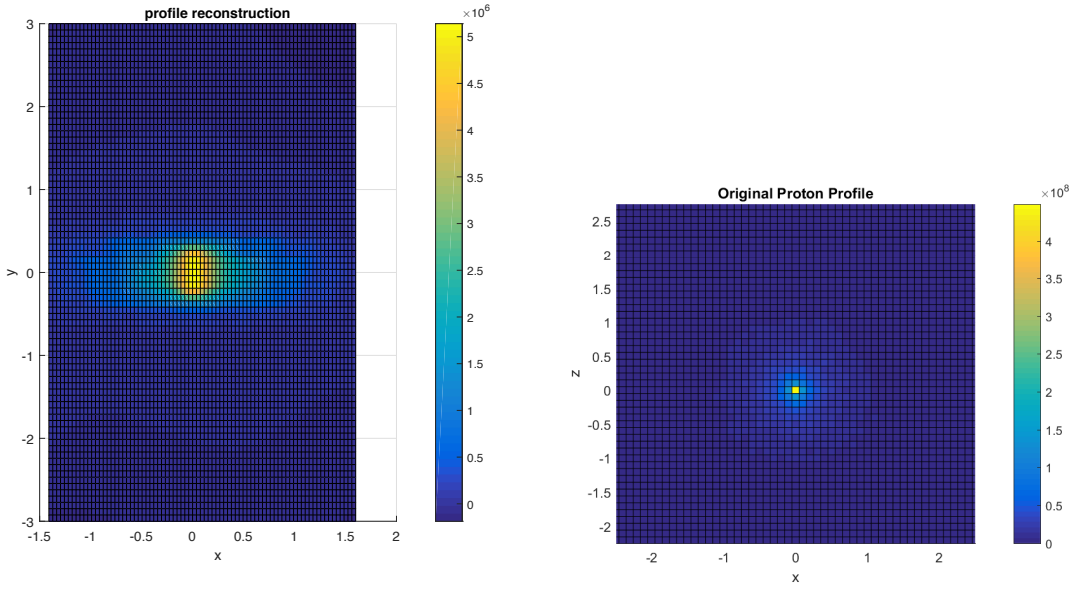


Figure 5.20: Proton Beam Reconstruction

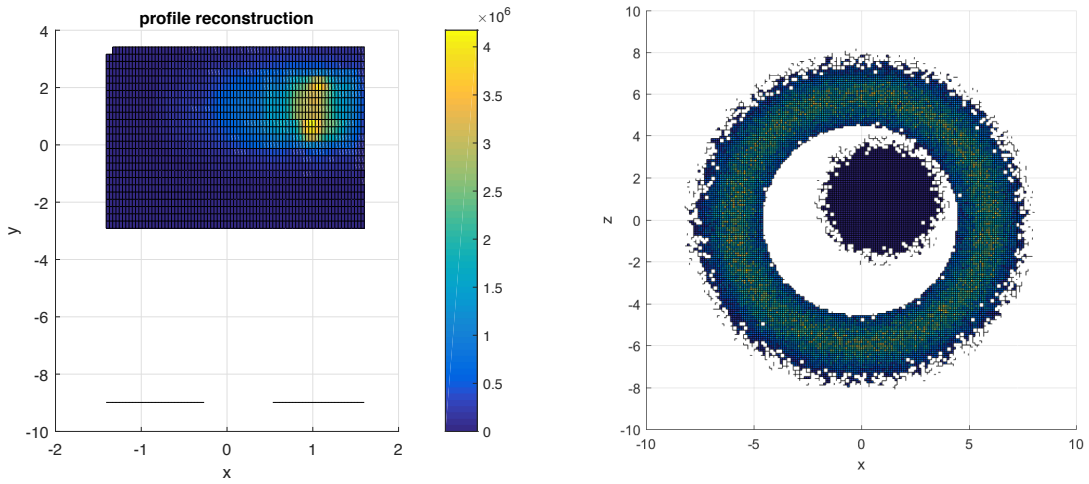


(a) Reconstruction (b) Original Data

Figure 5.21: Profile reconstructed after going through system

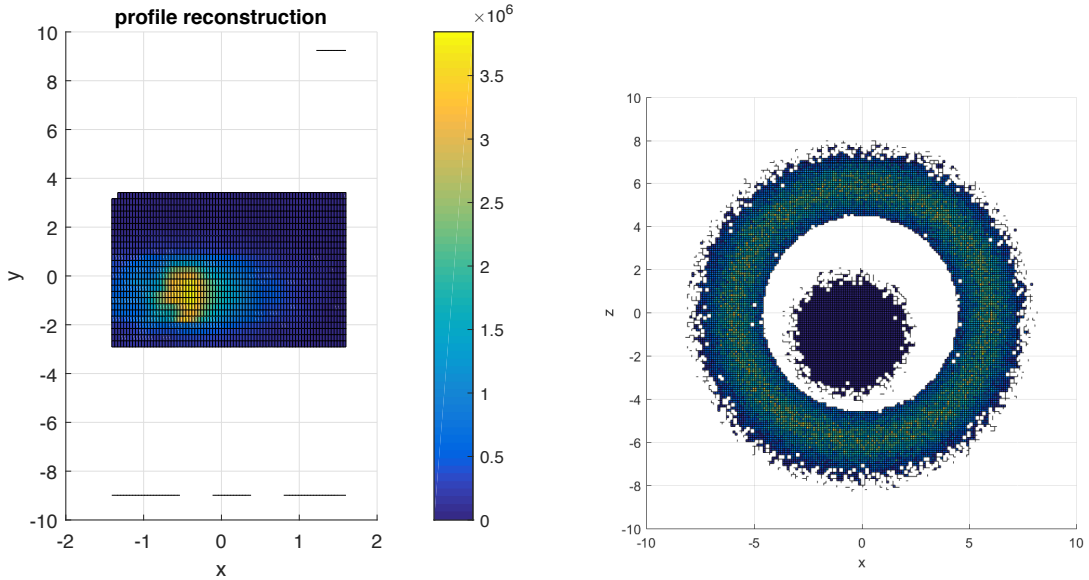
so taking more sample slices of the original data was required to produce a more accurate reconstruction, as shown in figure 5.22a.

Again, the reconstruction suffered from being cut off at the top and bottom, so that a full



(a) Reconstruction (b) Original Data

Figure 5.22: Profile reconstructed with protons centred at $x = 1$ mm, $y = 1$ mm



(a) Reconstruction (b) Original Data

Figure 5.23: Profile reconstructed with protons centred at $x = -0.5$ mm, $y = -1$ mm

image of the Gaussian profile can't quite be seen, however the centre point of the proton core can obtained from this reconstruction as being placed at $x = 1$ mm, $y = 1$ mm. A second simulation with a different proton beam position in also shown.

5.6 SOLIDWORKS Models

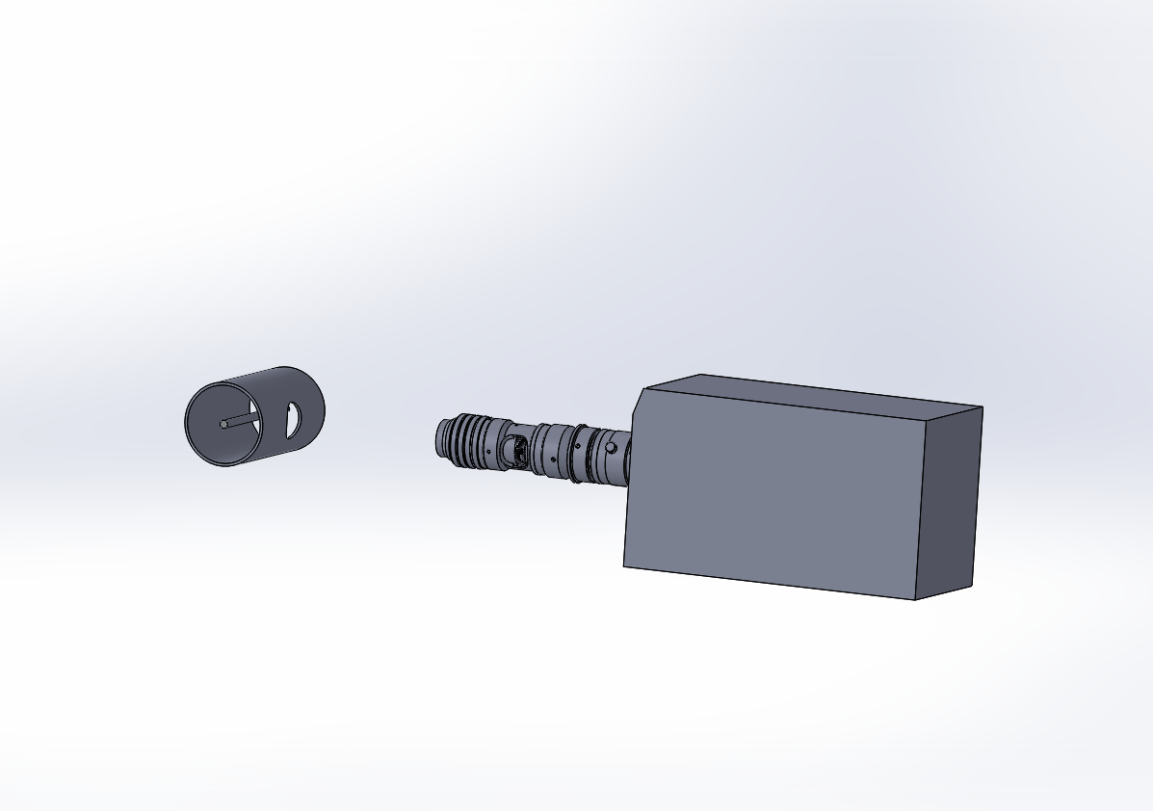


Figure 5.24: 3D camera and lens setup

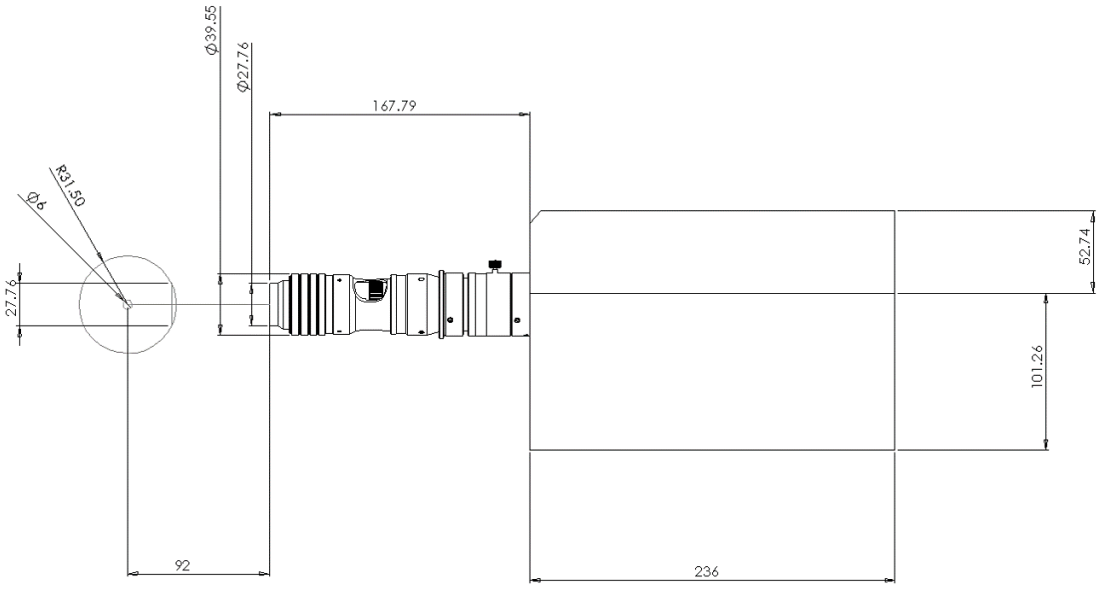


Figure 5.25: 2D drawing of component parts

Chapter 6

Conclusion

The neutral beam diagnostic method consisting of the components described in section 2.6.2 has proven that it can be used to successfully image the cross section of the proton and electron beams, however it has a number of shortcomings that would still need to be addressed.

An in depth study of atomic ionisation revealed a minimum beam energy of 100 eV that would be required to ensure the neutral beam is not completely ionised by the proton and electron beams and an analysis of the ion trajectory in the magnetic field revealed a maximum energy limit of 20 MeV to ensure sufficient deflection occurs so that ions do not make contact with the MCP detector on the other side of the beam pipe. Since the system performance would be optimal towards the lower limit, a 500 eV atomic neutral Hydrogen beam was chosen. Further analysis determined a pencil beam would be used over a ribbon beam as section 2.4 showed the ribbon beam shape was impossible to generate. The Lotz correlation showed the proton beam signal would be $\times 10^{-12}$ smaller than that of the electron beam signal and therefore two different detection methods would be required. A study was also conducted in section 2.2.2.1 to determine whether a coherently pulsed neutral beam would be advantageous. However, it made little difference to the relative signal strength of the proton and electron beams and therefore a continuous beam was opted for.

The final neutral beam parameters are shown in table 6.1.

Neutral Beam Composition	Neutral Atomic Hydrogen
Neutral Beam Energy	500eV
Beam Current	10mA
Beam Shape	Round Pencil Beam
Beam Radius	1σ where $\sigma = 1$mm
Beam Format	Continuous
Beam Scan Frequency	60Hz

Table 6.1: Neutral Beam Parameters

The neutral hydrogen atom beam would be created by neutralising negative hydrogen ions generated from a Penning Ion Gauge. Due to caesium being used in the source, caesium vapour can leak out with the extracted beam. Electrons are also co-extracted with the ion beam. As these beam impurites can cause unwanted conversion of negative ions to positive ions, a cold box with a 90 degree magnetic dipole is used to remove them. The ion beam is then electrostatically lensed by an Einzel lens to achieve the desired beam shape and two parallel plate condensers are used to deflect the ion beam without leaving any transverse velocity. After the beam is shaped and positioned, it is then neutralised via photo-detachment as described in section 3.5 in a mirrored chamber by passing it through four orthogonally placed (to minimise the effect of interference), high intensity, near-infrared laser sources. Any ions that remain will be removed via an ion dump, finally forming a neutral beam with an energy of 500 eV.

In terms of detecting the electron shell, a few different techniques for neutral atom detection were explored, including the semiconductor detector, the reflection surface, the conversion surface and the micro-channel plate detector. It was concluded that the MCP detector had the simplest design while meeting the requirements of the project. A delay-line layer is placed after the MCP to enhance both spatial and temporal resolution and the calibration of the detector is discussed in section 4.1.7. Analysis of different reconstruction algorithms showed that there would be limitations reconstructing the beam profile from just two orthogonal projections. Therefore, by assuming the electron profile to be an idealised Gaussian shell, the reconstruction process is demonstrated using the back projection algorithm, with minimisation of projection errors in the least-square sense to recover the beam parameters accurately.

To image the proton core a computer model was produced to accurately model different lens and camera parameters. The thin lens equation with the principal planes separated was utilised as it provides a good approximation of a real optical system with a small computation time. From this, it was decided a high magnification zoom lens would be required in conjunction with a high speed, low noise CCD camera for reasons outlined in sections 5.3 and 5.4. Using the computer model, the output from these devices was estimated and using a series of digital reconstruction algorithms as outlined in section 5.5 the position of the proton core was successfully determined while the full Gaussian shape was cut-off unfortunately, again due to the much higher relative strength of the electron signal.

While the system is feasible, due to the nature of the beam generation process, it was decided a neutral beam method is unlikely to be the most viable option for proton and electron shell diagnostics due to the high complexity of the many systems required and the cost of components. A medium to high current negative hydrogen ion source would

need to be commissioned, which together with advanced lensing and collimation can cost as high as USD480k (National Electrostatic Corp Ion source). Therefore, it's likely simpler methods would be considered before this diagnostic method is developed further.

6.1 Further Developments

6.1.1 Obtaining High Energy Cross Section Data

With greater resources and time on this project a number of different areas would be developed in much greater detail. Firstly, more high energy experimental data on the ionisation process between the neutral hydrogen atom beam and the proton core would be required such that the Lotz correlation described in section 2.2.1 would not have to be so heavily relied upon.

6.1.2 Calibrating Neutral Atom Gun

In order to implement the neutral atom generator, a suitable laser source would need to be commissioned with a high energy laser manufacturer as no commercial laser sources are suitable for the project. Testing of the system, with the proposed magnetic shielding from section 3.5.5.3 should also be carried out. Finally, experimental calibration of the ion source and einzel lens will need to be carried out as stated in section 3.3.3.2.

6.1.3 Optimising Reconstruction

To image the transient variation in Gaussian characteristic along the real electron profile, more projection angles would be required. The least number of projections required for a quality reconstruction is 22 as mentioned in section 4.3.2. In order to achieve additional projections, more probe beams approaching the hadron beam at different angles will be needed. The current set-up only has two orthogonal probe beams from two orthogonally positioned neutral atom guns. Adding more such neutral atom generators is not feasible due to both the space limitation and the cost of adding each atom gun/projection. Alternatively, each atom gun can be modified so that the angle of approach can be controlled through the parallel plate condensers.

Instead of using the second condenser to parallelise the beam, it can be used to give the ion beam a transverse velocity, thus giving the probe beam a non-zero angle when approaching the hadron beam. However, the added transverse velocity would cause the overall velocity of the probe beam to be larger, affecting the probe beam's interaction with the hadron beam. To maintain the same probe beam velocity, the initial beam velocity prior

to deflection needs to be reduced. However, to maintain a constant beam current, the extraction voltage cannot change. Thus, the velocity of the ion beam needs to be changed post-extraction, but before deflection. This could be achieved by a set of deceleration grids placed after the 90 degree dipole. However, the initial velocity affects the ion beam deflection and lensing as seen by equation 3.15 and figure 3.3 respectively. Therefore, a robust control system would need to be developed to control the deceleration grids, Einzel lens and parallel plate condensers' voltages.

With suitable control systems in place, each neutral beam generator could be used to create probe beams that approach the hadron beam from a range of angles. If it was decided this was mechanically unachievable, then advances in iterative reconstruction algorithms would be necessary to achieve an acceptable level of reconstruction, for example, by exploring new cost functions.

6.1.4 Improving CCD Noise Rejection

A motorised zoom and focusing system for the proton imaging lens would need to be developed in order to finely adjust the field of view as different depths within the proton beam are being scanned. This would mean less of the proton profile would be cut off by the much stronger signal originating from the electron shell. One solution is that the motor is set back away from the strong magnetic field and is connected to the focusing and magnification rings on the lens via a long rod and a gearing system. This would minimise the amount of magnetic shielding required, therefore less of the solenoid would have to be removed near the front of the lens.

6.1.5 Miscellaneous

Further study into the risks of irradiation damage to camera sensors would have to be conducted to determine whether the camera had to be placed further back from the high energy beams. Most importantly, an in depth analysis of a vacuum pump system would be required to access how the neutral atoms would be removed once ionised to ensure the ultra-high vacuum system is not compromised.

Bibliography

[1] Giulio Stancari, Valentina Previtali, Alexander Valishev, Roderik Bruce, Stefano Redaelli, Adriana Rossi, and Belen Salvachua Ferrando. Conceptual design of hollow electron lenses for beam halo control in the Large Hadron Collider. 2014.

[2] T. Moore, N.I. Agladze, I.V. Bazarov, A. Bartnik, J. Dobbins, B. Dunham, S. Full, Y. Li, X. Liu, J. Savino, and K. Smolenski. Fast wire scanner for intense electron beams. *Physical Review Special Topics - Accelerators and Beams*, 17(2), 2014. cited By 0.

[3] J. D. Gilpatrick. Techniques for intense-proton-beam profile measurements. *AIP Conference Proceedings*, 451(1):110–124, 1998.

[4] S. Kopp, B. Baller, S. Childress, R. Ford, D. Harris, D. Indurthy, C. Kendziora, C. Moore, Ž. Pavlović, M. Proga, G. Tassotto, and R. Zwaska. Segmented foil sem grids for high-intensity proton beams at fermilab. volume 2, pages 1047–1051, 2005. cited By 0.

[5] J. Krider. Residual gas beam profile monitor. *Nucl. Instrum. Meth.*, A278:660–663, 1989.

[6] F. Becker R. Haseitl P. Forck, C. Andre and B. Walasek-Hohne. Beam induced fluorescence profile monitor developments. *Proceedings of HB2010*, 2010.

[7] P Ausset, S Bousson, D Gardès, A C Müller, B Pottin, R Gobin, G Belyaev, and I Roudskoy. Optical Transverse Beam Profile Measurements for High Power Proton Beams. 2002.

[8] F. Pérez U. Iriso. SYNCHROTRON RADIATION MONITORS AT ALBA. *Proceedings of EPAC 2006, Edinburgh, Scotland*, 2006.

[9] Massimiliano Putignano. *Supersonic Gas-Jet Based Beam Profile Monitor*. PhD thesis, University of Liverpool, July 2012.

[10] M B Shah, P McCallion, and H B Gilbody. Ionisation and electron capture in collisions of slow h + and he 2+ ions with hydrogen. *Journal of Physics B: Atomic, Molecular and Optical Physics*, 22(24):3983, 1989.

[11] W. Lotz. Electron-impact ionization cross-sections and ionization rate coefficients for atoms and ions. *apjs*, 14:207, May 1967.

[12] Xabier Cid Vidal. Lhc parameters, December 2015.

[13] V Shiltsev, A Drozhdin, V Kamerdzhiev, G Kuznetsov, L Vorobiev, et al. LHC particle collimation by hollow electron beams. *Proceedings EPAC08, MOPC098*, 2008.

[14] Vasilis Tzoganis and Carsten P. Welsch. A non-invasive beam profile monitor for charged particle beams. *Applied Physics Letters*, 104(20), 2014.

[15] F. Hornstra. A beam induced gas scintillation (BIGS) profile monitor for hera. 1989.

[16] J. Camas, R. J. Colchester, G. Ferioli, R. Jung, and J. Koopman. Preliminary test of a luminescence profile monitor in the CERN SPS. 1999.

[17] Peter Forck. Lecture notes on beam instrumentation and diagnostics. 2012.

[18] F. Becker. Beam induced fluorescence profile monitors. *Proceedings of DIPAC2011*, 2011.

[19] H. Bethe und J. Ashkin. Experimental nuclear physics. 1953.

[20] G. Ferioli R. Jung J. Koopman R. Perret A. Variola J.M. Vouillot G. Burtin, J. Camas. THE LUMINESCENCE PROFILE MONITOR OF THE CERN SPS. *Proceedings of EPAC 2000, Vienna, Austria*, 2000.

[21] R. Jung A. Variola and G. Ferioli. Characterization of a nondestructive beam profile monitor using luminescent emission. 2007.

[22] Roy Middleton. A Negative-Ion Cookbook. 1990.

[23] Jure Maglica. Plasma heating with neutral beam injection. 2005.

[24] Safdar Ali. *Electron-ion recombination data for plasma applications*. PhD thesis, 2012.

[25] Accelerated neutral atom beam (anab).

[26] A.Jeff, E.B.Holzer, T.Lefevre, V.Tzoganis, C.Welsch, and H.Zhang. Quantum Gas Jet for Non-Invasive Beam Profile Measurement. Technical report, 2014.

[27] Douglas P. Moehs, Jens Peters, and Joseph Sherman. Negative Hydrogen Ion Sources for Accelerators. *IEEE TRANSACTIONS ON PLASMA SCIENCE*, 33(6):1786–1798, 2005.

[28] D.C. Faircloth. Negative Ion Sources: Magnetron and Penning. *CERN Yellow Report CERN-2013-007*, pages 285–310, 2014.

[29] D.C. Faircloth, J.W.G. Thomason, R. Sidlow, A.P. Letchford, J. Pozimski, M.O. Whitehead, T. Wood, S. Jolly, P. Savage, M. Haigh, J. Morrison, I. Yew, and G. Doucas. The Development of the ISIS H- Surface Plasma Ion Source at RAL. Number 18 in International Collaboration on Advanced Neutron Sources, April 2007.

[30] Charles W. Schmidt. REVIEW OF NEGATIVE HYDROGEN ION SOURCES. Linear Accelerator Conference, Albuquerque, New Mexico, USA, 1990.

[31] T. Kalvas. Beam Extraction and Transport. CERN Accelerator School, Ion Sources, pages 537–564, May 2012.

[32] Helmut Liebl. *Applied Charged Particle Optics*. Springer, 2007.

[33] Douglas A. Brown and John F. O'Hanlon. Space-charge divergence of an intense, unneutralized rectangular ion beam. *Phys. Rev. E*, 48:523–531, Jul 1993.

[34] T. Tomisawa, H. Akikawa, S. Sata, A.Ueno, Y. Kondo, H. Oigawa, T.Sasa, K.Hasegawa, S.Lee, I. Zenei, T. Toyoma, and M. Ikegami. Investigation of Photo Neutralization Efficiency of High Intensity H- Beam With ND:YAG Laser in J-PARC. Number 7 in European Workshop on Beam Diagnostics and Instrumentation for Particle Accelerators (DIPAC), June 2005.

[35] Robert E. Shafer. Laser Diagnostic for High Current H– Beams. AIP Conference, Stanford, California (USA), 1998.

[36] Stephen J. Smith and David S. Burch. Photodetachment cross section of the negative hydrogen ion. *Phys. Rev. Lett.*, 2:165–166, Feb 1959.

[37] Alexei M. Frolov. Photodetachment cross-section of the negatively charged hydrogen ion. November 2015.

[38] Stephen A. Benton and V. Michael Bove Jr. *Holographic Imaging*. Wiley-Blackwell, 2008.

[39] Mircea Mujat, Aristide Dogariu, and Emil Wolf. A law of interference of electromagnetic beams of any state of coherence and polarization and the Fresnel–Arago interference laws. *Journal of the Optical Society of America A*, 21(12):2414–2417, 2004.

[40] Magnetic shield corp. mumetal® zero gauss chamber.

[41] Broadband dielectric mirrors, thorlabs website.

[42] Laser diode array 900w qcw, cutting edge optronics.

[43] K.C.Harvey and Jr. C.Fehrenbach. Semiconductor detector for the selective detection of atomic hydrogen. *Review of Scientific Instruments,54(9)*, 1983.

[44] Alexander Grigoriev. *The Neutral Particle Detector on the Mars and Venus Express missions*. PhD thesis, Swedish Institute of Space Physics, Kiruna, September 2007.

[45] NASA. Nasa spaca science data coordinated archive, neutral particle imager(pippi).

[46] Mark W. Utlaut Anthony Graupera, N. William Parker. On-axis detector for charged particle beam system.

[47] Mcp assembly, technical information,hamamatsu photonics.

[48] German Image Detector Systems. Mcp-detector cf-viewport assembly, 2015.

[49] Achim Czasch Reinhard Dörner Mirko Hattaß Min Huang Volker Mergel Uwe Spillmann Klaus Ullmann-Pfleger Thorsten Weber Horst Schmidt-Böcking Ottmar Jagutzki, Alfred Cerezo and George D. W. Smith. Multiple hit readout of a microchannel plate detector with a three-layer delay-line anode. *IEEE TRANSACTIONS ON NUCLEAR SCIENCE*, 2002.

[50] R. Rispoli ; E. De Angelis ; L. Colasanti ; N. Vertolli ; S. Orsini ; J. A. Scheer ; A. Mura ; A. Milillo ; P. Wurz ; S. Selci ; A. M. Di Lellis ; R. Leoni ; M. D'Alessandro ; F. Mattioli ; S. Cibella. Elena mcp detector: absolute detection efficiency for low-energy neutral atoms. *SPIE Conference Volume 8450*, 2012.

[51] MATLAB help Mathworks. Radon transform.

[52] Vedhanayagam Masilamani and Kamala Krithivasan. A min-cost-max-flow based algorithm for reconstructing binary image from two projections using similar images. 2008.

[53] G.T.Herman and R.Davidi. On image reconstruction from a small number of projections. *IOP Publishing*, 2008.

[54] Franco Casali Samantha Cornacchia Maria Pia Morigi Alessandro Pasini Davide Romani Rosa Brancaccio, Matteo Bettuzzi. Study of an appropriate reconstruction algorithm for an innovative electron beam imaging system for dosimetry in iort (intra operative radiation therapy). *IEEE*, 2004.

[55] Hairong Zheng Zhanli Hu. Improved total variation minimization method for few-view computed tomography image reconstruction. June 2014.

[56] Jean-Jacques Leveque Jeannot Trampert. Simultaneous iterative reconstruction technique: Physical interpretation based on the generalized least squares solution. 1990.

[57] Yao Danya Zhang Baofen Su Bangliang, Peng Lihui. An improved simultaneous iterative reconstruction technique for electrical capacitance tomography. 1999.

[58] Justin Romberg Emmanuel Candes and Terence Tao. Robust uncertainty principles: Exact signal reconstruction from highly incomplete frequency information. *IEEE Trans Inf Theory 2006;52:489–509.*, 2006.

[59] A Lipson, S G Lipson, and H Lipson. *Optical Physics*. Cambridge University Press, 2010.

[60] Eustace L. Dereniak and Teresa D. Dereniak. *Geometrical and Trigonometric Optics*. Cambridge University Press, 2008.

[61] A Walther. *The Ray and Wave Theory of Lenses*. Cambridge Studies in Modern Optics. Cambridge University Press, 2006.

[62] Ramesh Jain, Rangachar Kasturi, and Brian G Schunck. *Machine Vision*. 1995.

[63] Murali Subbarao and Ming-Chin Lu. *Computer Modeling and Simulation of Camera Defocus*. PhD thesis, State University of New York.

[64] J. Avison. *The World of Physics*. Nelson, 2014.

[65] Eric W. Weisstein. Solid Angle, MathWorld, A Wolfram Web Resource.

[66] Solid Angle Calculation for a Circular Disk. *THE REVIEW OF SCIENTIFIC INSTRUMENTS*, 30(4), 1959.

[67] Chris McFee. Noise sources in a CCD.

[68] SERVO CONTROL FACTS A HANDBOOK EXPLAINING THE BASICS OF MOTION, BALDOR ELECTRIC COMPANY.

[69] Pierre Magnan. Detection of visible photons in CCD and CMOS: A comparative view. *Nuclear Instruments and Methods in Physics Research Section A: Accelerators, Spectrometers, Detectors and Associated Equipment*, 504(1-3):199–212, may 2003.

[70] Ted Pella Inc. Background Information on CCD and CMOS Technology.

[71] Jihong Wang and Timothy J Blackburn. The AAPM/RSNA Physics Tutorial for Residents X-ray Image Intensifiers for Fluoroscopy. *RG I*, 20(5), 2000.

[72] Stanford Computer Optics, 4 Quik E Datasheet.

[73] Steven Roberts. B14: Signal Processing Lecture Series, Department of Engineering Science, University of Oxford, 2016.

[74] John Chiverton. Lecture 05: Design of Non-recursive Digital Filters, School of Information Technology, Mae Fah Luang University.

[75] Tom O'Haver. A Pragmatic Introduction to Signal Processing, Smoothing, 2016.

[76] Eric W. Weisstein. Hamming Function, MathWorld, A Wolfram Web Resource.

[77] John D'Errico. inpaint nans.m, 2009.